TAMPEREEN TEKNILLINEN YLIOPISTO
TAMPERE UNIVERSITY OF TECHNOLOGY

Ilkka Kylänpää

First-principles Finite Temperature Electronic Structure of Some Small Molecules

Julkaisu 990 • Publication 990

Tampere 2011

Tampereen teknillinen yliopisto. Julkaisu 990
Tampere University of Technology. Publication 990

Ilkka Kylänpää

First-principles Finite Temperature Electronic Structure of Some Small Molecules

Thesis for the degree of Doctor of Science in Technology to be presented with due permission for public examination and criticism in Sähkötalo Building, Auditorium S4, at Tampere University of Technology, on the 4th of November 2011, at 12 noon.

Tampereen teknillinen yliopisto - Tampere University of Technology
Tampere 2011

ISBN 978-952-15-2662-6 (printed)
ISBN 978-952-15-2674-9 (PDF)
ISSN 1459-2045

Abstract

The work presented in this thesis is based on the Feynman path integral formalism for quantum statistics. This brings forth a novel approach to solve quantum many-body systems giving complementary knowledge to more conventional approaches. In practice, the multidimensional path integrals are evaluated with Monte Carlo methods, and hence, the approach is called path integral Monte Carlo (PIMC).

The PIMC method has not gained the deserved popularity, yet, even though this finite temperature approach yields exact quantum statistics. In practice, the PIMC method faces challenges deriving from its computational labour and the proper treatment of antisymmetric density matrix in case of identical fermions, that is, the fermi statistics. Also, the singularity of the Coulomb potential sets challenges for the most direct application of the path integrals.

In this thesis we concentrate on the finite temperature quantum chemistry of some small molecules using the path integral Monte Carlo method. First, we give a brief introduction to the basics of the path integral formalism and its application using the Metropolis Monte Carlo algorithm. Second, we show how to overcome the problems related to the Coulomb singularity. Third, a brief survey on path integrals for fermions is carried out. Finally, we present the results from the four papers, which are included in this thesis and have been published in the refereed journals of the American Institute of Physics and the American Physical Society.

In Paper I, a three-body quantum system, hydrogen molecule ion H_2^+, is revisited, once again. There we aim at tracing the electron–nuclei coupling effects in the three-body all-quantum, i.e. nonadiabatic, molecule. Among others we have evaluated spectroscopic constants and molecular deformation, also considering the isotope effects. Distinct features of coupling are found for the nuclei.

In Paper II, we have found and explained the surprising thermal instability of the dipositronium molecule, Ps_2. A proper nonadiabatic treatment is necessary for the dipositronium, thus making it challenging for conventional methods of quantum chemistry. In addition, with the PIMC method the present strong correlations are described properly.

In Paper III, the quantum statistics of the five-particle molecule, H_3^+ ion, is examined. There we show how contributions from quantum and thermal dynamics to the particle distributions and correlation functions can be sorted out, and furthermore, how the quantum to classical dynamics transition can be monitored. At low temperatures the necessity of the fully quantum mechanical approach for all five particles is established.

In Paper IV, the nonadiabatic simulations of Paper III are extended to higher temperatures, also, where the molecular dissociation–recombination equilibrium is studied. The temperature dependent mixed state description of the H_3^+ ion, the density dependent equilibrium dissociation–recombination balance and the energetics has been evaluated for the first time. At about 4000 K the fragments of the molecule, H_2+H^+, H_2^++H and 2H+H^+, start contributing. Paper IV gives major additions to the earlier published studies in the literature, where the dissociation–recombination reaction of H_3^+ has been neglected.

Preface

This thesis consists of four papers published in refereed journals and an introductory part. The introductory part, along with the appendices, aim at providing the relevant details for proper application of the path integral Monte Carlo method for the quantum chemistry of small molecules. The result from the published papers demonstrate that the Feynman formulation of statistical mechanics is a powerful tool for solving quantum many-body systems.

The introductory part, especially the Matrix squaring section in Chapter 3, has a lot of mathematical details in it. They are meant to speed up the understanding and, in particular, the implementation process of the next generation. Thus, at first those parts may seem less readable, but bear with me.

The main message of this work is to highlight the importance of path integrals in the description of subtle quantum effects. There are still plenty of interesting research subjects that can be addressed instantly with the path integral Monte Carlo method. In addition, the development of this approach to properly treat the fermion statistics is of great interest at the present time — although extremely challenging.

The research work was carried out in the Department of Physics at Tampere University of Technology during the years $2007 - 2011$. For financial support the author is greatful for the Department of Physics, Jenny and Antti Wihuri Foundation and Finnish Foundation for Technology Promotion.

First and foremost, the author is exceedingly grateful to his supervisor, professor Tapio T. Rantala, for the support and guidance during these years needed to finish this thesis. I would also like to thank the people of the Electronic Structure Theory group and the Department of Physics, in particular, Dr. Markku Leino, Dr. Johannes Vuorinen, Mr. Jussi Ojanen and Mr. Mikael Kuisma. This thesis was reviewed and criticized by two distinguished experts, professors David M. Ceperley and Cyrus J. Umrigar, to whom the author expresses his gratitude, also. Last, but not least, the author is especially thankful for his family, relatives and friends.

List of Publications

The thesis includes the following publications

- Paper I: I. Kylänpää, M. Leino and T. T. Rantala, *Hydrogen molecule ion: Path integral Monte Carlo approach*, Physical Review A 76, 052508 (2007)
- Paper II: I. Kylänpää and T. T. Rantala, *Thermal dissociation of dipositronium: Path-integral Monte Carlo approach*, Physical Review A 80, 024504 (2009)
- Paper III: I. Kylänpää and T. T. Rantala, *Finite temperature quantum statistics of H_3^+ molecular ion*, Journal of Chemical Physics 133, 044312 (2010)
- Paper IV: I. Kylänpää and T. T. Rantala, *First-principles simulation of molecular dissociation–recombination equilibrium*, Journal of Chemical Physics 135, 104310 (2011)

For the included papers the author has carried out all the calculations. For the analysis of the results and writing the articles assistance has been provided by the co-authors.

Other publications of the author not included in this Thesis.

- M. Leino, I. Kylänpää and T. T. Rantala, *Coverage dependence of finite temperature quantum distribution of hydrogen on nickel (001) surface*, Surface Science 601, 1246 (2007)

Contents

Chapter 1

Introduction to path integrals

Path integral formalism is an exact and straightforward way to describe a system with interacting quantum particles. In practice, the exactness of the method, however, is usually based on an infinite number of parameters that form the continuous path, and thus, we must settle for a finite approximation of the formalism.

In this chapter, we move gradually towards path integrals. First, the basis dependence of representations in quantum mechanics is introduced. Second, the density matrix and its properties are looked into. Then, finally, we construct the path.

1.1 Basis dependence of representation

Time evolution of a quantum system is described by the time dependent Schrödinger equation

$$\hat{H}|\psi(t)\rangle = i\hbar\frac{\partial}{\partial t}|\psi(t)\rangle, \tag{1.1}$$

where $\hat{H}$ is the Hamiltonian operator corresponding to the total energy of the system. The equation above in its present form is an operator equation of an abstract space of vectors $|\psi(t)\rangle$. The Hamiltonian $\hat{H}$ in this space is independent of its basis. Desired basis is obtained by operating from the left hand side with a *bra*-vector $\langle\cdot|$. For example, a wave function $\psi(R,t)$ of the *Hilbert space* is

$$\psi(R,t) \equiv \langle R|\psi(t)\rangle. \tag{1.2}$$

For the operators of the abstract space the basis is given similarly. For example, the position and momentum operators in coordinate basis are

$$\langle R|\hat{R}|\psi(t)\rangle = R\langle R|\psi(t)\rangle = R\psi(R,t) \quad \text{and} \tag{1.3a}$$

$$\langle R|\hat{p}|\psi(t)\rangle = -i\hbar\nabla\langle R|\psi(t)\rangle = -i\hbar\nabla\psi(R,t). \tag{1.3b}$$

Thus, we may define the following transformations [Kleinert, 2004]

$$\langle R|\hat{p} \equiv -i\hbar\nabla\langle R| \qquad \text{and} \tag{1.4a}$$

$$\begin{aligned}\langle R|\hat{H} &\equiv \langle R|H(\hat{p},\hat{R},t) \\ &\equiv H(-i\hbar\nabla,R,t)\langle R| \\ &\equiv H\langle R|. \end{aligned} \tag{1.4b}$$

The Schrödinger equation of the abstract presentation space may now be transformed into the more conventional Schrödinger equation of the *Hilbert space*

$$\begin{aligned} & \langle R|\hat{H}|\psi(t)\rangle = \langle R|i\hbar\frac{\partial}{\partial t}|\psi(t)\rangle \\ \iff \quad & \langle R|H(\hat{p},\hat{R},t)|\psi(t)\rangle = i\hbar\frac{\partial}{\partial t}\langle R|\psi(t)\rangle \\ \iff \quad & H(-i\hbar\nabla,R,t)\langle R|\psi(t)\rangle = i\hbar\frac{\partial}{\partial t}\langle R|\psi(t)\rangle \\ \iff \quad & H\psi(R,t) = i\hbar\frac{\partial}{\partial t}\psi(R,t). \end{aligned} \tag{1.5}$$

In this thesis, the notation R represents a set of cartesian coordinates of N particles in three dimensions, i.e. $R = \{\boldsymbol{r}_1, \boldsymbol{r}_2, \ldots, \boldsymbol{r}_N\}$ — unless it is momentarily defined in some other way.

1.2 Density matrix and Bloch equation

The quantum statistical analogue to Schrödinger equation is the *Bloch equation* for the density matrix, which may be derived by many means [Feynman, 1972, 1998, Leino, 2007]. Here, we present a way that gives a convenient analogue for the density matrix and the Green's function, and is not often seen in the literature.

For a Hamiltonian $\hat{H} = H(\hat{p},\hat{R})$ that does not explicitly depend on time the Schrödinger equation is separable and is easily solved. Then the time propagation of the wave function from initial state t_0 to t is

$$|\psi(t)\rangle = e^{-i(t-t_0)\hat{H}/\hbar}|\psi(t_0)\rangle \equiv \hat{U}(t-t_0)|\psi(t_0)\rangle, \tag{1.6}$$

where $\hat{U}(t-t_0)$ is called the *time-evolution operator*. More on the *time-evolution operator* is found, for example, in Kleinert [2004].

In the framework of nonrelativistic quantum mechanics only *propagators*, $\langle R|\hat{U}(t-t_0)|R'\rangle$, evolving forward in time are relevant [Kleinert, 2004]. Thus, we may set $t_0 = 0$ and define the *retarded propagator*, i.e. the *Green's function*, as

$$G(R,R';t) \equiv \langle R|\Theta(t)\hat{U}(t,0)|R'\rangle \equiv \langle R|\hat{G}(t)|R'\rangle, \tag{1.7}$$

where $\hat{G}(t)$ is a basis independent *Green's function* and $\Theta(t)$ is a Heaviside step function having $\Theta(t) = 1$ if $t \geq 0$, and is otherwise zero. It is easily verified that the *propagator* in Eq. (1.7) satisfies the well known equation for *Green's functions* [Mattuck, 1992, Schulman, 2005]

$$\Big[H - i\hbar\frac{\partial}{\partial t}\Big]G(R, R'; t) = -i\hbar\delta(t)\delta(R - R'). \tag{1.8}$$

Imaginary time, $t - t_0 = -i\hbar\beta$ and $-i\hbar\frac{\partial}{\partial t} = \frac{\partial}{\partial\beta}$, analogue for the *time-evolution operator* is

$$\hat{U}_\beta(\beta) \equiv \hat{U}(-i\hbar\beta) = e^{-\beta\hat{H}}. \tag{1.9}$$

If we define a retarded imaginary time-evolution operator as

$$\hat{\rho}(\beta) \equiv \Theta(\beta)\hat{U}_\beta(\beta) \tag{1.10}$$

then the retarded imaginary time propagator is

$$\rho(R, R'; \beta) \equiv \langle R|\hat{\rho}(\beta)|R'\rangle = \Theta(\beta)\langle R|\hat{U}_\beta(\beta)|R'\rangle. \tag{1.11}$$

The object in Eq. (1.11) is a solution to the *Bloch equation*

$$\Big[H + \frac{\partial}{\partial\beta}\Big]\rho(R, R'; \beta) = \delta(\beta)\delta(R - R'), \tag{1.12}$$

since the β-derivative is

$$\begin{aligned}
\frac{\partial\rho(R, R'; \beta)}{\partial\beta}\Big|_{\beta=0} &= \frac{\partial}{\partial\beta}[\Theta(\beta)\langle R|\hat{U}_\beta(\beta)|R'\rangle]_{\beta=0} \\
&= \Big[\frac{\partial\Theta(\beta)}{\partial\beta}\langle R|\hat{U}_\beta(\beta)|R'\rangle + \Theta(\beta)\frac{\partial}{\partial\beta}\langle R|\hat{U}_\beta(\beta)|R'\rangle\Big]_{\beta=0} \\
&= \Big[\delta(\beta)\langle R|\hat{U}_\beta(\beta)|R'\rangle + \Theta(\beta)\langle R| - \hat{H}\hat{U}_\beta(\beta)|R'\rangle\Big]_{\beta=0} \\
&= \Big[\delta(\beta)\langle R|\hat{U}_\beta(\beta)|R'\rangle - \Theta(\beta)H\langle R|\hat{U}_\beta(\beta)|R'\rangle\Big]_{\beta=0} \\
&= \delta(0)\langle R|R'\rangle - \Theta(0)H\langle R|R'\rangle \\
&= \delta(0)\delta(R - R') - H\delta(R - R').
\end{aligned}$$

A solution of the Bloch equation is called *density matrix*. In quantum statistics β is identified with the inverse temperature: $\beta = 1/k_{\mathrm{B}}T$. Therefore, $\beta > 0$ for all T and the unnormalized *density operator* may be written as

$$\hat{\rho}(\beta) = \exp(-\beta\hat{H}). \tag{1.13}$$

Other approaches to the *Bloch equation* and *density matrices* are more statistical in nature, but here the point is to introduce the trivial — yet not often thought of — analogue between quantum mechanics and quantum statistics, i.e.

$$\rho(R, R'; \beta) = G(R, R'; -i\hbar\beta). \tag{1.14}$$

1.2.1 Properties of density matrices

As was shown in the last section, there is a clear analogue with density matrices and Green's functions. Thus, they share the same properties — at least in the mathematical point of view.

For the quantum statistical density operator, Eq. (1.13), we have

$$\begin{aligned}\hat{\rho}(\beta_1 + \beta_2) &= \hat{G}(-i\hbar(\beta_1 + \beta_2)) \\ &= \hat{G}(-i\hbar\beta_1)G(-i\hbar\beta_2) \\ &= \hat{\rho}(\beta_1)\hat{\rho}(\beta_2),\end{aligned} \tag{1.15}$$

and thus, we may write

$$\begin{aligned}\rho(R, R'; \beta_1 + \beta_2) &= \langle R|\hat{\rho}(\beta_1 + \beta_2)|R'\rangle \\ &= \langle R|\hat{\rho}(\beta_1)\hat{\rho}(\beta_2)|R'\rangle \\ &= \langle R|\hat{\rho}(\beta_1) \int \mathrm{d}R'' \; |R''\rangle\langle R''| \; \hat{\rho}(\beta_2)|R'\rangle \\ &= \int \mathrm{d}R'' \; \langle R|\hat{\rho}(\beta_1)|R''\rangle\langle R''|\hat{\rho}(\beta_2)|R'\rangle \\ &= \int \mathrm{d}R'' \; \rho(R, R''; \beta_1)\rho(R'', R'; \beta_2),\end{aligned} \tag{1.16}$$

where we used the coordinate space *identity operator*

$$\mathbf{I} = \int \mathrm{d}R \; |R\rangle\langle R|. \tag{1.17}$$

Eqs. (1.15) and (1.16) simply state that the product of two density matrices (operators) is a density matrix (operator). These properties are the foundations for the path integral formalism, which becomes crystal clear why in the section Path integral. In practice, however, presumably the most important property is that the density matrix in the coordinate representation is nonnegative. Thus, we may interpret the densities as probability distributions [Ceperley, 1995].

1.2.2 Wave function presentation of density matrix

Let $|n\rangle$ be a complete orthonormal set of functions in Hilbert space, which satisfy the stationary Schrödinger equation

$$\hat{H}|n\rangle = E_n|n\rangle, \tag{1.18}$$

where $n = 0, 1, \ldots$ and E_n corresponds to the energy of the eigenfunction $|n\rangle$. For a complete basis we may employ the well known *completeness relation* [Kleinert, 2004]

$$\mathbf{1} = \sum_n |n\rangle\langle n| + \int \mathrm{d}c\, |c\rangle\langle c|. \tag{1.19}$$

Now, we may write the density matrix as an expansion of wave functions $\phi_n(R) = \langle R|n\rangle$.

$$\rho(R, R'; \beta) = \sum_n \phi_n(R)\phi_n^*(R')e^{-\beta E_n} + \int \mathrm{d}c\, \phi_c(R)\phi_c^*(R')e^{-\beta E_c}. \tag{1.20}$$

In order to save some space we will consider only the discrete part of the *completeness relation* in showing how one arrives at Eq. (1.20).

$$\begin{aligned}
\rho(R, R'; \beta) &= \langle R|\hat{\rho(\beta)}|R'\rangle \\
&= \langle R|e^{-\beta\hat{H}}|R'\rangle \\
&= \sum_n \langle R|e^{-\beta\hat{H}}|n\rangle\langle n|R'\rangle \\
&= \sum_n \langle R|n\rangle\langle n|R'\rangle e^{-\beta E_n} \\
&= \sum_n \phi_n(R)\phi_n^*(R')e^{-\beta E_n}.
\end{aligned} \tag{1.21}$$

For the spectral integral part of the *completeness relation* the procedure is identical — instead of a sum we have an integral. In addition, sometimes one may come across with notations where the summation in Eq. (1.21) actually contains also the *continuum* contributions.

1.2.3 Partition function

For a system in thermal equilibrium at constant temperature the partition function and the density matrix may be calculated by an analytic continuation of the Green's function to the imaginary time, see section Density matrix and Bloch equation. For

such a system the partition function contains all the thermodynamical information of the system [Kleinert, 2004]. The local thermodynamical properties, however, are included in the density matrix from which all the properties of the quantum system may be derived [Pollock and Ceperley, 1987].

The partition function is defined as the trace of the density operator, i.e.

$$Z = \mathrm{Tr}\ \hat{\rho}(\beta). \tag{1.22}$$

In the coordinate basis this transforms into an integral over the diagonal elements of the density matrix,

$$Z = \int \mathrm{d}R\ \rho(R, R; \beta). \tag{1.23}$$

Inserting the wave function expansion of the density matrix, Eq. (1.21), into the integrand of Eq. (1.23), we obtain the traditional expression for the partition function, i.e. the summation over *Boltzmann factor*s,

$$\begin{aligned} Z &= \int \mathrm{d}R \sum_n \phi_n(R)\phi_n^*(R)e^{-\beta E_n} \\ &= \sum_n e^{-\beta E_n} \int \mathrm{d}R\ |\phi_n(R)|^2 \\ &= \sum_n e^{-\beta E_n}, \end{aligned} \tag{1.24}$$

where we have assumed that the wave functions have been normalized to unity, i.e. $\int \mathrm{d}R\ |\phi_n(R)|^2 = 1$ for all n. Furthermore, the summation over Boltzmann factors can be thought of consisting also the continuum contributions, i.e. integrals over continuum eigenenergies.

As was mentioned in section Properties of density matrices, the density matrix may be interpreted as a probability distribution. The integral of the *density function*, diagonal of the density matrix, over all states or configurations thus gives one the total probability of one [Parr and Yang, 1989]. Therefore, we may write the *normalized density matrix* as $Z^{-1}\rho(R, R'; \beta)$, since

$$\int \mathrm{d}R\ Z^{-1}\rho(R, R; \beta) = \frac{\int \mathrm{d}R\ \rho(R, R; \beta)}{Z} = \frac{\int \mathrm{d}R\ \rho(R, R; \beta)}{\int \mathrm{d}R\ \rho(R, R; \beta)} = 1. \tag{1.25}$$

1.2.4 Observables

Any quantity that can be measured is an observable. The expectation value of an observable is the weighted average of the measurement operator over all states or

configurations. In terms of the density operator of the abstract space the expectation value of a measurement operator $\hat{O}$ is

$$\langle \hat{O} \rangle = \frac{\mathrm{Tr}(\hat{O}\hat{\rho}(\beta))}{Z}. \tag{1.26}$$

In the coordinate representation this is given as

$$\begin{aligned}
\langle \hat{O} \rangle &= \frac{\int \mathrm{d}R \, \langle R|\hat{O}\hat{\rho}(\beta)|R\rangle}{Z} \\
&= Z^{-1} \int \mathrm{d}R \, \langle R|\hat{O}\hat{\rho}(\beta)|R\rangle \\
&= Z^{-1} \int \mathrm{d}R\mathrm{d}R' \, \langle R|\hat{O}|R'\rangle\langle R'|\hat{\rho}(\beta)|R\rangle \\
&= Z^{-1} \int \mathrm{d}R\mathrm{d}R' \, \rho(R,R';\beta)\langle R|\hat{O}|R'\rangle,
\end{aligned} \tag{1.27}$$

where the last modification is valid because of the symmetry of the density matrix [Ceperley, 1995]. Usually, the measurement operators for observables are diagonal. Therefore $\langle R|\hat{O}|R'\rangle = O(R)\langle R|R'\rangle$, and

$$\langle \hat{O} \rangle = Z^{-1} \int \mathrm{d}R \, \rho(R,R;\beta)O(R). \tag{1.28}$$

1.2.5 Free particle density matrix

Density matrix of a free particle has substantial importance in the conventional path integral formalism. Thus, here we shall concentrate on that.

For a free particle the Hamiltonian consists of the kinetic operator, only, i.e $\hat{H} = \hat{T}$. Therefore, the Bloch equation, Eq. (1.12), for $\beta > 0$ is

$$\begin{aligned}
-\frac{\partial}{\partial\beta}\rho^{\mathrm{K}}(\boldsymbol{r},\boldsymbol{r}';\beta) &= T(\boldsymbol{r})\rho^{\mathrm{K}}(\boldsymbol{r},\boldsymbol{r}';\beta) \\
\iff \frac{\partial}{\partial\beta}\rho^{\mathrm{K}}(\boldsymbol{r},\boldsymbol{r}';\beta) &= \lambda\nabla^2_{\boldsymbol{r}}\rho^{\mathrm{K}}(\boldsymbol{r},\boldsymbol{r}';\beta),
\end{aligned} \tag{1.29}$$

where $T(\boldsymbol{r}) = -\lambda\nabla^2_{\boldsymbol{r}}$ and $\lambda = \hbar^2/2m$. Eq. (1.29) is a diffusion-like equation [Feynman, 1972, 1998] with diffusion coefficient λ, which leads to a solution

$$\rho^{\mathrm{K}}(\boldsymbol{r},\boldsymbol{r}';\beta) = (4\pi\lambda\beta)^{-d/2} \exp\left[-\frac{(\boldsymbol{r}-\boldsymbol{r}')^2}{4\lambda\beta}\right], \tag{1.30}$$

where d is the dimensionality of the space and the coefficient in front of the exponential comes from the normalization

$$\int \mathrm{d}\boldsymbol{r} \, \rho^{\mathrm{K}}(\boldsymbol{r},\boldsymbol{r}';\beta) = 1. \tag{1.31}$$

The normalization simply indicates that the total probability for a particle to diffuse from $\boldsymbol{r}'$ to $\boldsymbol{r}$ is unity if the particle goes through all the paths between the old and the new position. For N free particles with the same mass the density matrix is simply

$$\rho^{\mathrm{K}}(R,R';\beta) = (4\pi\lambda\beta)^{-dN/2}\exp\left[-\frac{(R-R')^2}{4\lambda\beta}\right]. \tag{1.32}$$

Another way to end up to the same result [Feynman, 1972, 1998, Ceperley, 1995, Leino, 2007] is maybe more practical with respect to the simulations. In that scheme, one considers a free particle in a periodically repeated box. The wave functions for this type of a situation are plane waves such as

$$\psi_n(R) = L^{-d/2}e^{-i\boldsymbol{k}_n\cdot R}, \tag{1.33}$$

where L is the length of the box side and $\boldsymbol{k}_n = 2\pi\boldsymbol{n}/L$, the eigenvalues being $E_n = \lambda\boldsymbol{k}_n^2$. Now, the density matrix may be written in terms of the expansion in Eq. (1.21), i.e.

$$\begin{aligned}\rho^{\mathrm{K}}(R,R';\beta) &= \sum_n \psi_n(R)\psi_n^*(R')e^{-\beta E_n} \\ &= L^{-dN}\sum_n \exp\left[-i\boldsymbol{k}_n\cdot(R-R') - \beta\lambda\boldsymbol{k}_n^2\right].\end{aligned} \tag{1.34}$$

Eq. (1.34) may also be expressed in terms of a Jacobi theta function, $\theta_3(z,t)$, [Ceperley, 1995, Schulman, 2005, Leino, 2007]

$$\begin{aligned}\rho^{\mathrm{K}}(R,R';\beta) &= L^{-dN}\sum_n \exp\left[-i\boldsymbol{k}_n\cdot(R-R') - \beta\lambda\boldsymbol{k}_n^2\right] \\ &= L^{-dN}\sum_n \left[e^{-\beta\lambda(2\pi/L)^2}\right]^{\boldsymbol{n}^2} e^{-2i\pi\boldsymbol{n}\cdot(R-R')/L} \\ &= L^{-dN}\prod_{k=1}^{dN}\sum_{n_k}\left[e^{-\beta\lambda(2\pi/L)^2}\right]^{n_k^2} e^{-2i\pi n_k(R-R')_k/L} \\ &= L^{-dN}\prod_{k=1}^{dN}\theta_3(z_k,t),\end{aligned} \tag{1.35}$$

where $z_k = \pi(R-R')_k/L$, $t = \exp\left[-\beta\lambda(2\pi/L)^2\right]$ and the property $\theta_3(z,t) = \theta_3(-z,t)$ of the theta function was also used.

Eqs. (1.34) and (1.35) are always valid for periodic boundary conditions. However, if the thermal wave length, $\sqrt{2\lambda\beta}$, is significantly smaller than the size of the

box, i.e. $2\lambda\beta \ll L^2$, the summation in Eq. (1.34) may be replaced by an integral and the resulting density matrix may also be used in periodic simulations.

$$\begin{aligned}
\rho^{\mathrm{K}}(R,R';\beta) &= L^{-dN}\sum_n \exp\left[-i\boldsymbol{k}_n\cdot(R-R') - \beta\lambda\boldsymbol{k}_n^2\right] \\
&\approx L^{-dN}\int \frac{L^{dN}}{(2\pi)^{dN}}\mathrm{d}\boldsymbol{k}\ \exp\left[-i\boldsymbol{k}\cdot(R-R') - \beta\lambda\boldsymbol{k}^2\right], \quad 2\lambda\beta \ll L^2 \\
&= (2\pi)^{-dN}\int \mathrm{d}\boldsymbol{k}\ \exp\left[-i\boldsymbol{k}\cdot(R-R') - \beta\lambda\boldsymbol{k}^2\right] \\
&= (2\pi)^{-dN}\prod_{j=1}^{dN}\int \mathrm{d}k_j\ \exp\left[-ik_j(R-R')_j - \beta\lambda k_j^2\right] \\
&= (2\pi)^{-dN}\prod_{j=1}^{dN}\exp\left[-\frac{(R-R')_j^2}{4\lambda\beta}\right]\int \mathrm{d}z_j\ \exp\left[-\beta\lambda z_j^2\right] \\
&= (2\pi)^{-dN}\prod_{j=1}^{dN}\left(\frac{\pi}{\lambda\beta}\right)^{-1/2}\exp\left[-\frac{(R-R')_j^2}{4\lambda\beta}\right] \\
&= (4\pi\lambda\beta)^{-dN/2}\exp\left[-\frac{(R-R')^2}{4\lambda\beta}\right],
\end{aligned} \tag{1.36}$$

where we made a change of variables such that $k_j = z_j - i(R-R')_j/2\lambda\beta$ in order to obtain a gaussian integral. The result, Eq. (1.36), is the same we found earlier for N free particles in infinitely large space, i.e. Eq. (1.32). Here, it should be emphasized that if the condition $2\lambda\beta \ll L^2$ is violated one should use Eq. (1.34), Eq. (1.35) or add periodic "images" to Eq. (1.36), see Ceperley [1995].

1.3 Path integral

Path integrals offer an intuitive description of quantum mechanical phenomena such as quantum fluctuations, for example. The possibility to interpret quantum phenomena via path integrals stem from the fact that quantum mechanics or statistics is traced back in the formalism from a classical model. Thus, in some situations one may find classical reasoning to be enough also for definite quantum effects [Ceperley, 1995].

Here, we shall introduce the path integral formalism for a set of N distinguishable interacting particles. In order to shorten the equations all the particles are assumed to have the same mass, i.e. the same $\lambda = \hbar^2/2m$. The system may be thought of as consisting of N interacting electrons in the absence of a magnetic field.

1.3.1 Discrete path

The product property of the density matrix, Eq. (1.16), is the foundation of path integrals. If we apply the product property to the density matrix for M times and define $1/k_{\mathrm{B}}T = \beta = M\tau$, we may write a *discrete path* for the density matrix as

$$\begin{aligned}
&\rho(R, R'; \beta) \\
&= \int \mathrm{d}R_1 \mathrm{d}R_2 \cdots \mathrm{d}R_{M-1}\, \rho(R, R_1; \tau)\rho(R_1, R_2; \tau) \cdots \rho(R_{M-1}, R'; \tau) \\
&= \int \prod_{i=1}^{M-1} \mathrm{d}R_i \prod_{i=1}^{M} \rho(R_{i-1}, R_i; \tau),
\end{aligned} \tag{1.37}$$

where $R_0 = R$ and $R_M = R'$.

For N interacting particles the Hamiltonian is $\hat{H} = \hat{T} + \hat{V}$, where $\hat{T}$ is the kinetic energy operator and $\hat{V}$ the potential energy operator. Thus, we may represent the high temperature density matrix term in Eq. (1.37) as

$$\begin{aligned}
\rho(R_{i-1}, R_i; \tau) &= \langle R_{i-1}|e^{-\tau(\hat{T}+\hat{V})}|R_i\rangle \\
&= \langle R_{i-1}|e^{-\tau\hat{T}}e^{-\tau\hat{V}}e^{-\frac{\tau^2}{2}[\hat{T},\hat{V}]}|R_i\rangle \\
&\approx \langle R_{i-1}|e^{-\tau\hat{T}}e^{-\tau\hat{V}}|R_i\rangle.
\end{aligned} \tag{1.38}$$

The kinetic and potential operators do not commute, and therefore, the τ^2-dependence is usually neglected. Eq. (1.38), or in operator notation $e^{-\tau(\hat{T}+\hat{V})} \approx e^{-\tau\hat{T}}e^{-\tau\hat{V}}$, is known as the *primitive approximation*, which becomes exact in the limit $M \to \infty$, since according to Trotter [1959]

$$e^{-\beta(\hat{T}+\hat{V})} = \lim_{M\to\infty} \left[e^{-\tau\hat{T}}e^{-\tau\hat{V}}\right]^M. \tag{1.39}$$

The above is known as the *Trotter expansion*, which unfortunately is valid only for potentials bounded from below [Suzuki, 1976] — this will be discussed in more detail later in this thesis. There are also higher order approximations to separate the noncommutative operators, see for example DeRaedt and DeRaedt [1983] and Li and Broughton [1987]. For more information on the details of these expansions consult Leino [2007].

Within the primitive approximation the high temperature density matrix, Eq. (1.38),

may be written as

$$\begin{aligned}\rho(R_{i-1},R_i;\tau) &\approx \int \mathrm{d}R\ \langle R_{i-1}|e^{-\tau\hat{T}}|R\rangle\langle R|e^{-\tau\hat{V}}|R_i\rangle \\ &= \int \mathrm{d}R\ \langle R_{i-1}|e^{-\tau\hat{T}}|R\rangle e^{-\tau V(R)}\langle R|R_i\rangle \\ &= \int \mathrm{d}R\ \langle R_{i-1}|e^{-\tau\hat{T}}|R\rangle e^{-\tau V(R)}\delta(R,R_i) \\ &= \langle R_{i-1}|e^{-\tau\hat{T}}|R_i\rangle e^{-\tau V(R_i)} \\ &= \rho^{\mathrm{K}}(R_{i-1},R_i;\tau)e^{-\tau V(R_i)}. \end{aligned} \tag{1.40}$$

Thus, combining Eqs. (1.32), (1.37) and (1.40) we have for the discrete path of the density matrix

$$\rho(R,R';\beta) \approx \int \prod_{i=1}^{M-1}\mathrm{d}R_i \prod_{i=1}^{M} e^{-S(R_{i-1},R_i;\tau)}, \tag{1.41}$$

where $R_0 = R$ and $R_M = R'$, as above, and the *action* $S(R_{i-1},R_i;\tau)$ is

$$S(R_{i-1},R_i;\tau) = \frac{dN}{2}\ln(4\pi\lambda\tau) + \frac{(R_{i-1}-R_i)^2}{4\lambda\tau} + \tau V(R_i). \tag{1.42}$$

More about the *action* is discussed in the section Action.

1.3.2 Continuous path

In the case of *continuous path*, the Trotter expansion, i.e. Eq. (1.39), is used instead of the primitive approximation, Eq. (1.38). Thus, our density matrix is

$$\begin{aligned}\rho(R,R';\beta) &= \lim_{M\to\infty}\int \prod_{i=1}^{M-1}\mathrm{d}R_i \prod_{i=1}^{M} e^{-S(R_{i-1},R_i;\tau)} \\ &= \lim_{M\to\infty}\int \mathrm{d}R_1\mathrm{d}R_2\cdots\mathrm{d}R_{M-1}\ e^{-\sum_{i=1}^{M}S(R_{i-1},R_i;\tau)}, \end{aligned} \tag{1.43}$$

where $R_0 = R$, $R_M = R'$ and the action $S(R_{i-1},R_i;\tau)$ is as in Eq. (1.42). In addition, if we write the integrand as

$$\begin{aligned}&\exp\left\{-\sum_{i=1}^{M}S(R_{i-1},R_i;\tau)\right\} \\ &= (4\pi\lambda\tau)^{-dNM/2}\exp\left\{-\sum_{i=1}^{M}\left[\frac{(R_{i-1}-R_i)^2}{4\lambda\tau}+\tau V(R_i)\right]\right\} \\ &= (4\pi\lambda\tau)^{-dNM/2}\exp\left\{-\tau\sum_{i=1}^{M}\left[\frac{(R_{i-1}-R_i)^2}{4\lambda\tau^2}+V(R_i)\right]\right\}, \end{aligned} \tag{1.44}$$

and define the integral measure to be

$$\mathcal{D}R(\tau) = \lim_{M\to\infty} (4\pi\lambda\tau)^{-dNM/2}\, \mathrm{d}R_1 \mathrm{d}R_2 \cdots \mathrm{d}R_{M-1}, \tag{1.45}$$

we may change the summation in Eq. (1.44) into a Riemann integral in the limit of small τ. Thus, we obtain the *Feynman-Kac* formula

$$\begin{aligned}\rho(R, R'; \beta) &= \int \mathcal{D}R(\tau)\, \exp\left\{ -\int_0^\beta \mathrm{d}\tau\, \left(\frac{1}{4\lambda} \left[\frac{\mathrm{d}R(\tau)}{\mathrm{d}\tau} \right]^2 + V[R(\tau)] \right) \right\} \\ &= \int \mathcal{D}R(\tau)\, e^{-S[R(\tau)]}, \end{aligned} \tag{1.46}$$

which may also be written as

$$\rho(R, R'; \beta) = \rho^{\mathrm{K}}(R, R'; \beta) \left\langle e^{-\int_0^\beta \mathrm{d}\tau\, V[R(\tau)]} \right\rangle_{\mathrm{BRW}}, \tag{1.47}$$

where the BRW indicates that the average is taken over Brownian random walk, i.e. the free particle density matrix.

Chapter 2

Path integral Monte Carlo

Evaluation of the multidimensional path integrals is challenging, and usually, the conventional quadrature rules cannot be applied, in principle. Thus, the use of Monte Carlo integration becomes essential, and for canonical ensembles especially, the Metropolis Monte Carlo algorithm [Metropolis et al., 1953] is most suitable.

2.1 Metropolis Monte Carlo

In this section a brief introduction to a generalized Metropolis algorithm is given. For more detailed discussion an interested reader should consult especially Kalos and Whitlock [1986, 2008], and also, Ceperley [1995], Esler [2006], Leino [2007].

In chapter 2 it was shown that the density function or the probability for finding a system in a state represented by the configuration R is

$$Z^{-1}\rho(R, R; \beta). \tag{2.1}$$

According to the principle of *detailed balance* close to equilibrium the total rate of transitions from state R to R' equals that of the reverse rate, i.e.

$$P(R \to R')\frac{\rho(R, R; \beta)}{Z} = P(R' \to R)\frac{\rho(R', R'; \beta)}{Z}. \tag{2.2}$$

Considering the transition probability $P(R \to R')$ as a product of an *a priori* sampling probability $T(R \to R')$ and an acceptance probability $A(R \to R')$ we get

$$T(R \to R')A(R \to R')\rho(R, R; \beta) = T(R' \to R)A(R' \to R)\rho(R', R'; \beta). \tag{2.3}$$

The above can be written as

$$\frac{A(R \to R')}{A(R' \to R)} = \frac{T(R' \to R)\rho(R', R'; \beta)}{T(R \to R')\rho(R, R; \beta)} = q(R'|R) \geq 0, \tag{2.4}$$

of which the probability for accepting or rejecting a move is easily deduced. However, usually this is written in the form

$$A(R \to R') = \min\left[1, q(R'|R)\right]. \tag{2.5}$$

Thus, the generalized Metropolis Monte Carlo algorithm can be presented in the following way: at first the state of the system is $R_n = R$

- sample a possible new configuration R' using $T(R \to R')$
- calculate $q(R'|R)$
- if $A(R \to R') > \xi$, where $\xi \in [0, 1]$ is a uniformly distributed random number, set $R_{n+1} = R'$, i.e. the move is accepted
- otherwise, set $R_{n+1} = R_n = R$, that is, the move is rejected.

The system generated using the Metropolis algorithm is *ergodic* [Kalos and Whitlock, 1986, 2008], and thus, together with the principle of detailed balance the equilibrium distribution is sampled in the long time limit. Ergodicity ensures that any state R' can be reached from any other state, R, in a finite number of Monte Carlo moves.

Here, it should be emphasized that the most effective and uncorrelated sampling is given by sampling probability satisfying

$$\frac{T(R' \to R)}{T(R \to R')} = \frac{\rho(R, R; \beta)}{\rho(R', R'; \beta)}, \tag{2.6}$$

that is, $q = 1$ [Kalos and Whitlock, 1986, 2008]. Thus, a proper choice for the sampling probability is important, in practice.

2.1.1 Multilevel Metropolis algorithm

The Metropolis algorithm described above can be generalized to include multiple stages, or levels, in a Monte Carlo move. In path integral Monte Carlo the path is divided into M pieces with time step $\tau = \beta/M$, as described earlier. At each stage, s, some subset of the path is moved and accepted or rejected according to

$$A(R_s \to R'_s) = \min\left[1, \frac{q(R'_s|R_s)}{q(R'_{s-1}|R_{s-1})}\right]. \tag{2.7}$$

For the first stage $q(R'_{s-1}|R_{s-1}) = q(R'_0|R_0) = 1$, and thus, we have $A(R_1 \to R'_1) = \min\left[1, q(R'_1|R_1)\right]$.

If the move of some subset is accepted we continue to the next stage. If, however, the move of a subset is rejected at any stage the entire move is rejected and we proceed

to make a new move. As before, if the entire move is accepted, set $R_{n+1} = R'$, otherwise set $R_{n+1} = R_n = R$, where n refers to the number of Monte Carlo moves, not stages.

Apart from the last stage it is not required to have exact or the best approximation for q, since

$$\underbrace{q(R'_1|R_1)}_{1^{\text{st}}\text{ stage}} \underbrace{\left[\frac{q(R'_2|R_2)}{q(R'_1|R_1)}\right]}_{2^{\text{nd}}\text{ stage}} \underbrace{\left[\frac{q(R'_3|R_3)}{q(R'_2|R_2)}\right]}_{3^{\text{rd}}\text{ stage}} \cdots \underbrace{\left[\frac{q(R'_N|R_N)}{q(R'_{N-1}|R_{N-1})}\right]}_{\text{last stage}} = \underbrace{q(R'_N|R_N)}_{\text{overall}}, \quad (2.8)$$

that is, the intermediate stages cancel out. However, an improper approximation for q in intermediate stages might lead to problems with ergodicity — a move of some subset might be rejected eventhough the overall move would be accepted.

2.2 Action

As was shown in Eq. (1.37), in the path integral formalism the integrand consists of products of high temperature density matrices. These are usually expressed formally in terms of an object called *action*, which is defined as the natural logarithm of the density matrix

$$S(R_{i-1}, R_i; \tau) = -\ln \rho(R_{i-1}, R_i; \tau). \quad (2.9)$$

In addition, the action is conventionally separated into kinetic and interaction contributions

$$S(R_{i-1}, R_i; \tau) = K(R_{i-1}, R_i; \tau) + U(R_{i-1}, R_i; \tau), \quad (2.10)$$

where the kinetic term K is taken to be that of free particles, i.e.

$$K(R_{i-1}, R_i; \tau) = \frac{dN}{2} \ln(4\pi\lambda\tau) + \frac{(R_{i-1} - R_i)^2}{4\lambda\tau}, \quad (2.11)$$

where d is the dimensionality of the space. Everything else is left to the interaction term, which is usually unknown, since it also contains kinetic contributions of higher order in τ [Ceperley, 1995]. However, in the limit $\tau \to 0$ the interaction term consists solely of the potential energy terms of the system as was shown in the previous sections.

Good approximations for the interaction term enable the computations of larger and larger systems. One needs to find a way to include as much quantum information in that term as possible for the integral to be feasible to simulate — giving accurate expectation values in a reasonable time.

2.2.1 Pair approximation

The idea behind pair approximation stems from the statistical analysis: If two random variables X and Y are uncorrelated, then $\langle XY\rangle - \langle X\rangle\langle Y\rangle = 0$, i.e. the covariance is zero. This is, naturally, valid also for a set of uncorrelated random variables $\{X_i\}$. Thus, we may write

$$\left\langle \prod_i X_i \right\rangle = \prod_i \langle X_i\rangle \,. \tag{2.12}$$

The short-time, or high temperature, density matrix may be written as

$$\rho(R,R';\tau) = \rho^{\mathrm{K}}(R,R';\tau)\left\langle e^{-\int_0^\tau \mathrm{d}t\; V_{\mathrm{tot}}[R(t)]}\right\rangle_{\mathrm{BRW}}, \tag{2.13}$$

where BRW represents the average over all Brownian Random Walks, and ρ^{K} is the kinetic part of the density matrix, see Eq. (1.32). If the total potential energy can be expressed in terms of pair interactions, e.g. $V_{\mathrm{tot}}(R) = \sum_{i<j} V(\boldsymbol{r}_{ij})$, where $r_{ij} = |\boldsymbol{r}_{ij}|$ gives the distance between particles i and j, then the average over all BRWs is

$$\left\langle e^{-\int_0^\tau \mathrm{d}t\; V_{\mathrm{tot}}[R(t)]}\right\rangle_{\mathrm{BRW}} = \left\langle \prod_{i<j} e^{-\int_0^\tau \mathrm{d}t\; V(\boldsymbol{r}_{ij}(t))}\right\rangle_{\mathrm{BRW}\boldsymbol{r}_{ij}}. \tag{2.14}$$

Now, if we assume that the random variables $\exp\left[-\int_0^\tau \mathrm{d}t\; V(\boldsymbol{r}_{ij}(t))\right]$ in Eq. (2.14) are uncorrelated, then we can write the average as

$$\left\langle \prod_{i<j} e^{-\int_0^\tau \mathrm{d}t\; V(\boldsymbol{r}_{ij}(t))}\right\rangle_{\mathrm{BRW}\boldsymbol{r}_{ij}} = \prod_{i<j}\left\langle e^{-\int_0^\tau \mathrm{d}t\; V(\boldsymbol{r}_{ij}(t))}\right\rangle_{\mathrm{BRW}\boldsymbol{r}_{ij}}. \tag{2.15}$$

However, in practice we know that there are three and higher body correlations involved in the averaging. Therefore, we must write

$$\left\langle e^{-\int_0^\tau \mathrm{d}t V_{\mathrm{tot}}(R(t))}\right\rangle_{\mathrm{BRW}} \approx \prod_{i<j}\left\langle e^{-\int_0^\tau \mathrm{d}t\; V(\boldsymbol{r}_{ij}(t))}\right\rangle_{\mathrm{BRW}\boldsymbol{r}_{ij}}. \tag{2.16}$$

In the limit $\tau \to 0$, i.e. high temperature limit, equality is ensured in Eq. (2.16) by the Trotter expansion.

Identifying Eq. (2.16) with the equation

$$e^{-U(R,R';\tau)} \approx \prod_{i<j} e^{-u(\boldsymbol{r}_{ij},\boldsymbol{r}'_{ij};\tau)}, \tag{2.17}$$

we may write the approximate interaction part of the action U as a sum over all pairs i.e.

$$U(R, R'; \tau) = \sum_{i<j} u(\boldsymbol{r}_{ij}, \boldsymbol{r}'_{ij}; \tau). \tag{2.18}$$

Eq. (2.16) is called as the *pair approximation*, which is exact for a pair of particles. The errors for this approach stem from three and higher body correlations [Ceperley, 1995].

2.2.2 Primitive approximation

Further approximating Eq. (2.16), i.e.

$$\left\langle e^{-\int_0^\tau \mathrm{d}t V_{\mathrm{tot}}(R(t))} \right\rangle_{\mathrm{BRW}} \approx \prod_{i<j} \left\langle e^{-\int_0^\tau \mathrm{d}t\ V(\boldsymbol{r}_{ij}(t))} \right\rangle_{\mathrm{BRW}\boldsymbol{r}_{ij}},$$

we eventually end up to the primitive approximation, which is also the form given by the Trotter expansion. First, taking the average up to the exponent we have the so-called *cumulant approximation*, i.e.

$$\prod_{i<j} \left\langle e^{-\int_0^\tau \mathrm{d}t\ V(\boldsymbol{r}_{ij}(t))} \right\rangle_{\mathrm{BRW}\boldsymbol{r}_{ij}} \approx \prod_{i<j} e^{-\int_0^\tau \mathrm{d}t\ \langle V(\boldsymbol{r}_{ij}(t))\rangle_{\mathrm{BRW}\boldsymbol{r}_{ij}}}. \tag{2.19}$$

Second, taking the average over a classical trajectory, only, gives us the *semi-classical approximation*, that is,

$$\prod_{i<j} e^{-\int_0^\tau \mathrm{d}t\ \langle V(\boldsymbol{r}_{ij}(t))\rangle_{\mathrm{BRW}\boldsymbol{r}_{ij}}} \approx \prod_{i<j} e^{-\tau \int_0^1 \mathrm{d}s\ V\left(\boldsymbol{r}_{ij}^{(0)} + (\boldsymbol{r}_{ij}^{(1)} - \boldsymbol{r}_{ij}^{(0)})s\right)}, \tag{2.20}$$

where $\boldsymbol{r}_{ij}^{(0)}$ and $\boldsymbol{r}_{ij}^{(1)}$ are the end points of the classical trajectory.

Third, the *primitive approximation* is reached when we approximate the integral in the semi-classical approach by an averaged potential calculated at the end points, i.e.

$$\prod_{i<j} e^{-\tau \int_0^1 \mathrm{d}s\ V\left(\boldsymbol{r}_{ij}^{(0)} + (\boldsymbol{r}_{ij}^{(1)} - \boldsymbol{r}_{ij}^{(0)})s\right)} \approx \prod_{i<j} e^{-\frac{\tau}{2}\left[V(\boldsymbol{r}_{ij}^{(0)}) + V(\boldsymbol{r}_{ij}^{(1)})\right]}, \tag{2.21}$$

which is equivalent to the Trotter expansion, mentioned earlier. A thorough analysis of the pros and cons for the introduced approximations is given in Ceperley [1995].

2.3 Sampling the configuration space

How to effectively sample the full configuration space is one of the most important questions in Metropolis Monte Carlo simulations. The trivial choice of Metropolis et al. [1953] that $T(R \to R')$ is a uniform distribution, i.e. $T(R' \to R)/T(R \to R') = 1$, is inefficient in practice, and thus, should be avoided. Here, we will concentrate on the so-called *bisection move*, which together with the multilevel algorithm provide much more powerful sampling [Ceperley, 1995, Esler, 2006]. In addition, the so-called *displacement move* [Chakravarty et al., 1998] is briefly discussed.

2.3.1 Bisection move

Let us first define two new concepts: the bead and the time slice. The bead refers to a position of a particle and the time slice determines the place of the bead in the discrete path representing that particle — the discrete path is often referred to as a polymer [Ceperley, 1995].

In the bisection move the new position of a bead is determined in terms of the adjacent beads and a random number from a gaussian distribution. This will sample the free particle density matrix exactly, as is shown below.

Let us consider three consecutive time slices of a single particle: $\boldsymbol{r}_{i-1}$, $\boldsymbol{r}_i$ and $\boldsymbol{r}_{i+1}$. The positions $\boldsymbol{r}_{i-1}$ and $\boldsymbol{r}_{i+1}$ are fixed, and for the sampling probability we choose the normal distribution with mean $\bar{\boldsymbol{r}} = \frac{1}{2}(\boldsymbol{r}_{i-1} + \boldsymbol{r}_{i+1})$ and σ^2 variance. Thus, we have

$$T(\boldsymbol{r}_i \to \boldsymbol{r}_i') = \frac{1}{\sqrt{2\pi\sigma^2}} \exp\left[-\frac{(\boldsymbol{r}_i' - \bar{\boldsymbol{r}})^2}{2\sigma^2}\right] \tag{2.22}$$

and

$$T(\boldsymbol{r}_i' \to \boldsymbol{r}_i) = \frac{1}{\sqrt{2\pi\sigma^2}} \exp\left[-\frac{(\boldsymbol{r}_i - \bar{\boldsymbol{r}})^2}{2\sigma^2}\right]. \tag{2.23}$$

Now, $q(\boldsymbol{r}_i'|\boldsymbol{r}_i)$ in the acceptance probability, Eq. (2.5), can be written as

$$\begin{aligned} q(\boldsymbol{r}_i'|\boldsymbol{r}_i) &= \frac{T(\boldsymbol{r}_i' \to \boldsymbol{r}_i) e^{-S(\boldsymbol{r}_{i-1}, \boldsymbol{r}_i'; \tau) - S(\boldsymbol{r}_i', \boldsymbol{r}_{i+1}; \tau)}}{T(\boldsymbol{r}_i \to \boldsymbol{r}_i') e^{-S(\boldsymbol{r}_{i-1}, \boldsymbol{r}_i; \tau) - S(\boldsymbol{r}_i, \boldsymbol{r}_{i+1}; \tau)}} \\ &= \frac{T(\boldsymbol{r}_i' \to \boldsymbol{r}_i)}{T(\boldsymbol{r}_i \to \boldsymbol{r}_i')} e^{-\Delta K} e^{-\Delta U}, \end{aligned}$$

where

$$\begin{aligned}\Delta K &= K(\boldsymbol{r}_{i-1}, \boldsymbol{r}'_i; \tau) + K(\boldsymbol{r}'_i, \boldsymbol{r}_{i+1}; \tau) - K(\boldsymbol{r}_{i-1}, \boldsymbol{r}_i; \tau) - K(\boldsymbol{r}_i, \boldsymbol{r}_{i+1}; \tau) \\ &= \frac{1}{4\lambda\tau}\left[(\boldsymbol{r}_{i-1} - \boldsymbol{r}'_i)^2 + (\boldsymbol{r}'_i - \boldsymbol{r}_{i+1})^2 - (\boldsymbol{r}_{i-1} - \boldsymbol{r}_i)^2 - (\boldsymbol{r}_i - \boldsymbol{r}_{i+1})^2\right] \\ &= \frac{1}{4\lambda\tau}\, 2\left[(\boldsymbol{r}'_i)^2 - 2\boldsymbol{r}'_i\bar{\boldsymbol{r}} - \boldsymbol{r}_i^2 + 2\boldsymbol{r}_i\bar{\boldsymbol{r}}\right] \\ &= \frac{1}{2\lambda\tau}\left[(\boldsymbol{r}'_i - \bar{\boldsymbol{r}})^2 - (\boldsymbol{r}_i - \bar{\boldsymbol{r}})^2\right]. \end{aligned} \tag{2.24}$$

If we choose $\sigma^2 = \lambda\tau$, we have

$$\frac{T(\boldsymbol{r}'_i \to \boldsymbol{r}_i)}{T(\boldsymbol{r}_i \to \boldsymbol{r}'_i)} e^{-\Delta K} = 1 \quad \Longrightarrow \quad q(\boldsymbol{r}'_i|\boldsymbol{r}_i) = e^{-\Delta U}. \tag{2.25}$$

Therefore, choosing $\sigma^2 = \lambda\tau$ the kinetic part of the action is sampled exactly and need not be calculated at every Monte Carlo step — this is true for such cases where the gaussian form is proper for the kinetic part, i.e. for large enough simulation box.

2.3.2 Bisection move and multilevel algorithm

Bisection move together with the multilevel algorithm is an efficient sampling scheme. The basic idea is to choose a segment of the path of length $2^L + 1$, where L is the number of levels, or stages. The end beads of this segment are fixed and the beads in between will be moved.

The first bisection move is made for the middle bead. Thus, the time step is now $2^{L-1}\tau$, and for the variance of the sampling probability we should choose $\sigma^2 = 2^{L-1}\lambda\tau$. If the move is accepted then we have two segments of length $2^{L-1} + 1$ formed by the previous end beads and the bead just moved.

Next we will move the middle beads of these two segments similarly as described above. The time step is now $2^{L-2}\tau$, and the variance for the sampling probability is $\sigma^2 = 2^{L-2}\lambda\tau$. This will be continued until all the beads in the initial segment are moved or some of the moves is rejected.

The new bead position for a bisection move in the multilevel algorithm can be written as

$$\boldsymbol{r}'_i = \tfrac{1}{2}(\boldsymbol{r}_{i-2^{l-1}} + \boldsymbol{r}_{i+2^{l-1}}) + \eta\,\sqrt{2^{l-1}\lambda\tau}, \tag{2.26}$$

where η is a normally distributed random vector with zero mean and unit variance, and l is the number of levels left, e.g. at first stage $l = L$, which is the number of levels, at the second stage $l = L - 1$, at the third stage $l = L - 2$, ..., and at the last stage $l = 1$. With the above expression one should keep in mind that

$i \pm 2^{l-1} = \mathrm{mod}(i \pm 2^{l-1} - 1, M) + 1$, where M is the Trotter number. Also, one should notice that, excluding the initial segment, the positions of the end beads on the right-hand side have been updated in the previous levels.

For $L = 3$ the multilevel bisection move is

$$\underbrace{\left(e^{-\Delta U_{4\tau}}\right)}_{1^{\text{st}}\text{ stage}} \underbrace{\left(e^{-\Delta U_{2\tau}} e^{\Delta U_{4\tau}}\right)}_{2^{\text{nd}}\text{ stage}} \underbrace{\left(e^{-\Delta U_{\tau}} e^{\Delta U_{2\tau}}\right)}_{3^{\text{rd}}\text{ stage}} = \underbrace{e^{-\Delta U_{\tau}}}_{\text{overall}}, \tag{2.27}$$

which shows how one should check the acceptance at each level, or stage, and that the overall weight is $e^{-\Delta U_\tau}$, as it should.

As was mentioned earlier, only at the last stage or level the action needs to be accurate. A fast solution computationally is to use constant potential, i.e. $\Delta U = 0$, for all but the last stage. In this case, effective sampling is achieved with acceptance probability of about 50%. On the other hand, the better the stage action the faster the convergence.

2.3.3 Displacement move

In the displacement move the whole imaginary time path is moved for one or several particles by a random three-vector, i.e. the center-of-masses of the randomly selected polymer rings are moved. This kind of move is relevant especially in describing dissociation recombination reactions of a loosely bound molecule or a molecule at high enough temperature and low density.

2.4 Periodic boundary conditions

Due to the finite temperature present in path integral Monte Carlo simulations a simulation box is required, in principle, in order to properly simulate the NVT statistics of the system. Incorporation of a simulation box is usually accompanied with periodic boundary conditions. In many situations the *minimum image convention*, also called as the *nearest image convention*, is good enough. The minimum image convention states that all coordinates are considered to be taken modulo the box lengths, that is, a particle leaving the right side of the simulation box immediately reenters from the left, etc.

The use of periodic boundary conditions may introduce additional technical challenges if we are dealing with long-range interaction potentials, such as the Coulomb potential, for example. Then the calculation of the interactions of each particle is taken over all the periodic images of the particles, in addition to the others particles

in the simulation box. Special methods are needed for proper convergence [Ceperley, 1983, Esler, 2006]

However, it is fair to assume that the properties of a single atom or a molecule are also well described by using large enough simulation box and the minimum image convention — without the sum over images.

2.4.1 Finite size effects

Inclusion of the simulation box may also lead to so-called *finite size effects*. For example, simulations of a given density with different number of particles in simulation boxes may give unequal expectation values of an observable. The estimation of the finite size errors, however, is difficult to assess because the needed PIMC simulations are computationally much more demanding — converged results for paths corresponding to large systems can be challenging [Militzer and Ceperley, 2001].

Also, another effect arising from the finite size is related to the thermal de Broglie wave length, $\sqrt{2\lambda\beta}$. One should take care that the thermal wave length is small compared to the simulation box. A good example of the latter case is positron scattering from the H_2 molecule, i.e. low H_2 density, at about room temperature, $T = 293$ K. Simulations with one positron and one H_2 molecule in a cubic box ($V = L^3$) require relatively large simulation box since the positron in the system can almost be regarded as a free particle. The thermal wave length for the positron is $\lambda_{\text{th}} \approx 32.83a_0$, and thus, $L \gg \lambda_{\text{th}}$ is required, which is evident from simulation results: for instance, for the annihilation parameter, defined by [Gribakin et al., 2010]

$$Z_{\text{eff}} = a_0^{-3} \sum_{i=1}^{N_e} \int \mathrm{d}R \, \frac{\rho(R, R; \beta)}{Z} \delta(\mathbf{r}_i - \mathbf{r}_{e^+}), \tag{2.28}$$

where i refers to the i^{th} electron, we get $Z_{\text{eff}} = 9.98(26)$ for a box of volume $V = (30a_0)^3$ and $Z_{\text{eff}} = 15.3(8)$ for $V = (130a_0)^3$. The experimental values to be compared with are $14.61(14)$, $14.8(2)$ and $16.02(8)$ from references Laricchia et al. [1987], McNutt et al. [1979] and Wright et al. [1983], respectively.

2.5 Calculation of properties

Next, we shall briefly concentrate on the evaluation of quantum mechanical expectation values from path integral Monte Carlo simulations. First, we discuss about the diagonal properties, and second, we look into the most commonly used energy estimators, i.e. thermal and virial energy estimators. For an extensive analysis on the subject see Ceperley [1995].

2.5.1 Diagonal properties

According to Eq. (1.28) the expectation value of a diagonal observable is calculated as

$$\langle \hat{O} \rangle = Z^{-1} \int \mathrm{d}R_0 \; \rho(R_0, R_0; \beta) O(R_0). \tag{2.29}$$

Expressing the density function as a path integral we get

$$\langle \hat{O} \rangle = Z^{-1} \int \prod_{i=0}^{M-1} \mathrm{d}R_i \prod_{j=1}^{M} \rho(R_{j-1}, R_j; \beta) O(R_0), \tag{2.30}$$

where M is the Trotter number and $R_M = R_0$. Due to the symmetry in imaginary time all the time steps are equivalent [Ceperley, 1995], and thus, we may average over all time steps

$$\begin{aligned} \langle \hat{O} \rangle &= Z^{-1} \int \prod_{i=0}^{M-1} \mathrm{d}R_i \prod_{j=1}^{M} \rho(R_{j-1}, R_j; \beta) \frac{1}{M} \sum_{k=0}^{M-1} O(R_k) \\ &= \frac{1}{M} \sum_{k=0}^{M-1} Z^{-1} \int \prod_{i=0}^{M-1} \mathrm{d}R_i \prod_{j=1}^{M} \rho(R_{j-1}, R_j; \beta) O(R_k) \\ &= \frac{1}{M} \sum_{k=0}^{M-1} \langle O(R_k) \rangle. \end{aligned} \tag{2.31}$$

Therefore, using the equation above calculation of scalar operators, such as density, potential energy and pair correlation function, is straighforward. For example, the potential energy is simply

$$\langle V \rangle = \frac{1}{M} \sum_{k=0}^{M-1} \langle V(R_k) \rangle. \tag{2.32}$$

2.5.2 Thermal energy estimator

The thermal energy estimator is straightforwardly derived from the well known thermodynamical expression for the energy, that is,

$$\langle E_{\mathrm{T}} \rangle = -\frac{1}{Z} \frac{\partial Z}{\partial \beta}, \tag{2.33}$$

where the subscript T refers to Thermal. In path integral formalism the above can be written as

$$\begin{aligned}
\langle E_{\mathrm{T}} \rangle &= -\frac{1}{Z}\frac{\partial}{\partial\beta}\int \prod_{j=0}^{M-1} \mathrm{d}R_j \prod_{i=1}^{M} e^{-S(R_{i-1},R_i;\tau)} \\
&= -\frac{1}{Z}\frac{1}{M}\int \prod_{j=0}^{M-1} \mathrm{d}R_j \frac{\partial}{\partial\tau}\prod_{i=1}^{M} e^{-S(R_{i-1},R_i;\tau)} \\
&= \frac{1}{Z}\frac{1}{M}\int \prod_{j=0}^{M-1} \mathrm{d}R_j \frac{\partial \sum_{k=1}^{M} S(R_{k-1},R_k;\tau)}{\partial\tau}\prod_{i=1}^{M} e^{-S(R_{i-1},R_i;\tau)} \\
&= \frac{1}{M}\sum_{k=1}^{M}\left\langle \frac{\partial S(R_{k-1},R_k;\tau)}{\partial\tau}\right\rangle . \qquad (2.34)
\end{aligned}$$

Thus, the thermal energy estimator is the average of the τ-derivatives of the link actions $S(R_{k-1}, R_k; \tau)$ defined in Eqs. (2.9), (2.10) and (2.11). Taking the derivative yields

$$\langle E_{\mathrm{T}} \rangle = \frac{1}{M}\sum_{k=1}^{M}\left\langle \frac{dN}{2\tau} - \frac{(R_{k-1}-R_k)^2}{4\lambda\tau^2} + \frac{\partial U(R_{k-1},R_k;\tau)}{\partial\tau}\right\rangle . \qquad (2.35)$$

For the *primitive approximation* the τ-derivative of the potential action equals the average $\frac{1}{2}\left[V(R_{k-1}) + V(R_k)\right]$, and hence, the thermal energy estimator for the primitive approximation is

$$\langle E_{\mathrm{T}} \rangle = \frac{1}{M}\sum_{k=1}^{M}\left\langle \frac{dN}{2\tau} - \frac{(R_{k-1}-R_k)^2}{4\lambda\tau^2} + V(R_k)\right\rangle . \qquad (2.36)$$

2.5.3 Virial energy estimator

The novel idea behind the virial energy estimator is to transform the kinetic term in Eq. (2.35) into something that might fluctuate less. A general expression is derived in Ceperley [1995], Appendix A. Here, however, we shall go through the derivation for the primitive approximation as in Herman et al. [1982], only.

We begin with

$$\begin{aligned}
&\left\langle \sum_{k=0}^{M-1} R_k \nabla_k S \right\rangle \\
&= Z^{-1} \int \prod_{j=0}^{M-1} \mathrm{d}R_j \left(\sum_{k=0}^{M-1} R_k \nabla_k S \right) e^{-S} \\
&= Z^{-1} \sum_{k=0}^{M-1} \int \prod_{j=0}^{M-1} \mathrm{d}R_j \; R_k \left(-\nabla_k e^{-S} \right) \\
&= -Z^{-1} \sum_{k=0}^{M-1} \int \prod_{\substack{j=0 \\ j\neq k}}^{M-1} \mathrm{d}R_j \int \mathrm{d}R_k \; R_k \nabla_k e^{-S} \\
&= -Z^{-1} \sum_{k=0}^{M-1} \int \prod_{\substack{j=0 \\ j\neq k}}^{M-1} \mathrm{d}R_j \left\{ \text{substitution part } - Nd \int \mathrm{d}R_k \; e^{-S} \right\}, \qquad (2.37)
\end{aligned}$$

where N is the number of particle, d is the dimensionality and the substitution part is

$$\text{substitution part } = \sum_{n=1}^{N} \sum_{m=1}^{d} \int \mathrm{d}R_{k,n,m} \Big[R_{k,n,m} e^{-S} \Big]_{R_k^i}^{R_k^f}, \qquad (2.38)$$

where $\mathrm{d}R_{k,m,n}$ is a $d-1$ dimensional differential measure for the n^{th} particle in the time slice k. For example, for a particle in three dimensions one substitution term would be $\int \mathrm{d}x\mathrm{d}y[z\exp(-S)]_{z_i}^{z_f}$, and another would be $\int \mathrm{d}x\mathrm{d}z[y\exp(-S)]_{y_i}^{y_f}$. Thus, we may write

$$\left\langle \sum_{k=0}^{M-1} R_k \nabla_k S \right\rangle = MNd - \Upsilon, \qquad (2.39)$$

where Υ refers to the surface term. For some cases, e.g. particle confined in a volume with reflected boundaries, the surface term gives rise to an observable pressure [Leino, 2007]. This will be shown shortly for the case of Coulomb interactions. For now, let's assume the substitution part is zero [Herman et al., 1982], i.e.

$$\left\langle \sum_{k=0}^{M-1} R_k \nabla_k S \right\rangle = MNd. \qquad (2.40)$$

On the other hand, the expectation value can also be written as

$$\left\langle \sum_{k=0}^{M-1} R_k \nabla_k S \right\rangle = \left\langle \sum_{k=0}^{M-1} R_k \nabla_k K \right\rangle + \left\langle \sum_{k=0}^{M-1} R_k \nabla_k U \right\rangle. \qquad (2.41)$$

The kinetic action may be expressed as $K = \text{constant} + \tilde{K}$, where

$$\text{constant} = \frac{dNM}{2} \ln(4\pi\lambda\tau)$$

and

$$\tilde{K} = \sum_{i=0}^{M-1} \frac{(R_i - R_{i+1})^2}{4\lambda\tau}. \tag{2.42}$$

For the primitive approximation $U = \tau \sum_{i=0}^{M-1} V(R_i)$, and thus, $\nabla_k U = \tau \nabla_k V(R_k)$. Since [Herman et al., 1982]

$$\sum_{i=0}^{M-1} x_i \frac{\partial}{\partial x_i}(x_i - x_{i+1})^2 = 2 \sum_{i=1}^{M-1} (x_i - x_{i+1})^2, \tag{2.43}$$

we may write $R_k \nabla_k K = R_k \nabla_k \tilde{K} = 2\tilde{K}$. Inserting Eq. (2.40) to Eq. (2.41) with the shown modifications we have

$$MNd = \langle 2\tilde{K} \rangle + \left\langle \tau \sum_{k=0}^{M-1} R_k \nabla_k V(R_k) \right\rangle. \tag{2.44}$$

This can be further modified to give

$$\begin{aligned} \frac{1}{M} \sum_{k=0}^{M-1} \left\langle \frac{1}{2} R_k \nabla_k V(R_k) \right\rangle &= \left\langle \frac{MNd}{2\beta} - \frac{1}{\beta}\tilde{K} \right\rangle \\ &= \frac{1}{M} \sum_{k=0}^{M-1} \left\langle \frac{dN}{2\tau} - \frac{(R_k - R_{k+1})^2}{4\lambda\tau^2} \right\rangle, \end{aligned} \tag{2.45}$$

where on the right we have the thermal kinetic energy estimator. Thus, the virial total energy estimator for the primitive approximation can be written as

$$\langle E_{\mathrm{V}} \rangle = \frac{1}{M} \sum_{k=0}^{M-1} \left\langle \frac{1}{2} R_k \nabla_k V(R_k) + V(R_k) \right\rangle, \tag{2.46}$$

where V stands for Virial.

Observable pressure: Coulomb interaction

A fully nonadiabatic simulation for a system where particles are interacting via the Coulomb interactions only, Eq. (2.46) simplifies to $\langle E_{\mathrm{V}} \rangle = \langle V \rangle / 2$, i.e. only the

potential energy needs to be calculated, which speeds up simulations and lowers the variance. However, according to Feynman [1972, 1998]

$$3pV = 2\langle T\rangle + \langle V\rangle, \tag{2.47}$$

which would indicate zero pressure when $\langle E_{\rm V}\rangle = \langle V\rangle/2$. Using Eq. (2.39) we may relate the surface term Υ to pressure. First, including the surface term to Eq. (2.45) we may write

$$\langle T_{\rm V}\rangle - \langle T_{\rm T}\rangle = -\frac{\Upsilon}{2\beta}. \tag{2.48}$$

Adding the term $3(\langle T_{\rm T}\rangle - \langle T_{\rm V}\rangle)$, that equals $3\Upsilon/2\beta$, to both sides gives

$$2\langle T_{\rm T}\rangle - 2\langle T_{\rm V}\rangle = \frac{\Upsilon}{\beta}. \tag{2.49}$$

Since, now $-2\langle T_{\rm V}\rangle = \langle V\rangle$, we have

$$2\langle T_{\rm T}\rangle + \langle V\rangle = \frac{\Upsilon}{\beta}, \tag{2.50}$$

and thus,

$$3pV = \frac{\Upsilon}{\beta}. \tag{2.51}$$

Therefore, the virial energy estimator of Eq. (2.46) is most appropriate in describing molecular properties of, for example, a molecule in a large enough simulation box.

2.6 Ensemble average and error estimate

In a path integral Monte Carlo simulation one estimates the expectation value of an observable $\hat{O}$ according to equations given above at every Monte Carlo step — or with some frequency, e.g. at every 100 MC steps. The longer the simulation the more statistical accuracy is obtained.

For the total simulation with N MC steps the expectation value or ensemble average is simply the *sample mean*

$$\langle\hat{O}\rangle = \frac{1}{N}\sum_{i=1}^{N} O_i, \tag{2.52}$$

where O_i is the expectation value of the i^{th} MC step. If the simulation data O_i are uncorrelated the standard error of the mean (SEM) is given by

$$\text{SEM} = \frac{s}{\sqrt{N}}, \tag{2.53}$$

where s is the square root of the *sample variance*

$$s^2 = \frac{1}{N-1}\sum_{i=1}^{N}(O_i - \langle\hat{O}\rangle)^2. \tag{2.54}$$

Most often, however, the Monte Carlo simulation data is correlated, as implied in section 2.1. The correlation can be taken into account by a coefficient called correlation time κ. Now, the SEM is expressed as

$$\text{SEM} = s\sqrt{\frac{\kappa}{N}}, \tag{2.55}$$

where the correlation time is given in terms of the autocorrelation time $C(\Delta t)$ as

$$\kappa = 1 + 2\sum_{\Delta t=1}^{\infty} C(\Delta t). \tag{2.56}$$

For a discrete data set the autocorrelation time can be estimated using

$$C(k) \approx \frac{1}{(N-k)s^2}\sum_{t=1}^{N-k}\left[\left(O_t - \langle\hat{O}\rangle\right)\left(O_{t+k} - \langle\hat{O}\rangle\right)\right]. \tag{2.57}$$

In practice, the infinite summation in Eq. (2.56) can be approximated by taking the sum from 1 to N, only. Also, if the autocorrelation time is negative for some $k = m < N$ the summation is taken up to $m - 1$.

Chapter 3

Coulombic systems

The direct application of the path integrals, i.e. the primitive approximation, suffer from problems due to the Coulomb singularity — the attractive Coulomb potential is not bounded from below as is required by the Trotter formula. Here, we address this issue and show how this is solved by the pair approximation introduced in Chapter 2.

3.1 Pair density

For a pair of particles ($R = \{\boldsymbol{r}_1,\ \boldsymbol{r}_2\}$) one may write the density matrix in terms of its center of mass (c.m.) coordinates and those for the relative motion as

$$\rho(R, R'; \tau) = \rho_{\text{c.m.}}(\boldsymbol{r}_{\text{c.m.}}, \boldsymbol{r}'_{\text{c.m.}}; \tau)\rho_{\text{rel}}(\boldsymbol{r}, \boldsymbol{r}'; \tau), \tag{3.1}$$

where $\boldsymbol{r}_{\text{c.m.}} = (m_1\boldsymbol{r}_1 + m_2\boldsymbol{r}_2)/(m_1 + m_2)$ and $\boldsymbol{r} = \boldsymbol{r}_1 - \boldsymbol{r}_2$. In addition, for any central potential the density matrix $\rho_{\text{rel}}(\boldsymbol{r}, \boldsymbol{r}'; \tau)$ may be expanded in partial waves as [Storer, 1968]

$$\rho_{\text{rel}}(\boldsymbol{r}, \boldsymbol{r}'; \tau) = \frac{1}{4\pi r r'} \sum_{l=0}^{\infty} (2l+1)\rho_l(r, r'; \tau) P_l(\cos(\theta)), \tag{3.2}$$

where $P_l(x)$ is the lth Legendre polynomial, θ is the angle between vectors $\boldsymbol{r}$ and $\boldsymbol{r}'$, and ρ_l is the pair density matrix, which is a solution to the Bloch equation

$$-\frac{\partial \rho_l(r, r'; \tau)}{\partial \tau} = \left[-\lambda \frac{\partial^2}{\partial r^2} + v(r) + \frac{\lambda l(l+1)}{r^2}\right] \rho_l(r, r'; \tau), \tag{3.3}$$

with appropriate boundary conditions: $\rho_l(r, r'; \tau) = \delta(\tau)\delta(r - r')$ and $\rho_l(0, r'; \tau) = 0$ [Ceperley, 1995].

The pair density matrix may be expressed, for example, using the radial eigenfunctions, i.e.

$$\rho_l(r,r';\tau) = \sum_n \psi_n(r)^* e^{-\tau E_n} \psi_n(r') + \int_0^\infty \mathrm{d}k\ \psi_k(r)^* e^{-\tau E_k} \psi_k(r'), \tag{3.4}$$

where summation index $n = \{n, l\}$ and $k = \{k, l\}$. In practice this computation may become an unmanageable task. Another way — a bit more popular approach — to compute the pair density matrix is called *matrix squaring*, which is introduced later.

3.1.1 Free particle

Now, for future reference, it is useful to introduce the pair density matrix of a free particle [Ceperley, 1995]

$$\rho_l^{\mathrm{K}}(r,r';\tau) = \frac{4\pi r r'}{(4\pi\lambda\tau)^{3/2}} \exp\left(-\frac{r^2+r'^2}{4\lambda\tau}\right) i_l\left(\frac{rr'}{2\lambda\tau}\right), \tag{3.5}$$

where $i_l(x)$ is the lth modified spherical Bessel function of the first kind.

For the free particle the summation over partial waves, Eq. (3.2) may be performed exactly [Ceperley, 1995]

$$\begin{aligned}\rho_{\mathrm{rel}}^{\mathrm{K}}(\boldsymbol{r},\boldsymbol{r}';\tau) &= \frac{1}{4\pi r r'} \sum_{l=0}^{\infty} (2l+1) \rho_l^{\mathrm{K}}(r,r';\tau) P_l(\cos(\theta)) \\ &= (4\pi\lambda\tau)^{-3/2} \exp\left(-\frac{|\boldsymbol{r}-\boldsymbol{r}'|^2}{4\lambda\tau}\right).\end{aligned} \tag{3.6}$$

Generally, however, the summation has to be approximated.

3.1.2 Coulombic

In case of the Coulomb interaction, it has been shown [Hostler and Pratt, 1963, Storer, 1968] that the relative motion density matrix can be obtained from equations

$$\rho_{\mathrm{rel}}(\boldsymbol{r},\boldsymbol{r}';\tau) = -\frac{1}{8\pi s}\frac{\partial}{\partial s}\rho_0(z+s, z-s;\tau) \tag{3.7a}$$

$$\rho_{\mathrm{rel}}(\boldsymbol{r},\boldsymbol{r};\tau) = -\frac{1}{8\pi}\frac{\partial^2}{\partial s^2}\rho_0(z+s, z-s;\tau)|_{s=0}, \tag{3.7b}$$

where $z = (x+y)/2$, $s = (x-y)/2$, $x = (r + r' + |\boldsymbol{r}-\boldsymbol{r}'|)/2$ and $y = (r + r' - |\boldsymbol{r}-\boldsymbol{r}'|)/2$. The off-diagonal term, Eq. (3.7a), may also be written as

$$\rho_{\mathrm{rel}}(\boldsymbol{r},\boldsymbol{r}';\tau) = -\frac{1}{4\pi(x-y)}\Big(\frac{\partial}{\partial x} - \frac{\partial}{\partial y}\Big)\rho_0(x,y;\tau). \tag{3.8}$$

The importance of this presentation lies in the fact that only the first ($l = 0$) pair density matrix is needed to obtain the desired density matrix. The above equation is derived in Appendix A, also.

Numerical evaluations of the Coulomb density matrix using this approach are found, for example, in Storer [1968] and Pollock [1988]. Storer [1968] shows how to obtain the Coulombic density matrix with the matrix squaring technique. Pollock [1988] instead, does the evaluation using partial waves.

3.2 Pair potential

In the previous sections, the means to construct the density matrix for relative motion of a two particle system was introduced. The effective pair potential for the Coulomb interaction, required by the pair approximation, may now be derived from the equation

$$\rho_{\text{rel}}(\boldsymbol{r},\boldsymbol{r}';\tau) = \rho^{\text{K}}_{\text{rel}}(\boldsymbol{r},\boldsymbol{r}';\tau)\rho^{\text{U}}_{\text{rel}}(\boldsymbol{r},\boldsymbol{r}';\tau) = \rho^{\text{K}}_{\text{rel}}(\boldsymbol{r},\boldsymbol{r}';\tau)\exp\left[-u(\boldsymbol{r},\boldsymbol{r}';\tau)\right]. \quad (3.9)$$

Thus, the effective potential is

$$u(\boldsymbol{r},\boldsymbol{r}';\tau) = -\ln\left[\frac{\rho_{\text{rel}}(\boldsymbol{r},\boldsymbol{r}';\tau)}{\rho^{\text{K}}_{\text{rel}}(\boldsymbol{r},\boldsymbol{r}';\tau)}\right] = S_{\text{rel}}(\boldsymbol{r},\boldsymbol{r}';\tau) - K_{\text{rel}}(\boldsymbol{r},\boldsymbol{r}';\tau). \quad (3.10)$$

3.2.1 Properties of the Coulomb pair potential

Next we will consider some analytically obtainable information about the effective potential introduced in Eq. (3.10) for the Coulomb interaction. First, the value at the origin, as well as the behaviour near the origin, is shown as in Pollock [1988]. Second, the diagonal terms are looked into.

Behaviour at the origin

Pollock [1988] showed for the repulsive Coulomb interaction that the density matrix at the origin is

$$\begin{aligned}\rho_{\text{rel}}(0,0;\tau) &= \frac{|Z_1Z_2|^3}{2\pi\lambda^3}\int_0^\infty \mathrm{d}k\,\frac{ke^{-\gamma k^2}}{e^{\pi/k}-1} \\ &= \frac{|Z_1Z_2|^3}{\lambda^3(4\pi\gamma)^{3/2}}\left[1-(\pi\gamma)^{1/2}+\sum_{j=0}^{\infty}\frac{(-1)^j}{j!}\left(\frac{j}{2}\right)!\zeta(j+2)\gamma^{j/2+1}\right],\end{aligned}$$

where $\gamma = \tau(Z_1 Z_2)^2/\lambda$ and ζ is the Riemann zeta function. Comparing the expression above to a cumulant expansion, i.e.

$$\begin{aligned}
&\rho_{\text{rel}}(0,0;\tau) \\
&= \frac{|Z_1 Z_2|^3}{\lambda^3 (4\pi\gamma)^{3/2}} \exp\left(-\sum_{j=1}^{\infty} P_j \gamma^{j/2}\right) \\
&= \frac{|Z_1 Z_2|^3}{\lambda^3 (4\pi\gamma)^{3/2}} \left[1 - P_1\gamma^{j/2} + \left(\frac{1}{2!}P_1^2 - P_2\right)\gamma - \left(\frac{1}{3!}P_1^3 + P_3 - P_1 P_2\right)\gamma^{3/2} + \ldots\right],
\end{aligned}$$

we may write the effective potential for the repulsive Coulomb interaction at the origin as

$$u(0,0;\tau) = \sum_{j=1}^{\infty} P_j \gamma^{j/2}, \tag{3.11}$$

the coefficients being $P_1 = \sqrt{\pi}$, $P_2 = \frac{1}{2}\pi - \zeta(2) = \frac{1}{2}\pi - \frac{1}{6}\pi^2$, $P_3 = \frac{1}{3}\pi^{3/2} - \frac{1}{6}\pi^{5/2} + \frac{1}{2}\sqrt{\pi}\,\zeta(3)$, etc. See Table 3.1 for numerical values up to $j = 8$. These values clearly demonstrate the rapid convergence of the cumulant expansion.

More generally the effective potential at the origin is expressed as

$$u(0,0;\tau) = \sum_{j=1}^{\infty} (\pm 1)^j P_j \gamma^{j/2}, \tag{3.12}$$

where $+$ is for the repulsive and $-$ for the attractive case. This indicates that choosing the free particle action as the kinetic action we end up with an effective Coulomb potential which is non-singular at the origin.

Behaviour near the origin

Examination of the most divergent terms in the Bloch equation near the origin results in the *cusp*-condition [Pollock, 1988]

$$\lim_{\substack{r\to 0 \\ r'\to 0}} u(r,r';\tau) = u(0,0;\tau) - \frac{Z_1 Z_2}{2\lambda}(r + r'). \tag{3.13}$$

The second term on the right-hand side is simply the $1s$-orbital contribution to the density matrix.

Table 3.1: Coefficients P_j for Eq. (3.11)

P_1	1.772453851
P_2	-0.074137740
P_3	0.005834805
P_4	-0.000382686
P_5	0.000008738
P_6	0.000002138
P_7	-0.000000356
P_8	0.000000021

Diagonal of the effective potential

For the diagonal terms it is now possible to lay out three conditions of which the last one is exact in the limit $\tau \to 0$, only,

$$u(0,0;\tau) = \sum_{j=1}^{\infty} (\pm 1)^j P_j \gamma^{j/2} \tag{3.14a}$$

$$\frac{\mathrm{d}u(r,r;\tau)}{\mathrm{d}r}\Big|_{r=0} = -\frac{Z_1 Z_2}{\lambda} \tag{3.14b}$$

$$u(r,r;\tau) \approx \tau \frac{Z_1 Z_2}{r} \quad \text{, for } r \geq r_c, \tag{3.14c}$$

where r_c is some cut-off radius.

3.3 Matrix squaring

In this section, a brief introduction to the basic theory of the matrix squaring is given, first. Second, the matrix squaring is looked into in a different way in order to obtain as much accuracy as possible.

3.3.1 Basic principle

Theory

The basic idea of the matrix squaring is to obtain a low temperature pair density matrix using that of a high temperature. Let us assume we know the pair density matrix at the inverse temperature $\tau = \beta/M$ and we want to have it at β. Using the

product property once, we have

$$\rho_l(r, r'; 2\tau) = \int_0^\infty \mathrm{d}r'' \rho_l(r, r''; \tau)\rho_l(r'', r'; \tau), \tag{3.15}$$

which is the density matrix at a lower temperature ($T \to T/2$). Applying the same property for n times recursively we obtain the desired density matrix $\rho_l(r, r'; M\tau) = \rho_l(r, r'; \beta)$, where $M = 2^n$. For more details, see for example Storer [1968] and Klemm and Storer [1973].

Practice

The simple theory of the matrix squaring has a great deal of limiting factors in practice. For example, we do not (usually) know the high temperature pair density matrix, and the integral in Eq. (3.15) cannot be integrated all the way to infinity. At a high enough temperature, however, the primitive and semi-classical approximations may be considered accurate. Thus, the first practical problem is solved.

The matrix squaring procedure is basically a two step process:

1. Compute the initial pair density matrix using a high-temperature approximation (e.g. the semi-classical approximation)

   $$\rho_l(r, r'; \tau) \approx \rho_l^{\mathrm{K}}(r, r'; \tau) \exp\left(-\frac{\tau}{r' - r}\int_r^{r'} V(x)\mathrm{d}x\right),$$

   where $\rho_l^{\mathrm{K}}(r, r'; \tau)$ is the free-particle pair density matrix, see Eq. (3.5).

   - Remember the boundary value $\rho_l(0, r'; \tau) = 0$, see Eq. (3.3).

2. Do the required amount of squaring procedures

   $$\rho_l(r, r'; 2\tau) = \int_0^{r_c} \mathrm{d}r'' \rho_l(r, r''; \tau)\rho_l(r'', r'; \tau) + \int_{r_c}^\infty \mathrm{d}r'' F(r, r', r''; \tau),$$

   where the second term on the right is some analytically solvable approximation, for instance [Storer, 1968].

Numerically the previous using a uniform grid and Riemann summation is

1. Make an N by N matrix ρ using the semi-classical approximation at the inverse temperature τ.

2. Compute iteratively as many times as it is required the matrix-matrix product $\rho(\tau)\rho(\tau)$ multiplied by the grid spacing Δx,

$$\begin{aligned}\rho(2\tau) &= \rho(\tau)\rho(\tau)\Delta x,\\ \rho(4\tau) &= \rho(2\tau)\rho(2\tau)\Delta x,\\ &\vdots\\ \rho(M\tau) &= \rho(\tfrac{M}{2}\tau)\rho(\tfrac{M}{2}\tau)\Delta x,\end{aligned}$$

and at each step compute to every matrix element the approximated value of the integral from r_c to infinity.

3.3.2 Advanced

The basic matrix squaring method where the partial wave density matrix is integrated in a two dimensional uniform grid loses a lot of accuracy, since the density matrix is very sharply peaked along the diagonal. Thus, the grid should have extremely small spacing in order to store the matrix accurately, which is not desirable.

One way to overcome this loss of accuracy is introduced in the Thesis by Esler [2006], which is shown here also, but with slightly different notation.

"Squaring the potential"

Instead of squaring the partial density matrix, it is better to "square" only the potential term, which is much more well behaved — no sharp peaks. The procedure starts with the same product property as before.

$$\begin{aligned}&\rho_l(r,r';2\tau) = \int_0^\infty \mathrm{d}r''\rho_l(r,r'';\tau)\rho_l(r'',r';\tau)\\
&\Leftrightarrow\ \rho_l^{\mathrm{K}}(r,r';2\tau)e^{-u_l(r,r';2\tau)} = \int_0^\infty \mathrm{d}r''\rho_l^{\mathrm{K}}(r,r'';\tau)\rho_l^{\mathrm{K}}(r'',r';\tau)e^{-u_l(r,r'';\tau)-u_l(r'',r';\tau)}\\
&\Leftrightarrow\ e^{-u_l(r,r';2\tau)} = \int_0^\infty \mathrm{d}r''\frac{\rho_l^{\mathrm{K}}(r,r'';\tau)\rho_l^{\mathrm{K}}(r'',r';\tau)}{\rho_l^{\mathrm{K}}(r,r';2\tau)}e^{-u_l(r,r'';\tau)-u_l(r'',r';\tau)}\\
&\Leftrightarrow\ u_l(r,r';2\tau) = -\ln\left[\int_0^\infty \mathrm{d}r''\frac{\rho_l^{\mathrm{K}}(r,r'';\tau)\rho_l^{\mathrm{K}}(r'',r';\tau)}{\rho_l^{\mathrm{K}}(r,r';2\tau)}e^{-u_l(r,r'';\tau)-u_l(r'',r';\tau)}\right]\\
&\Leftrightarrow\ u_l(r,r';2\tau) = -\ln\left[\int_0^\infty \mathrm{d}r''I(r,r',r'';\tau)e^{-u_l(r,r'';\tau)-u_l(r'',r';\tau)}\right], \qquad (3.16)\end{aligned}$$

where

$$I(r,r',r'';\tau) = \frac{\rho_l^{\mathrm{K}}(r,r'';\tau)\rho_l^{\mathrm{K}}(r'',r';\tau)}{\rho_l^{\mathrm{K}}(r,r';2\tau)}. \qquad (3.17)$$

Trivially the free particle part of the integrand $I(r, r', r''; \tau)$ integrates to 1:

$$\begin{aligned}\int_0^\infty \mathrm{d}r'' I(r, r', r''; \tau) &= \int_0^\infty \mathrm{d}r'' \frac{\rho_l^{\mathrm{K}}(r, r''; \tau)\rho_l^{\mathrm{K}}(r'', r'; \tau)}{\rho_l^{\mathrm{K}}(r, r'; 2\tau)} \\ &= \frac{\int_0^\infty \mathrm{d}r'' \rho_l^{\mathrm{K}}(r, r''; \tau)\rho_l^{\mathrm{K}}(r'', r'; \tau)}{\rho_l^{\mathrm{K}}(r, r'; 2\tau)} \\ &= \frac{\rho_l^{\mathrm{K}}(r, r'; 2\tau)}{\rho_l^{\mathrm{K}}(r, r'; 2\tau)} \\ &= 1. \end{aligned} \tag{3.18}$$

Since the free particle density matrix is known analytically, the $I(r, r', r''; \tau)$ term in the integrand is easily evaluated. Thus, only the potential needs to be tabulated — and during the integration it also should be interpolated.

Modified integrand

In order to be computationally relatively effective the analytical part of the integrand should be modified. Let's first write down the free particle partial density matrix in a computationally favourable form.

$$\begin{aligned}\rho_l^{\mathrm{K}}(r, r'; \tau) &= \frac{4\pi r r'}{(4\pi\lambda\tau)^{3/2}} \exp\left(-\frac{r^2 + r'^2}{4\lambda\tau}\right) i_l\left(\frac{r r'}{2\lambda\tau}\right) \\ &= \frac{4\pi r r'}{(4\pi\lambda\tau)^{3/2}} \exp\left(-\frac{r^2 + r'^2}{4\lambda\tau}\right) i_l\left(\frac{r r'}{2\lambda\tau}\right) \exp\left(\frac{r r'}{2\lambda\tau}\right) \exp\left(-\frac{r r'}{2\lambda\tau}\right) \\ &= \frac{4\pi r r'}{(4\pi\lambda\tau)^{3/2}} \exp\left(-\frac{(r - r')^2}{4\lambda\tau}\right) i_l\left(\frac{r r'}{2\lambda\tau}\right) \exp\left(-\frac{r r'}{2\lambda\tau}\right) \\ &= \frac{4\pi r r'}{(4\pi\lambda\tau)^{3/2}} \exp\left(-\frac{(r - r')^2}{4\lambda\tau}\right) m_l\left(\frac{r r'}{2\lambda\tau}\right), \end{aligned} \tag{3.19}$$

where $m_l(z) = i_l(z)e^{-z},\ z \geq 0$.

In terms of Eq. (3.19) the free particle part of the integrand is

$$\begin{aligned} & I(r, r', r''; \tau) \\ &= \frac{\rho_l^{\mathrm{K}}(r, r''; \tau)\rho_l^{\mathrm{K}}(r'', r'; \tau)}{\rho_0^{\mathrm{K}}(r, r'; 2\tau)} \\ &= \frac{\frac{4\pi r r''}{(4\pi\lambda\tau)^{3/2}} \exp\left(-\frac{(r-r'')^2}{4\lambda\tau}\right) m_l\left(\frac{r r''}{2\lambda\tau}\right) \frac{4\pi r'' r'}{(4\pi\lambda\tau)^{3/2}} \exp\left(-\frac{(r''-r')^2}{4\lambda\tau}\right) m_l\left(\frac{r'' r'}{2\lambda\tau}\right)}{\frac{4\pi r r'}{(8\pi\lambda\tau)^{3/2}} \exp\left(-\frac{(r-r')^2}{8\lambda\tau}\right) m_l\left(\frac{r r'}{4\lambda\tau}\right)} \end{aligned}$$

$$= \frac{4\pi\left(8\pi\lambda\tau\right)^{3/2}}{\left(4\pi\lambda\tau\right)^{3}} r''^{2} \frac{\exp\left(-\frac{(r-r'')^2}{4\lambda\tau}\right)\exp\left(-\frac{(r''-r')^2}{4\lambda\tau}\right)}{\exp\left(-\frac{(r-r')^2}{8\lambda\tau}\right)} \frac{m_l\left(\frac{rr''}{2\lambda\tau}\right) m_l\left(\frac{r''r'}{2\lambda\tau}\right)}{m_l\left(\frac{rr'}{4\lambda\tau}\right)}$$

$$= \sqrt{\frac{2}{\pi}}\left(\lambda\tau\right)^{-3/2} r''^{2} \frac{\exp\left(-\frac{(r-r'')^2}{4\lambda\tau}\right)\exp\left(-\frac{(r''-r')^2}{4\lambda\tau}\right)}{\exp\left(-\frac{(r-r')^2}{8\lambda\tau}\right)} \frac{m_l\left(\frac{rr''}{2\lambda\tau}\right) m_l\left(\frac{r''r'}{2\lambda\tau}\right)}{m_l\left(\frac{rr'}{4\lambda\tau}\right)}, \tag{3.20}$$

which for convenience may be written as $I = ER$, where

$$E = \frac{\exp\left(-\frac{(r-r'')^2}{4\lambda\tau}\right)\exp\left(-\frac{(r''-r')^2}{4\lambda\tau}\right)}{\exp\left(-\frac{(r-r')^2}{8\lambda\tau}\right)} \tag{3.21}$$

and

$$R = \sqrt{\frac{2}{\pi}}\left(\lambda\tau\right)^{-3/2} r''^{2} \frac{m_l\left(\frac{rr''}{2\lambda\tau}\right) m_l\left(\frac{r''r'}{2\lambda\tau}\right)}{m_l\left(\frac{rr'}{4\lambda\tau}\right)}. \tag{3.22}$$

The exponential part E may be written in a more practical expression:

$$\begin{aligned}
E &= \frac{\exp\left(-\frac{(r-r'')^2}{4\lambda\tau}\right)\exp\left(-\frac{(r''-r')^2}{4\lambda\tau}\right)}{\exp\left(-\frac{(r-r')^2}{8\lambda\tau}\right)} \\
&= \frac{\exp\left(-\frac{r^2-2rr''+r''^2+r''^2-2r''r'+r'^2}{4\lambda\tau}\right)}{\exp\left(-\frac{(r-r')^2}{8\lambda\tau}\right)} \\
&= \frac{\exp\left(-\frac{r^2+r'^2+2r''^2-2rr''-2r''r'}{4\lambda\tau}\right)}{\exp\left(-\frac{(r-r')^2}{8\lambda\tau}\right)} \\
&= \frac{\exp\left(-\frac{r^2+r'^2+2r''^2-2r''(r+r')}{4\lambda\tau}\right)}{\exp\left(-\frac{(r-r')^2}{8\lambda\tau}\right)} \\
&= \frac{\exp\left(-\frac{r^2+r'^2+2\left[r''^2-r''(r+r')+\frac{1}{4}(r+r')^2\right]-\frac{1}{2}(r+r')^2}{4\lambda\tau}\right)}{\exp\left(-\frac{(r-r')^2}{8\lambda\tau}\right)} \\
&= \frac{\exp\left(-\frac{r^2+r'^2-\frac{1}{2}(r+r')^2+2\left[r''-\frac{r+r'}{2}\right]^2}{4\lambda\tau}\right)}{\exp\left(-\frac{(r-r')^2}{8\lambda\tau}\right)}
\end{aligned}$$

$$= \frac{\exp\left(-\frac{\frac{1}{2}(r-r')^2+2\left[r''-\frac{r+r'}{2}\right]^2}{4\lambda\tau}\right)}{\exp\left(-\frac{(r-r')^2}{8\lambda\tau}\right)}$$
$$= \exp\left(-\frac{\left[r''-\frac{r+r'}{2}\right]^2}{2\lambda\tau}\right). \tag{3.23}$$

Change of variable

Defining $\bar{x} = (r+r')/2$ and $s = r'' - \bar{x}$, we have

$$I(r,r',s;\tau)$$
$$= \sqrt{\frac{2}{\pi}}\,(\lambda\tau)^{-3/2}\,(\bar{x}+s)^2 \frac{m_l\left(\frac{r(\bar{x}+s)}{2\lambda\tau}\right) m_l\left(\frac{(\bar{x}+s)r'}{2\lambda\tau}\right)}{m_l\left(\frac{rr'}{4\lambda\tau}\right)} \exp\left(-\frac{s^2}{2\lambda\tau}\right). \tag{3.24}$$

This corresponds to a change of variable $r'' \to s + \bar{x}$. Thus, the differential changes as $\mathrm{d}r'' \to \mathrm{d}s$ and the new integration limits are from $-\bar{x}$ to ∞:

$$u_l(r,r';2\tau) = -\ln\left[\int_{-\bar{x}}^{\infty} \mathrm{d}s\; I(r,r',s;\tau) e^{-u_l(r,\bar{x}+s;\tau)-u_l(\bar{x}+s,r';\tau)}\right]. \tag{3.25}$$

Thus, now the "squaring" procedure incorporates the recursive use of the equation above.

In practice, the potential u_l is tabulated on a finite range, up to r_{end} and r'_{end}. The free particle part $I(r,r',s;\tau)$ is a gaussian-like function, and thus, falls to zero rapidly. Therefore, integration to infinity is not required for high accuracy. However, the process still involves integration outside the tabulated values. This can be dealt with by approximating the potential outside the grid, for example $r' > r'_{\text{end}}$, as

$$u_l(r,r';\tau) \approx u_l^{\text{app}}(r,r';\tau)\frac{u_l(r,r'_{\text{end}};\tau)}{u_l^{\text{app}}(r,r'_{\text{end}};\tau)}, \tag{3.26}$$

where app refers to some approximate potential action, e.g. the primitive approximation.

In the next section, we shall consider the squaring process for the β-derivative. There one also tabulates the values, and for the integration outside the grid a proper choice is given by the β-derivative of Eq. (3.26), i.e.

$$\frac{\partial u_l(r,r';\tau)}{\partial\tau} \approx \frac{u_l(r,r'_{\text{end}};\tau)}{u_l^{\text{app}}(r,r'_{\text{end}};\tau)}\frac{\partial u_l^{\text{app}}(r,r';\tau)}{\partial\tau} + \frac{u_l^{\text{app}}(r,r';\tau)}{u_l^{\text{app}}(r,r'_{\text{end}};\tau)}\frac{\partial u_l(r,r'_{\text{end}};\tau)}{\partial\tau}$$
$$- u_l^{\text{app}}(r,r';\tau)\frac{u_l(r,r'_{\text{end}};\tau)}{[u_l^{\text{app}}(r,r'_{\text{end}};\tau)]^2}\frac{\partial u_l^{\text{app}}(r,r'_{\text{end}};\tau)}{\partial\tau}. \tag{3.27}$$

3.3.3 Evaluation of energy

The accurate use of the thermal energy estimator requires that the β-derivative of the (potential) action is also evaluated. An expression for this can be obtained by the squaring procedure as well — this will be established shortly.

The β-derivative of the density matrix of relative motion is

$$\frac{\partial}{\partial\beta}\,\rho_{\mathrm{rel}}(\boldsymbol{r},\boldsymbol{r}';\beta) = \frac{1}{4\pi r r'}\sum_{l=0}^{\infty}(2l+1)\frac{\partial\rho_l(r,r';\beta)}{\partial\beta}P_l(\cos(\theta)). \tag{3.28}$$

Therefore, we need to solve the β-derivative of the partial density matrices. Furthermore, since the free particle part is analytically known the β-derivative of the potential is required, only.

Squaring the β-derivative

Again we begin with the product property

$$\rho_l(r,r';\beta) = \int_0^\infty \mathrm{d}r''\rho_l(r,r'';\tau)\rho_l(r'',r';\tau).$$

Note that here we have $\beta = 2\tau$. Now we are interested in the β-derivative.

$$\begin{aligned}
&\frac{\partial}{\partial\beta}\rho_l(r,r';\beta)\\
&= \frac{\partial}{\partial(2\tau)}\rho_l(r,r';2\tau)\\
&= \frac{1}{2}\frac{\partial}{\partial\tau}\rho_l(r,r';2\tau)\\
&= \frac{1}{2}\frac{\partial}{\partial\tau}\int_0^\infty \mathrm{d}r''\rho_l(r,r'';\tau)\rho_l(r'',r';\tau)\\
&= \frac{1}{2}\int_0^\infty \mathrm{d}r''\left[\frac{\partial\rho_l(r,r'';\tau)}{\partial\tau}\rho_l(r'',r';\tau) + \rho_l(r,r'';\tau)\frac{\partial\rho_l(r'',r';\tau)}{\partial\tau}\right]
\end{aligned} \tag{3.29}$$

The τ-derivative of the partial density matrix

$$\rho_l(r,r';\tau) = \rho_l^{\mathrm{K}}(r,r';\tau)\exp(-u_l(r,r';\tau)) \tag{3.30}$$

is

$$\frac{\partial\rho_l(r,r';\tau)}{\partial\tau} = e^{-u_l(r,r';\tau)}\frac{\partial\rho_l^{\mathrm{K}}(r,r';\tau)}{\partial\tau} - \rho_l(r,r';\tau)\frac{\partial u_l(r,r';\tau)}{\partial\tau}, \tag{3.31}$$

from which we can solve the τ-derivative of the potential to be

$$\begin{aligned}
&\frac{\partial u_l(r,r';\tau)}{\partial\tau} \\
&= \frac{1}{\rho_l(r,r';\tau)}\left[e^{-u_l(r,r';\tau)}\frac{\partial\rho_l^{\mathrm{K}}(r,r';\tau)}{\partial\tau} - \frac{\partial\rho_l(r,r';\tau)}{\partial\tau}\right] \\
&= -e^{u_l(r,r';\tau)}\left[\frac{1}{\rho_l^{\mathrm{K}}(r,r';\tau)}\frac{\partial\rho_l(r,r';\tau)}{\partial\tau} - e^{-u_l(r,r';\tau)}\frac{1}{\rho_l^{\mathrm{K}}(r,r';\tau)}\frac{\partial\rho_l^{\mathrm{K}}(r,r';\tau)}{\partial\tau}\right] \\
&= -e^{u_l(r,r';\tau)}\left[\frac{1}{\rho_l^{\mathrm{K}}(r,r';\tau)}\frac{\partial\rho_l(r,r';\tau)}{\partial\tau} - e^{-u_l(r,r';\tau)}C_l(r,r';\tau)\right] \\
&= -e^{u_l(r,r';\tau)}\alpha_l(r,r';\tau).
\end{aligned} \tag{3.32}$$

There we defined two new terms

$$C_l(r,r';\tau) = \frac{1}{\rho_l^{\mathrm{K}}(r,r';\tau)}\frac{\partial\rho_l^{\mathrm{K}}(r,r';\tau)}{\partial\tau} \tag{3.33}$$

and

$$\alpha_l(r,r';\tau) = \frac{1}{\rho_l^{\mathrm{K}}(r,r';\tau)}\frac{\partial\rho_l(r,r';\tau)}{\partial\tau} - e^{-u_l(r,r';\tau)}C_l(r,r';\tau), \tag{3.34}$$

which are helpful for more readable results due to shorter notation.

Now, the β-derivative can be written as

$$\begin{aligned}
&\frac{\partial}{\partial\beta}\rho_l(r,r';\beta) \\
&= \frac{1}{2}\int_0^\infty \mathrm{d}r''\rho_l^{\mathrm{K}}(r,r'';\tau)\rho_l^{\mathrm{K}}(r'',r';\tau)e^{-u_l(r,r'';\tau)-u_l(r'',r';\tau)} \\
&\qquad\left[C_l(r,r'';\tau) + C_l(r'',r';\tau) - \frac{\partial u_l(r,r'';\tau)}{\partial\tau} - \frac{\partial u_l(r'',r';\tau)}{\partial\tau}\right].
\end{aligned} \tag{3.35}$$

Thus, the α term is

$$\begin{aligned}
&\alpha_l(r,r';\beta) \\
&= \frac{1}{2}\int_0^\infty \mathrm{d}r'' I(r,r',r'';\tau)e^{-u_l(r,r'';\tau)-u_l(r'',r';\tau)} \\
&\qquad\left[C_l(r,r'';\tau) + C_l(r'',r';\tau) - 2C_l(r,r';\beta) - \frac{\partial u_l(r,r'';\tau)}{\partial\tau} - \frac{\partial u_l(r'',r';\tau)}{\partial\tau}\right],
\end{aligned} \tag{3.36}$$

and the β-derivative of the potential is

$$\frac{\partial u_l(r,r';\beta)}{\partial\beta} = -e^{u_l(r,r';\beta)}\alpha_l(r,r';\beta). \tag{3.37}$$

Thus, with some high temperature initial values for the potential action and its β-derivative one can solve the derivatives at lower temperatures recursively.

The new term $C_l(r, r'; \tau)$ is easily evaluated analytically. First, according to Eq. (3.19) we have

$$\rho_l^{\mathrm{K}}(r, r'; \tau) = \frac{4\pi r r'}{(4\pi\lambda\tau)^{3/2}} \exp\left(-\frac{(r-r')^2}{4\lambda\tau}\right) m_l\left(\frac{rr'}{2\lambda\tau}\right).$$

Therefore, for the τ-derivative we get

$$\begin{aligned}\frac{\partial \rho_l^{\mathrm{K}}(r, r'; \tau)}{\partial \tau} =& \frac{4\pi r r'}{(4\pi\lambda\tau)^{3/2}} \exp\left(-\frac{(r-r')^2}{4\lambda\tau}\right) \\ & \frac{1}{\tau}\left\{\left[\frac{r^2+r'^2}{4\lambda\tau} - \frac{3}{2}\right] m_l\left(\frac{rr'}{2\lambda\tau}\right) - \frac{rr'}{2\lambda\tau}\widetilde{m}_l'\left(\frac{rr'}{2\lambda\tau}\right)\right\}, \quad (3.38)\end{aligned}$$

where $\widetilde{m}_l'(z) = e^{-z}\frac{\mathrm{d}i_l(z)}{\mathrm{d}z}$. Combining the previous two equations we are left with

$$\begin{aligned}C_l(r, r'; \tau) &= \frac{1}{\rho_l^{\mathrm{K}}(r, r'; \tau)} \frac{\partial \rho_l^{\mathrm{K}}(r, r'; \tau)}{\partial \tau} \\ &= \frac{1}{\tau}\left[\frac{r^2+r'^2}{4\lambda\tau} - \frac{3}{2} - \frac{rr'}{2\lambda\tau}\frac{\widetilde{m}_l'\left(\frac{rr'}{2\lambda\tau}\right)}{m_l\left(\frac{rr'}{2\lambda\tau}\right)}\right]. \quad (3.39)\end{aligned}$$

For clarification, here is the algorithm for the calculation of the β-derivative:

1. use some high temperature approximation for the calculation of the potential $u_l(r, r'; \tau)$ and its τ-derivative
2. calculate $\alpha(r, r'; \beta) = \alpha(r, r'; 2\tau)$ using Eq. (3.36)
3. calculate $u_l(r, r'; \beta) = u_l(r, r'; 2\tau)$ using Eq. (3.25)
4. calculate the β-derivative of the potential using Eq. (3.37)
5. using the obtained potential $u_l(r, r'; \beta)$ and its β-derivative go through the steps from 2.-5. iteratively until the desired temperature is reached

3.4 The Coulomb pair potential

For a pair of particles interacting via the Coulomb potential the density matrix can be expressed in terms of the $l = 0$ partial density matrix, that is,

$$\rho_{\mathrm{rel}}(\boldsymbol{r}, \boldsymbol{r}'; \tau) = -\frac{1}{4\pi(x-y)}\Big(\frac{\partial}{\partial x} - \frac{\partial}{\partial y}\Big)\rho_0(x, y; \tau).$$

Thus, for the computation of the effective pair potential the matrix squaring needs to be performed for $l = 0$, i.e. the s-orbital contributions, only.

Using a shorter notation the above density matrix may be written as

$$\begin{aligned}
\rho_{\text{rel}} &= -\frac{1}{4\pi(x-y)}\Big(\frac{\partial}{\partial x}-\frac{\partial}{\partial y}\Big)\rho_0 \\
&= -\frac{1}{4\pi(x-y)}\Big(\frac{\partial}{\partial x}-\frac{\partial}{\partial y}\Big)\rho_0^{\text{K}} e^{-u_0} \\
&= -\frac{1}{4\pi(x-y)}\Big[e^{-u_0}\Big(\frac{\partial}{\partial x}-\frac{\partial}{\partial y}\Big)\rho_0^{\text{K}} - \rho_0^{\text{K}} e^{-u_0}\Big(\frac{\partial}{\partial x}-\frac{\partial}{\partial y}\Big)u_0\Big] \\
&= \rho_{\text{rel}}^{\text{K}} e^{-u_0} + \rho_0^{\text{K}} e^{-u_0} f \\
&= e^{-u_0}\left(\rho_{\text{rel}}^{\text{K}} + \rho_0^{\text{K}} f\right),
\end{aligned} \tag{3.40}$$

where

$$\rho_{\text{rel}}^{\text{K}} = -\frac{1}{4\pi(x-y)}\Big(\frac{\partial}{\partial x}-\frac{\partial}{\partial y}\Big)\rho_0^{\text{K}} = (4\pi\lambda\tau)^{-3/2} e^{-(x-y)^2/4\lambda\tau} \tag{3.41}$$

and

$$f = \frac{1}{4\pi(x-y)}\Big(\frac{\partial}{\partial x}-\frac{\partial}{\partial y}\Big)u_0. \tag{3.42}$$

Therefore, the pair potential, see Eq. (3.10), is

$$\begin{aligned}
u(\boldsymbol{r},\boldsymbol{r}';\tau) &= -\ln\left[\frac{\rho_{\text{rel}}(\boldsymbol{r},\boldsymbol{r}';\tau)}{\rho_{\text{rel}}^{\text{K}}(\boldsymbol{r},\boldsymbol{r}';\tau)}\right] \\
&= -\ln\left[\frac{e^{-u_0(x,y;\tau)}\left\{\rho_{\text{rel}}^{\text{K}}(x,y;\tau)+\rho_0^{\text{K}}(x,y;\tau)f(x,y;\tau)\right\}}{\rho_{\text{rel}}^{\text{K}}(x,y;\tau)}\right] \\
&= u_0(x,y;\tau) - \ln\left[1+\frac{\rho_0^{\text{K}}(x,y;\tau)}{\rho_{\text{rel}}^{\text{K}}(x,y;\tau)}f(x,y;\tau)\right] \\
&= u(x,y;\tau).
\end{aligned}$$

Furthermore, since

$$\frac{\rho_0^{\text{K}}(x,y;\tau)}{\rho_{\text{rel}}^{\text{K}}(x,y;\tau)} = \frac{\frac{4\pi xy}{(4\pi\lambda\tau)^{3/2}}\exp\left(-\frac{(x-y)^2}{4\lambda\tau}\right) m_0\left(\frac{xy}{2\lambda\tau}\right)}{(4\pi\lambda\tau)^{-3/2}\exp\left(-\frac{(x-y)^2}{4\lambda\tau}\right)} = 4\pi\, x\, y\, m_0(\frac{xy}{2\lambda\tau}),$$

the pair potential may be written as

$$u(x,y;\tau) = u_0(x,y;\tau) - \ln\left[1+4\pi\, x\, y\, m_0(\frac{xy}{2\lambda\tau})f(x,y;\tau)\right]. \tag{3.43}$$

3.4.1 β-derivative

Since the free particle part of the action is known analytically we only need to calculate the β-derivative of the potential (pair) action, i.e. Eq. (3.43). With elementary mathematics we get

$$\frac{\partial u}{\partial \beta} = \frac{\partial u_0}{\partial \beta} - 4\pi x y \frac{m_0(z)\frac{\partial f}{\partial \beta} - \frac{z}{\beta} f\left[\widetilde{m}_0'(z) - m_0(z)\right]}{1 + 4\pi x y m_0(z) f}, \tag{3.44}$$

where the new terms are defined as

$$z = \frac{xy}{2\lambda\beta}, \tag{3.45}$$

$$\widetilde{m}_0'(z) = \exp(-z)\frac{\mathrm{d}i_0(z)}{\mathrm{d}z}, \tag{3.46}$$

$$\frac{\partial f}{\partial \beta} = \frac{1}{4\pi(x-y)}\left(\frac{\partial}{\partial x} - \frac{\partial}{\partial y}\right)\frac{\partial u_0}{\partial \beta}. \tag{3.47}$$

Another approach for the β-derivative

Here the β-derivative of the pair potential is derived in a different way. This approach yields equivalent result. Let's begin with the β-derivative of the density matrix.

$$\begin{aligned} &\frac{\partial \rho_{\mathrm{rel}}}{\partial \beta} = e^{-u}\frac{\partial \rho_{\mathrm{rel}}^{\mathrm{K}}}{\partial \beta} - \rho_{\mathrm{rel}}\frac{\partial u}{\partial \beta} \\ &\implies \frac{\partial u}{\partial \beta} = \frac{1}{\rho_{\mathrm{rel}}^{\mathrm{K}}}\frac{\partial \rho_{\mathrm{rel}}^{\mathrm{K}}}{\partial \beta} - \frac{1}{\rho_{\mathrm{rel}}}\frac{\partial \rho_{\mathrm{rel}}}{\partial \beta} \end{aligned} \tag{3.48}$$

Then let us define the first term on the right-hand side to be $C_{\mathrm{rel}}^{\mathrm{K}}$, that is

$$C_{\mathrm{rel}}^{\mathrm{K}}(\boldsymbol{r}, \boldsymbol{r}'; \beta) = \frac{1}{\rho_{\mathrm{rel}}^{\mathrm{K}}(\boldsymbol{r}, \boldsymbol{r}'; \beta)}\frac{\partial \rho_{\mathrm{rel}}^{\mathrm{K}}(\boldsymbol{r}, \boldsymbol{r}'; \beta)}{\partial \beta}. \tag{3.49}$$

By Eq. (3.6) the free particle density matrix is

$$\rho_{\mathrm{rel}}^{\mathrm{K}}(\boldsymbol{r}, \boldsymbol{r}'; \beta) = (4\pi\lambda\beta)^{-3/2}\exp\left(-\frac{|\boldsymbol{r} - \boldsymbol{r}'|^2}{4\lambda\beta}\right),$$

and the β-derivative is, thus, given as

$$\frac{\partial \rho_{\mathrm{rel}}^{\mathrm{K}}(\boldsymbol{r}, \boldsymbol{r}'; \beta)}{\partial \beta} = \rho_{\mathrm{rel}}^{\mathrm{K}}(\boldsymbol{r}, \boldsymbol{r}'; \beta)\frac{1}{\beta}\left[\frac{|\boldsymbol{r} - \boldsymbol{r}'|^2}{4\lambda\beta} - \frac{3}{2}\right] \tag{3.50}$$

This leads to

$$C_{\mathrm{rel}}^{\mathrm{K}}(\boldsymbol{r}, \boldsymbol{r}'; \beta) = \frac{1}{\beta}\left[\frac{|\boldsymbol{r} - \boldsymbol{r}'|^2}{4\lambda\beta} - \frac{3}{2}\right]. \tag{3.51}$$

Now, the second term on the right-hand side of Eq. (3.48) cannot be analytically solved but it can be further simplified. Let's define that term to be

$$e^{u(\boldsymbol{r},\boldsymbol{r}';\beta)}C_{\text{rel}}(\boldsymbol{r},\boldsymbol{r}';\beta) = -\frac{1}{\rho_{\text{rel}}(\boldsymbol{r},\boldsymbol{r}';\beta)}\frac{\partial\rho_{\text{rel}}(\boldsymbol{r},\boldsymbol{r}';\beta)}{\partial\beta}, \tag{3.52}$$

which leads to

$$C_{\text{rel}}(\boldsymbol{r},\boldsymbol{r}';\beta) = -\frac{1}{\rho^{\text{K}}_{\text{rel}}(\boldsymbol{r},\boldsymbol{r}';\beta)}\frac{\partial\rho_{\text{rel}}(\boldsymbol{r},\boldsymbol{r}';\beta)}{\partial\beta}. \tag{3.53}$$

For the Coulomb potential the density matrix of relative motion can be expressed as

$$\begin{aligned}\rho_{\text{rel}}(\boldsymbol{r},\boldsymbol{r}';\beta) &= -\frac{1}{4\pi(x-y)}\Big(\frac{\partial}{\partial x}-\frac{\partial}{\partial y}\Big)\rho_0(x,y;\beta)\\ &= e^{-u_0}\left(\rho^{\text{K}}_{\text{rel}}+\rho^{\text{K}}_0 f\right),\end{aligned} \tag{3.54}$$

see Eqs. (3.40) and (3.42) for more details. The β-derivative of the expression above is

$$\begin{aligned}&\frac{\partial\rho_{\text{rel}}(\boldsymbol{r},\boldsymbol{r}';\beta)}{\partial\beta}\\ &= \frac{\partial}{\partial\beta}\left[e^{-u_0}\left(\rho^{\text{K}}_{\text{rel}}+\rho^{\text{K}}_0 f\right)\right]\\ &= -e^{-u_0}\left(\rho^{\text{K}}_{\text{rel}}+\rho^{\text{K}}_0 f\right)\frac{\partial u_0}{\partial\beta}+e^{-u_0}\left(\frac{\partial\rho^{\text{K}}_{\text{rel}}}{\partial\beta}+f\frac{\partial\rho^{\text{K}}_0}{\partial\beta}+\rho^{\text{K}}_0\frac{\partial f}{\partial\beta}\right)\end{aligned} \tag{3.55}$$

Thus, we get

$$\begin{aligned}C_{\text{rel}} &= -\frac{1}{\rho^{\text{K}}_{\text{rel}}}\frac{\partial\rho_{\text{rel}}}{\partial\beta}.\\ &= e^{-u_0}\left[\left(1+\frac{\rho^{\text{K}}_0}{\rho^{\text{K}}_{\text{rel}}}f\right)\frac{\partial u_0}{\partial\beta}-\frac{1}{\rho^{\text{K}}_{\text{rel}}}\frac{\partial\rho^{\text{K}}_{\text{rel}}}{\partial\beta}-\frac{1}{\rho^{\text{K}}_{\text{rel}}}\frac{\partial\rho^{\text{K}}_0}{\partial\beta}f-\frac{\rho^{\text{K}}_0}{\rho^{\text{K}}_{\text{rel}}}\frac{\partial f}{\partial\beta}\right]\\ &= e^{-u_0}\left[\left(1+\frac{\rho^{\text{K}}_0}{\rho^{\text{K}}_{\text{rel}}}f\right)\frac{\partial u_0}{\partial\beta}-C^{\text{K}}_{\text{rel}}-\frac{\rho^{\text{K}}_0}{\rho^{\text{K}}_{\text{rel}}}fC_0-\frac{\rho^{\text{K}}_0}{\rho^{\text{K}}_{\text{rel}}}\frac{\partial f}{\partial\beta}\right],\end{aligned} \tag{3.56}$$

where

$$\frac{\rho^{\text{K}}_0(x,y;\tau)}{\rho^{\text{K}}_{\text{rel}}(x,y;\tau)} = 4\pi\,x\,y\,m_0(\frac{xy}{2\lambda\tau}).$$

Finally, Eq. (3.48) may be written as

$$\frac{\partial u(x,y;\beta)}{\partial\beta} = C^{\text{K}}_{\text{rel}}(x,y;\beta)+e^{u(x,y;\beta)}C_{\text{rel}}(x,y;\beta). \tag{3.57}$$

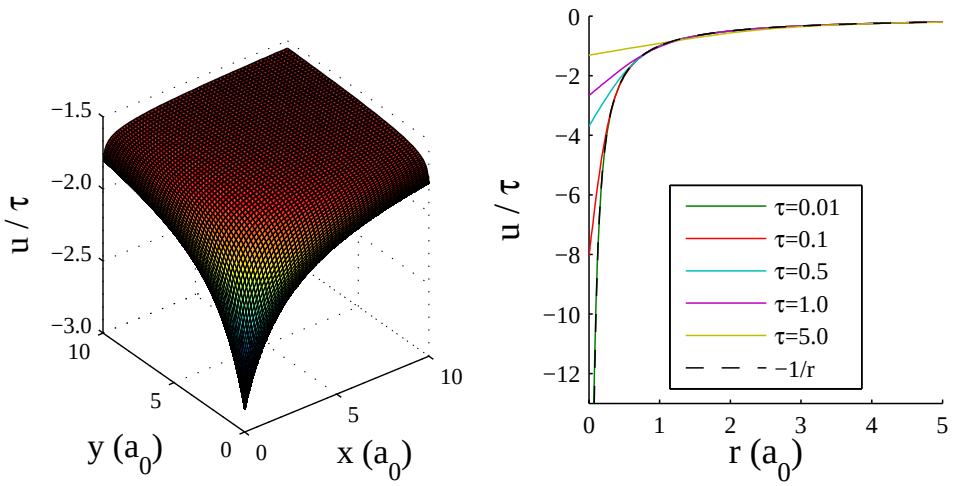

Figure 3.1: Pair potential for the electron–proton interaction divided by the time step τ. (LEFT) Surface for $\tau = 1.0E_h^{-1}$. (RIGHT) Diagonal for different time steps. The $-1/r$ potential is given as a reference.

3.4.2 Pair potential and the β-derivative

Here is the set of equations needed for the computation of the pair action of the Coulomb potential. First, one must generate the $l = 0$ potential and its β-derivative, for example, by using the matrix squaring technique described earlier. After that the pair potential is given by

$$u(x, y; \beta) = u_0(x, y; \beta) - \ln\left[1 + 4\pi x y m_0(z) f(x, y; \beta)\right], \tag{3.58}$$

and the β-derivative by

$$\frac{\partial u}{\partial \beta} = \frac{\partial u_0}{\partial \beta} - 4\pi x y \frac{m_0(z)\frac{\partial f}{\partial \beta} - \frac{z}{\beta} f\left[\widetilde{m}_0'(z) - m_0(z)\right]}{1 + 4\pi x y m_0(z) f}, \tag{3.59}$$

where

$$x = (r + r' + |\boldsymbol{r} - \boldsymbol{r}'|)/2, \tag{3.60}$$
$$y = (r + r' - |\boldsymbol{r} - \boldsymbol{r}'|)/2, \tag{3.61}$$

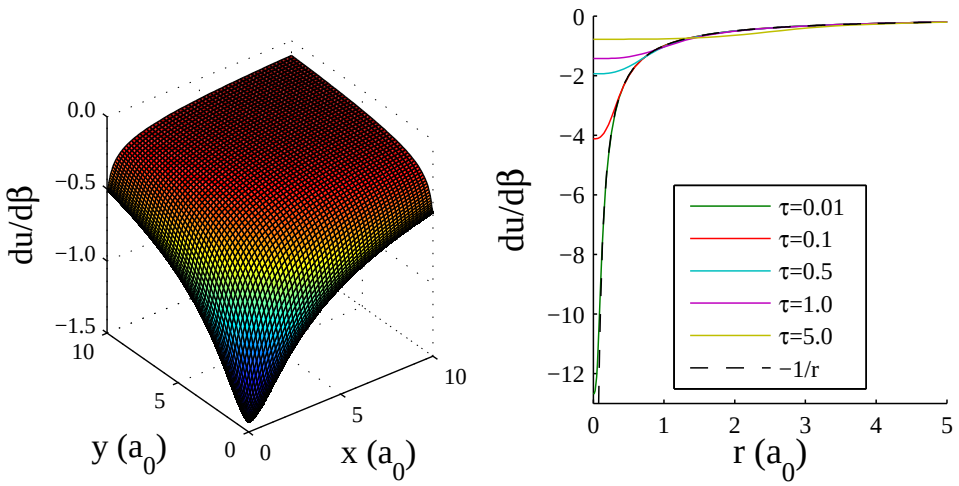

Figure 3.2: β-derivative of the electron–proton pair potential. (LEFT) Surface for $\tau = 1.0E_h^{-1}$. (RIGHT) Diagonal for different time steps. The $-1/r$ potential is given as a reference. With $\tau = 0.01E_h^{-1}$ the existing difference can be seen close to origin.

$$z = \frac{xy}{2\lambda\beta}, \tag{3.62}$$

$$m_0(z) = \exp(-z) i_0(z), \tag{3.63}$$

$$\widetilde{m}_0'(z) = \exp(-z) \frac{\mathrm{d}i_0(z)}{\mathrm{d}z}, \tag{3.64}$$

$$f(x,y;\beta) = \frac{1}{4\pi(x-y)} \left(\frac{\partial}{\partial x} - \frac{\partial}{\partial y} \right) u_0(x,y;\beta), \tag{3.65}$$

$$\frac{\partial f(x,y;\beta)}{\partial \beta} = \frac{1}{4\pi(x-y)} \left(\frac{\partial}{\partial x} - \frac{\partial}{\partial y} \right) \frac{\partial u_0(x,y;\beta)}{\partial \beta}. \tag{3.66}$$

In Figs. 3.1 and 3.2 the effective Coulomb pair potential and its β-derivative are shown for the electron–proton interaction.

3.4.3 Periodic pair potential

In order to shorten the notation here we omit the text ”rel” refering to the density matrix of relative motion. An expression for a periodic pair potential may be derived by a sum over periodic images [Ceperley, 1983] as

$$
\begin{aligned}
& \rho_{\mathrm{PBC}}(\boldsymbol{r},\boldsymbol{r}';\beta) = \sum_{\boldsymbol{n},\boldsymbol{m}} \rho(\boldsymbol{r}+\boldsymbol{n}L,\boldsymbol{r}'+\boldsymbol{m}L;\beta) \\
\iff \quad & \rho^{\mathrm{K}}_{\mathrm{PBC}} e^{-u_{\mathrm{PBC}}} = \sum_{\boldsymbol{n},\boldsymbol{m}} \rho^{\mathrm{K}}_{\boldsymbol{n},\boldsymbol{m}} e^{-u_{\boldsymbol{n},\boldsymbol{m}}} \\
\implies & u_{\mathrm{PBC}} = -\ln\left[\frac{\sum_{\boldsymbol{n},\boldsymbol{m}} \rho^{\mathrm{K}}_{\boldsymbol{n},\boldsymbol{m}} e^{-u_{\boldsymbol{n},\boldsymbol{m}}}}{\rho^{\mathrm{K}}_{\mathrm{PBC}}}\right] \\
& = -\ln\left[\frac{\sum_{\boldsymbol{n},\boldsymbol{m}} \rho^{\mathrm{K}}_{\boldsymbol{n},\boldsymbol{m}} e^{-u_{\boldsymbol{n},\boldsymbol{m}}}}{\sum_{\boldsymbol{k}} \rho^{\mathrm{K}}_{\boldsymbol{k}}}\right].
\end{aligned} \tag{3.67}
$$

Thus, the periodic pair potential is given as a free particle weighted average of the infinite one according to the equation above. As in chapter two L is the set of three primitive vectors of the Bravais lattice of the periodic system and $\boldsymbol{n}$ is an integer vector. For large simulation boxes u_{PBC} approaches u, and thus, the weighting process can be neglected. For small u the expression above simplifies to a similar form as is given in Ceperley [1983], i.e.

$$
u_{\mathrm{PBC}} = \frac{\sum_{\boldsymbol{n},\boldsymbol{m}} \rho^{\mathrm{K}}_{\boldsymbol{n},\boldsymbol{m}} u_{\boldsymbol{n},\boldsymbol{m}}}{\sum_{\boldsymbol{k}} \rho^{\mathrm{K}}_{\boldsymbol{k}}}. \tag{3.68}
$$

Chapter 4

Fermion and boson statistics

4.1 Fermion and boson density matrices

For indistinguishable particles the state of the system is either antisymmetric (fermions, F) or symmetric (bosons, B), for which the density matrix may be written as a sum over particle permutations, $\mathcal{P}$, as [Feynman and Hibbs, 1965, Feynman, 1972, 1998, Lyubartsev and Vorontsov-Velyaminov, 1993, Ceperley, 1996, Kleinert, 2004]

$$\rho_{\mathrm{F/B}}(R, R'; \beta) = \frac{1}{N!} \sum_{\mathcal{P}} (\mp 1)^{\mathcal{P}} \rho(\mathcal{P}R, R'; \beta), \tag{4.1}$$

where $\mathcal{P}$ is the permutation of particle labels, and $-$ and $+$ are for fermions and bosons, respectively. The above is simply a projection of the distinguishable particle, i.e. boltzmannon, density matrix ρ into either antisymmetric $(-)$ or symmetric $(+)$ states, only.

For fermions Eq. (4.1) results in the well-known *fermion sign problem*, in practice, due to the alternating sign, which leads to cancellation of positive and negative permutations. The direct use of Eq. (4.1), while exact, becomes exceedingly inefficient as the inverse temperature β and the number of particles N increase [Ceperley, 1996].

There are ways to go around the sign problem, such as restricted path integral [Ceperley, 1996] and multilevel blocking [Mak et al., 1998, Egger et al., 2000] methods, for example. Unfortunately, however, none of the present finite temperature solutions is feasible for accurate fermionic calculations at low temperatures, yet.

Next, we shall only briefly consider the restricted path integral approach, for which Ceperley [1996] proved that it is sufficient to sample only the positive or the negative contributions of the density matrix. Thus, the cancellation of the negative

and positive permutations is removed and the fermion sign-problem is solved, in principle.

4.1.1 Restricted path integral and fermion nodes

The basic idea behind the restricted path integrals [Ceperley, 1996] is exactly the same as that of the fixed-node approach [Anderson, 1976] for the ground state simulations, i.e. sampling only the positive or the negative contributions of the density matrix — or a wave function in case of the ground state. Therefore, in the restricted path integrals a trial density matrix is needed to define the positive and negative regions.

Starting from Eq. (4.1) we can write the many body fermion density matrix as

$$\begin{aligned}
\rho_{\mathrm{F}}(R,R';\beta) &= \frac{1}{N!}\sum_{\mathcal{P}}(-1)^{\mathcal{P}}\rho(\mathcal{P}R,R';\beta) \\
&= \frac{1}{N!}\sum_{\mathcal{P}}(-1)^{\mathcal{P}}\rho^{\mathrm{K}}(\mathcal{P}R,R';\beta)e^{-U(\mathcal{P}R,R';\beta)} \\
&= \frac{1}{N!}\sum_{\mathcal{P}}(-1)^{\mathcal{P}}\rho^{\mathrm{K}_{\mathcal{P}}}e^{-U_{\mathcal{P}}} \\
&= \rho^{\mathrm{K}_0}e^{-U_0}\frac{1}{N!}\sum_{\mathcal{P}}(-1)^{\mathcal{P}}\frac{\rho^{\mathrm{K}_{\mathcal{P}}}}{\rho^{\mathrm{K}_0}}e^{-(U_{\mathcal{P}}-U_0)} \\
&= \underbrace{\rho^{\mathrm{K}_0}e^{-U_0}}_{\text{boltzmannons}}\, w_{\mathrm{ex}},
\end{aligned} \tag{4.2}$$

where the term w_{ex} indicates how the Boltzmann statistics should be weighted in case of fermions. In the restricted path integral scheme only paths for which $w_{\mathrm{ex}} > 0$, for example, are accepted.

For the ground state the so-called *fermion nodes* are located at the space coordinates where the wave function vanishes, that is, where $\psi(R) = 0$. For the density matrix [Ceperley, 1991, 1996] the nodes are defined for a continuous path R_t as

$$\rho_{\mathrm{F}}(R_t,R_*;t) = 0, \quad \text{for all} \quad 0 < t \leq \beta, \tag{4.3}$$

where R_* is called the *reference point*, which is held fixed. In terms of the exchange term w_{ex} the nodes are given as

$$w_{\mathrm{ex}}(R_t,R_*;t) = 0, \quad \text{for all} \quad 0 < t \leq \beta. \tag{4.4}$$

For more details on the restricted path integrals and the fermion nodes see Ceperley [1991, 1996].

Free particle nodes

In case of the primitive approximation or a constant potential action the difference $U_{\mathcal{P}} - U_0 = 0$ in Eq. (4.2), and thus, we end up with

$$w_{\text{ex}} = \frac{1}{N!}\sum_{\mathcal{P}}(-1)^{\mathcal{P}}\frac{\rho^{\text{K}}(\mathcal{P}R,R';\beta)}{\rho^{\text{K}}(R,R';\beta)} \equiv w_{\text{ex}}^{\text{FP}}, \tag{4.5}$$

which determines the so-called *free particle nodes* (FP) according to Eqs. (4.3) and (4.4). This can be calculated exactly for any number of particles since the free particle density matrix is known analytically.

In a more computationally tractable form Eq. (4.5) may be written in terms of a determinant [Ceperley, 1991, 1996], which for N indistinguishable particles, i.e. $R = \{\mathbf{r}_1, \mathbf{r}_2, \ldots, \mathbf{r}_N\}$, is

$$w_{\text{ex}}^{\text{FP}} = \frac{1}{N!}\frac{\det(X)}{\rho^{\text{K}}(R,R';\beta)}, \tag{4.6}$$

where

$$X = \begin{bmatrix} \rho^{\text{K}}(\mathbf{r}_1,\mathbf{r}'_1;\beta) & \rho^{\text{K}}(\mathbf{r}_2,\mathbf{r}'_1;\beta) & \ldots & \rho^{\text{K}}(\mathbf{r}_N,\mathbf{r}'_1;\beta) \\ \rho^{\text{K}}(\mathbf{r}_1,\mathbf{r}'_2;\beta) & \rho^{\text{K}}(\mathbf{r}_2,\mathbf{r}'_2;\beta) & \ldots & \rho^{\text{K}}(\mathbf{r}_N,\mathbf{r}'_2;\beta) \\ \vdots & \vdots & \ddots & \vdots \\ \rho^{\text{K}}(\mathbf{r}_1,\mathbf{r}'_N;\beta) & \rho^{\text{K}}(\mathbf{r}_2,\mathbf{r}'_N;\beta) & \ldots & \rho^{\text{K}}(\mathbf{r}_N,\mathbf{r}'_N;\beta) \end{bmatrix}. \tag{4.7}$$

Above one should notice that the elements of the matrix X are free particle density matrices of a single particle. For bolzmannon particles the off-diagonal elements vanish, and as known, the many-body density matrix of free distinguishable particles is just a product of the single particle density matrices.

As an example, let us consider a more general system consisting of N_1 electrons spin up ($\uparrow$), N_2 electrons spin down ($\downarrow$), N_3 nuclei spin up ($\uparrow$) and N_4 nuclei spin down ($\downarrow$), i.e.

$$\begin{aligned} R = \{&\mathbf{r}_1^{(\uparrow)}, \mathbf{r}_2^{(\uparrow)}, \ldots, \mathbf{r}_{N_1}^{(\uparrow)}, \mathbf{r}_1^{(\downarrow)}, \mathbf{r}_2^{(\downarrow)}, \ldots, \mathbf{r}_{N_2}^{(\downarrow)}, \\ &\mathbf{R}_1^{(\uparrow)}, \mathbf{R}_2^{(\uparrow)}, \ldots, \mathbf{R}_{N_3}^{(\uparrow)}, \mathbf{R}_1^{(\downarrow)}, \mathbf{R}_2^{(\downarrow)}, \ldots, \mathbf{R}_{N_4}^{(\downarrow)}\}. \end{aligned} \tag{4.8}$$

Now, the free particle nodes can be determined from

$$w_{\text{ex}}^{\text{FP}} = \frac{1}{N_1!}\frac{1}{N_2!}\frac{1}{N_3!}\frac{1}{N_4!}\frac{\det(X_1)\det(X_2)\det(X_3)\det(X_4)}{\rho^{\text{K}}(R,R';\beta)}, \tag{4.9}$$

where matrix X_i is constructed from particles N_i in a similar fashion as is shown in Eq. (4.7).

4.1.2 Fermion path

For fermions the path can be expressed in two ways [Ceperley, 1996, Lyubartsev, 2005]. We can expand the distinguishable particle density matrix in Eq. (4.1) as

$$\begin{aligned}
&\rho_{\mathrm{F}}(R,R';\beta)\\
&=\frac{1}{N!}\sum_{\mathcal{P}}(-1)^{\mathcal{P}}\rho(\mathcal{P}R,R';\beta)\\
&=\frac{1}{N!}\sum_{\mathcal{P}}(-1)^{\mathcal{P}}\int \mathrm{d}R_1\mathrm{d}R_2\cdots\mathrm{d}R_M\;\rho(\mathcal{P}R,R_1;\tau)\rho(R_1,R_2;\tau)\cdots\rho(R_M,R';\tau)\\
&=\int \mathrm{d}R_1\mathrm{d}R_2\cdots\mathrm{d}R_M\;\frac{1}{N!}\sum_{\mathcal{P}}(-1)^{\mathcal{P}}\rho(\mathcal{P}R,R_1;\tau)\rho(R_1,R_2;\tau)\cdots\rho(R_M,R';\tau)\\
&=\int \mathrm{d}R_1\mathrm{d}R_2\cdots\mathrm{d}R_M\;\rho_{\mathrm{F}}(R,R_1;\tau)\rho(R_1,R_2;\tau)\cdots\rho(R_M,R';\tau). \qquad (4.10)
\end{aligned}$$

On the other hand, the fermion density matrix may also be written as an expansion of the fermion density matrices leading to

$$\begin{aligned}
&\rho_{\mathrm{F}}(R,R';\beta)\\
&=\int \mathrm{d}R_1\mathrm{d}R_2\cdots\mathrm{d}R_M\;\rho_{\mathrm{F}}(R,R_1;\tau)\rho_{\mathrm{F}}(R_1,R_2;\tau)\cdots\rho_{\mathrm{F}}(R_M,R';\tau). \qquad (4.11)
\end{aligned}$$

Both expression above are exact, but for most systems the straightforward application of either one is inefficient. An accurate approximation for the high temperature, i.e. small τ, fermion density matrix present in the above equations would be that given by the primitive approximation, i.e.

$$\begin{aligned}
\rho_{\mathrm{F}}(R,R';\tau)&\approx\rho_{\mathrm{F}}^{\mathrm{K}}(R,R';\tau)e^{-U(R,R';\tau)}\\
&=\rho^{\mathrm{K}}(R,R';\tau)e^{-U(R,R';\tau)}w_{\mathrm{ex}}^{\mathrm{FP}}(R,R';\tau)\\
&=\rho(R,R';\tau)w_{\mathrm{ex}}^{\mathrm{FP}}(R,R';\tau). \qquad (4.12)
\end{aligned}$$

Next we shall consider path integral simulations using Eqs. (4.11) and (4.12), where the path is restricted from first-principles.

Restricting the path

For efficient Monte Carlo simulations for fermions it seems essential that the path is somehow restricted, for instance, to the positive region, only. If the density matrix, or a decent approximation, is already known one can use that for locating the nodes [Ceperley, 1996]. On the other hand, one can also try locating the nodes from first-principles during the simulation using Eqs. (4.11) and (4.12). Next, we test the latter

case through a simple procedure, which here is based on the multilevel algorithm with the bisection moves — results are shown below, also.

As long as τ is small enough Eq. (4.12) is accurate, and with the bisection moves the kinetic part of the action is sampled exactly. Thus, in principle, we only need to deal with the term

$$w_{\text{ex}}^{\text{FP}}(R, R'; \tau) e^{-U(R,R';\tau)}. \tag{4.13}$$

Now, if the level L is 3 for the multilevel algorithm we have

$$\underbrace{\left(\left| \frac{g_{4\tau}^{i+1}}{g_{4\tau}^{i}} \right| e^{-\Delta U_{4\tau}} \right)}_{1^{\text{st}}\text{ stage}} \underbrace{\left(\left| \frac{g_{2\tau}^{i+1}}{g_{2\tau}^{i}} \right| e^{-\Delta U_{2\tau}} \left| \frac{g_{4\tau}^{i}}{g_{4\tau}^{i+1}} \right| e^{\Delta U_{4\tau}} \right)}_{2^{\text{nd}}\text{ stage}} \underbrace{\left(\left| \frac{g_{\tau}^{i+1}}{g_{\tau}^{i}} \right| e^{-\Delta U_{\tau}} \left| \frac{g_{2\tau}^{i}}{g_{2\tau}^{i+1}} \right| e^{\Delta U_{2\tau}} \right)}_{3^{\text{rd}}\text{ stage}}, \tag{4.14}$$

where the coefficients g_{τ}^{i} equal the product of the free particle weights of that stage, e.g.

$$g_{4\tau}^{i} = w_{\text{ex}}^{\text{Free}}(R_m^i, R_{m+4}^i; 4\tau) w_{\text{ex}}^{\text{Free}}(R_{m+4}^i, R_{m+8}^i; 4\tau), \tag{4.15}$$

for the i^{th} Monte Carlo iteration. The restriction to the positive region is determined by the coefficients $g_{n\tau}^{i+1}$ as

- 1^{st} stage: if $g_{4\tau}^{i+1} < 0$ reject, otherwise go through the Metropolis scheme for that stage according to Eq. (4.14)
  - if accepted continue to the second stage
- 2^{nd} stage: if $g_{2\tau}^{i+1} < 0$ reject, otherwise go through the Metropolis scheme for that stage according to Eq. (4.14)
  - if accepted continue to the third stage
- 3^{rd} stage: if $g_{\tau}^{i+1} < 0$ reject, otherwise go through the Metropolis scheme for that stage according to Eq. (4.14)
  - if accepted then save the new configuration, otherwise hold on to the old one

This approach is close to exact as long as the $n\tau$ of the largest level is small enough.

Unfortunately, as can be seen from the total energy results for He triplet, Li and Be, see Table 4.1, the approach is dependent on the sampling procedure. Increasing the level L will also increase the energy expectation value, and at some point the

Table 4.1: Total energies for small test systems calculated using the procedure introduced in the Restricting the path section: He triplet, Li and Be with $\tau = 0.03E_h^{-1}$ and $M = 2^{16}$, i.e. $T \approx 160$ K. Energies are given in units of hartree, L is the largest level in the multilevel algorithm and P_{acc} refers to the total acceptance probability.

	L	5	6	7	8
He	P_{acc}	0.66	0.50	0.37	0.29
($S = 1$)	E	$-2.224(2)$	$-2.1579(8)$ [a]	$-2.131(6)$	$-2.12(2)$
	L	4	5	6	7
Li	P_{acc}	0.64	0.45	0.31	0.23
	E	$-7.586(5)$	$-7.472(3)$ [b]	$-7.437(5)$	$-7.44(2)$
	L		5	6	
Be	P_{acc}		0.29	0.16	
	E		$-14.767(14)$	$-14.70(3)$ [c]	

[a] exact value for He ($S = 1$) is -2.1752 [Bürgers et al., 1995]

[b] exact value for Li is -7.4781 [McKenzie and Drake, 1991]

[c] exact value for Be is -14.6674 [Stanke et al., 2007]

restriction becomes poor due to the approximation in Eq. (4.12). However, Table 4.1 and related data indicate that good fermion nodes lie between some levels. The match could be made better by varying the size of the time step, however, this is not desirable.

In Table 4.2 we compare the total energies with different choices of nodes for the same atoms: He triplet, Li and Be. Here the nodes of the approach discussed above are called "Level nodes". The comparisons are made to results from PIMC simulations with the free particle (FP) nodes and the Hartree–Fock (HF) nodes. In addition, accurate upper bound values from literature are given. For these atoms the HF nodes are located at $|\boldsymbol{r}_1| = |\boldsymbol{r}_2|$, where $\boldsymbol{r}_1$ and $\boldsymbol{r}_2$ are coordinates for the electrons with the same spin. As expected, the HF nodes give accurate energies.

In Fig. 4.1 there are also snapshots of LiH and e^+Li molecules, which are simulated using the free particle nodes at about 160 K with time step $\tau = 0.03E_h^{-1}$. The LiH molecule is simulated fully nonadiabatically, whereas in the e^+Li simulation the Li nucleus has infinite mass. In the caption also the energetics are given and compared to accurate values. The free particle nodes give accurate expectation values for the e^+Li molecule — the same is not true for a single Li atom or the LiH molecule. The unexpected accuracy is due to the strong delocalization of the positron affecting the electronic structure of the Li atom, see the right figure in Fig. 4.1.

Table 4.2: Total energies for He triplet, Li and Be calculated using the free particle (FP) and the Hartree–Fock (HF) nodes with $\tau = 0.03E_h^{-1}$ and $M = 2^{16}$, i.e. $T \approx 160$ K. Also, the best matches from Table 4.1 and accurate reference energies with needed decimals are given. Energies are given in units of hartree.

	FP nodes	"Level nodes"	HF nodes	exact
He ($S = 1$)	$-2.116(2)$	$-2.1579(8)$	$-2.1757(9)$	-2.1752 [a]
Li	$-7.400(6)$	$-7.472(3)$	$-7.4715(30)$	-7.4781 [b]
Be	$-14.596(12)$	$-14.70(3)$	$-14.6845(50)$	-14.6674 [c]

[a] Bürgers et al. [1995]

[b] McKenzie and Drake [1991]

[c] Stanke et al. [2007]

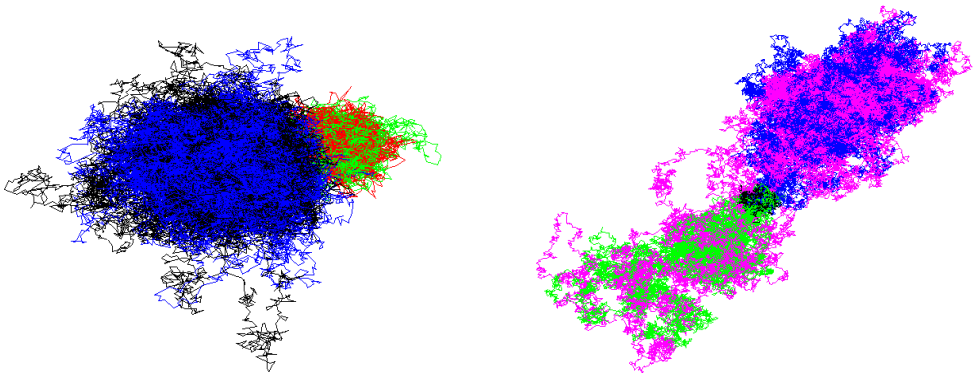

Figure 4.1: Simulation snapshots. Black, blue, red and green refer to electrons, and magenta is for the positron. Li nuclei cannot be seen in the figures. (LEFT) Fully nonadiabatic LiH molecule simulation giving total energy of $-8.0094(32)E_h$. This is not in good agreement with $-8.0661557638E_h$ by Scheu et al. [2001]. However, the binding energy of about $0.1E_h$ is relatively close to the accurate value of about $0.088E_h$. (RIGHT) e^+Li molecule with fixed Li nucleus giving total energy of $-7.5324(26)E_h$. This coincides exactly with $-7.5323955E_h$ calculated using the explicitly correlated gaussians [Mitroy, 2004].

Chapter 5

Few electron systems at finite temperature

This chapter is a brief summary to the simulations and results of the articles included in this thesis. Moreover, there will be some interesting additional parts, e.g. results that did not fit the contents of the papers — along with some theory.

5.1 Electron–nuclei coupling in H_2^+

In Paper I we evaluate the density matrix of the full three-body quantum dynamics, i.e. two protons and an electron, in a stationary state and finite temperature. This is what we call "all-quantum" (AQ) simulation. Secondly, the electronic part only is evaluated as a function of internuclear distance in the spirit of Born–Oppenheimer (BO) approximation, and thirdly, the adiabatic nuclear dynamics (QN) is evaluated in the BO potential curve. These allow us to demonstrate the nonadiabatic electron–nuclei coupling by a projection of the AQ dynamics onto the adiabatic approximations.

For the hydrogen molecule ion the potential energy is

$$V(\mathbf{r}_1, \mathbf{r}_2, \mathbf{R}) = -\frac{1}{r_1} - \frac{1}{r_2} + \frac{1}{R}, \tag{5.1}$$

where $r_i = |\mathbf{r} - \mathbf{R}_i|$, $R = |\mathbf{R}_1 - \mathbf{R}_2|$, $\mathbf{r}$ being the coordinates of the electron and R the internuclear distance. At the time we made the simulations for Paper I we were not that familiar with the pair approximation, yet. Thus, in Paper I we replace the attractive Coulomb interaction by a pseudo potential of the form [Corso et al., 1996]

$$V_{\text{PP}}(r) = -\frac{\text{erf}(\alpha_c r)}{r} + (a + br^2)e^{-\alpha r^2}. \tag{5.2}$$

The parametres $\alpha_c = 3.8638$, $\alpha = 7.8857$, $a = 1.6617$ and $b = -18.2913$ were fitted using direct numerical solution to give the exact ground state energy of hydrogen atom and the wave function accurately outside a cut-off radius of about $0.6\ a_0$. Also, a number of lowest energy orbitals of the hydrogen atom are obtained accurately outside the same cut-off radius [Kylänpää, 2006]. Because the bond length of H_2^+ is about $2\ a_0$, it is expected that bonding of the hydrogen molecule ion becomes properly described.

5.1.1 Spectroscopic constants

Within the BO approximation of diatomic molecules the corrections to electronic energies due to the rovibrational motion of the nuclei can be evaluated from a Dunham polynomial [Alexander and Coldwell, 2005]

$$\begin{aligned} E_{vJ} = &- D_e + \omega_\mathrm{e}(v+\frac{1}{2}) - \omega_\mathrm{e}x_\mathrm{e}(v+\frac{1}{2})^2 \\ &+ B_\mathrm{e}J(J+1) - \alpha_\mathrm{e}J(J+1)(v+\frac{1}{2}) + \ldots, \end{aligned} \tag{5.3}$$

where v and J are vibrational and rotational quantum numbers, respectively, and B_e, ω_e, $\omega_\mathrm{e}x_\mathrm{e}$ and α_e are the spectroscopic constants.

The spectroscopic constants of H_2^+ and D_2^+ are obtained as introduced in Alexander and Coldwell [2005]. In atomic units

$$B_\mathrm{e} = \frac{1}{2\mathrm{I}} = \frac{1}{2\mu R^2}, \tag{5.4}$$

$$\omega_\mathrm{e} = \Big(\frac{1}{\mu}\frac{\mathrm{d}^2E}{\mathrm{d}R^2}\Big)^{1/2}, \tag{5.5}$$

$$\omega_\mathrm{e}x_\mathrm{e} = \frac{1}{48\mu}\Big[5\Big(\frac{\mathrm{d}^3E/\mathrm{d}R^3}{\mathrm{d}^2E/\mathrm{d}R^2}\Big)^2 - 3\frac{\mathrm{d}^4E/\mathrm{d}R^4}{\mathrm{d}^2E/\mathrm{d}R^2}\Big] \tag{5.6}$$

and

$$\alpha_\mathrm{e} = -\frac{6B_\mathrm{e}^2}{\omega_\mathrm{e}}\Big[\frac{R}{3}\frac{\mathrm{d}^3E/\mathrm{d}R^3}{\mathrm{d}^2E/\mathrm{d}R^2} + 1\Big]. \tag{5.7}$$

Instead of determining these constants at the equilibrium distance only, as in Alexander and Coldwell [2005], we evaluate expectation values from the distribution of nuclei, e.g. for the rotational constant,

$$B_\mathrm{e} = \frac{1}{2\mu}\int g(R)\frac{1}{R^2}\mathrm{d}R, \tag{5.8}$$

where the pair correlation function $g(R)$ is normalized to unity and includes the R^2 weight. The other constants, Eqs. (5.5)–(5.7), are evaluated similarly.

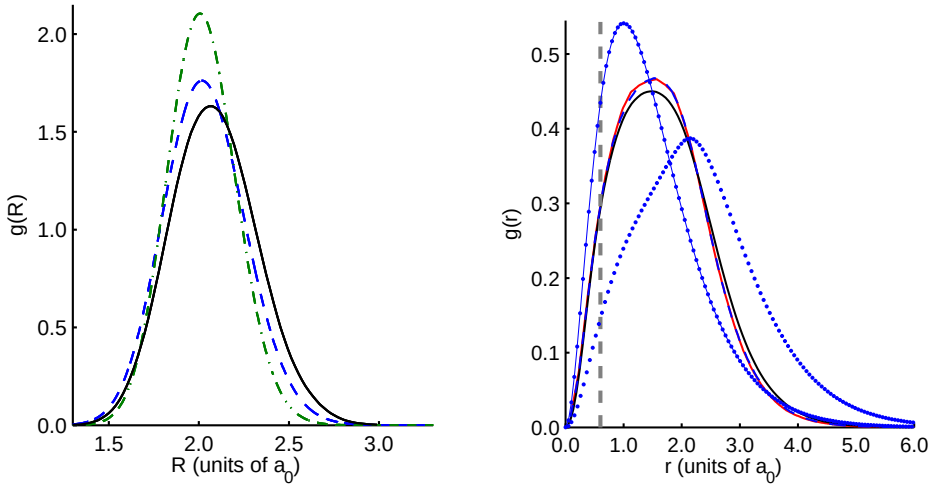

Figure 5.1: (LEFT) Nuclear pair correlation functions: H_2^+ AQ (solid), H_2^+ QN (dashed) and D_2^+ QN (dash-dotted). The difference in the average nuclear separation between QN and AQ H_2^+ is $0.056(3)\ a_0$. (RIGHT) H_2^+ electron–nucleus pair correlation functions: AQ (solid, second lowest curve), AQ projection to $R \approx 2.0\ a_0$ (solid) and BO at $R = 2.0\ a_0$ (dashed). The latter two almost coincide. Dashed vertical line indicates the size of the pseudo potential core, $r = 0.6\ a_0$. For comparison corresponding pair correlation functions for hydrogen atom (dotted line) and H_2^+ (dotted) obtained by using the analytical ground state wave function of hydrogen atom are also shown.

5.1.2 Nuclear dynamics and isotope effect

Quantum dynamics of the system is well described and distinct features of coupling are observed for the nuclei: shift of $0.056\ a_0$ in the equilibrium bond length, increase of $0.040\ a_0$ in the width of the pair correlation function of the nuclei and nonadiabatic correction of about $0.00097\ E_{\mathrm{H}}$ to dissociation energy. Electronic distribution is less influenced by the coupling than the nuclear one upon the inclusion of nonadiabatic effects.

For the quantum dynamics of the nuclei only we consider both H_2^+ and D_2^+ to find the isotope effect. The average nuclear separation of $2.019(1)\ a_0$ for H_2^+ and $2.007(2)\ a_0$ for the isotope D_2^+ is found with Trotter number $M \geq 2^6$. The full width at half maximum (FWHM) of the pair correlation functions are $0.539(1)\ a_0$ and $0.454(1)\ a_0$ for these isotopes, respectively.

Projection of the nonadiabatic three-body system with the help of Morse wave functions onto two-body nuclei-only subsystem indicates that Morse potential is not capable of describing nonadiabatic effects correctly.

5.2 Thermal dissociation of dipositronium

Dipositronium or positronium molecule, Ps_2, is a four-body system consisting of two electrons and two positrons. The dynamical stability of dipositronium was established in 1947 by Hylleraas and Ore [1947]. However, the molecule was not observed experimentally until recently by Cassidy and Mills Jr. [2007], even though a lot of knowledge had been provided by a number of theoretical studies, see Kinghorn and Poshusta [1993], Poshusta and Kinghorn [1996], Bressanini et al. [1997], Usukura et al. [1998], Usukura and Suzuki [1998], Schrader [2004], Bailey and Frolov [2005] and references therein. In addition to the fundamental issues of physics, Ps_2 is of interest also in astrophysical applications and solid state physics [Bubin and Adamowicz, 2006, Emami-Razavi, 2008].

In laboratory conditions, Ps_2 formation has recently been observed resulting from implantation of intense pulses of positrons into porous silica films by Cassidy and Mills Jr. [2007, 2008].

For the dipositronium molecule the concept of interatomic distance needs to be defined for evaluation. We should note that at the "equilibrium distance" the centers-of-mass of all four particles are superimposed on the same location, as evaluated from their one particle distributions (or wavefunctions). However, the particles do have well-defined (correlated) average distances. Thus, the definition is not trivial. The correlated definition is given as the expectation value of the separation of the two e^-e^+ dipoles, R_{dd}.

Our simulations lead to "thermal dissociation" at about 900 K, which can be explained by the strong temperature dependence of the Ps_2 free energy. With rising temperature the free energy of the two atoms decreases below that of the molecule, leading to transition from the molecular dominance to the atomic one. From our simulations we find the following surprising features: (i) the low temperature, where the transition takes place, (ii) sharpness of the transition and (iii) almost negligible density dependence at the experimentally relevant densities.

5.2.1 van der Waals interaction

At larger atomic distances it is the van der Waals interaction or the so-called dispersion forces, that are expected to contribute to the potential curve. These arise from the "dynamic dipole–dipole correlations", as usually quoted. Now, within our PIMC approach we have a transparent way to consider these interactions: the dipoles and their relative orientations. Thus, we monitor the dipole–dipole orientation correlation

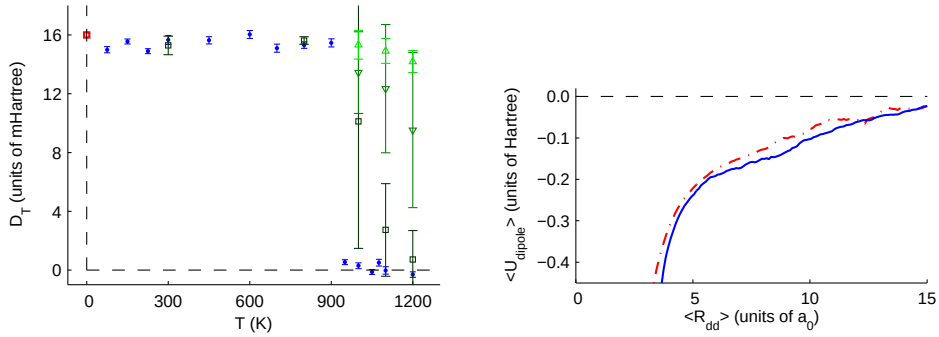

Figure 5.2: (LEFT) Apparent temperature dependent dissociation energy of dipositronium in units of mHartree: zero Kelvin reference (red square) and finite temperature simulation results at the low density limit (blue dots). Data from higher Ps density simulations are also shown (green): 0.50 (□), 14 ($\bigtriangledown$) and 100×10^{24} m^{-3} ($\bigtriangleup$). (RIGHT) Dipole–dipole interaction energy. The upper (dash-dotted, red) and lower (solid, blue) curves correspond to 1000 K and 800 K, respectively.

function

$$\left\langle \frac{\mathbf{p}_I \cdot \mathbf{p}_J}{p_I p_J} \right\rangle \tag{5.9}$$

as a function of interatomic distance R, where $\mathbf{p}_I$ and $\mathbf{p}_J$ are the two $e^- e^+$ dipoles. This function assumes values from -1 to 0, corresponding orientations from perfectly opposite to fully random.

In an equilibrium simulation of the dipositronium we are not able to choose or fix the interatomic distance R. Therefore, evaluation of R dependent quantities presumes that sampling in the chosen temperature includes the relevant R with good enough statistics. This kind of data hunting turns out to be computationally challenging.

To overcome this, we have used a "close-to-equilibrium" technique by starting from 800 K distribution and raising the temperature to 1000 K, and then, applying the reverse change in temperature to obtain another estimate. In the former case we are able to follow the increase in R from the molecular region to "dissociation", while the latter follows "recombination".

Using a "close-to-equilibrium" technique we also calculated the dipole–dipole interaction energy, for which a simple fit reveals that the large distance limit ($R_{\mathrm{dd}} > 12a_0$) for the van der Waals interaction energy shows the asymptotic $R^{-\alpha}$ behavior (α roughly 6) as expected, see Paper II.

5.2.2 Positron–electron annihilation

One interesting phenomenon, which we did not include in Paper II, is the annihilation of the positron–electron pairs of the Ps_2 molecule. This is related to the contact density, that is, the probability of finding a positron and an electron at the same position. From the simulation data of Paper II we can calculate the 2γ annihilation rate, $\Gamma_{2\gamma}$, which gives the dominant contribution of the total annihilation [Frolov et al., 1995]. The 2γ annihilation rate is directly proportional to the contact density.

For dipositronium $\Gamma_{2\gamma}$ can be written as [Frolov et al., 1995, Mitroy, 2005]

$$\Gamma_{2\gamma} = N_e N_{e^+} \pi r_0^2 c a_0^{-3} \langle \delta(\mathbf{r}_e - \mathbf{r}_{e^+}) \rangle \tag{5.10a}$$

$$= N_e N_{e^+} \pi \alpha^4 c a_0^{-1} \langle \delta(\mathbf{r}_e - \mathbf{r}_{e^+}) \rangle, \tag{5.10b}$$

where N_e is the number of electrons, N_{e^+} is the number of positrons, c is the speed of light, α is the fine structure constant and $r_0 = \alpha^2 a_0$ is the classical radius of the electron:

$$\alpha = 1/137.0359895 = 0.729735308 \times 10^{-2},$$
$$c = 0.299792458 \times 10^9 m \text{ s}^{-1},$$
$$a_0 = 0.529177249 \times 10^{-10} m.$$

Thus, here we have $N_e = 2$, $N_{e^+} = 2$ and

$$\Gamma_{2\gamma} = 201.87886 \times 10^9 \ \langle \delta(\mathbf{r}_e - \mathbf{r}_{e^+}) \rangle \text{ s}^{-1}. \tag{5.11}$$

For the contact density we estimate $0.0220(3)$, where the error estimate relates to the extrapolation to origin. This yields $\Gamma_{2\gamma} = 4.44(7) \times 10^9$ s^{-1}, which coincides nicely with the values $4.411(30) \times 10^9$ s^{-1} and 4.465106×10^9 s^{-1} given in Frolov et al. [1995] and Bubin and Adamowicz [2006], respectively.

5.3 Exchange and correlation hole

Here the concept of exchange and correlation (XC) hole is briefly introduced. This is another interesting subject, which is out of the reach of the included Papers of this thesis, however, suits well below the title ”Few electron systems”.

In order to define the XC hole the concepts such as density and density matrix are rewritten in a more conventional way. The following definitions follow Buijse and Baerends [1995], Baerends and Gritsenko [1997] and Buijse and Baerends [2002].

For the study of electron correlation the two-particle reduced density matrix is used

$$\Gamma^{(2)}(1',1;2',2) = N(N-1)\int \Psi^*(1',2',3,\ldots,N)\Psi(1,2,3,\ldots,N)\,\mathrm{d}3\mathrm{d}4\cdots\mathrm{d}N,$$

which is normalized to $N(N-1)$ electron pairs for practical purposes. The used coordinate 1 denotes the space-spin coordinate $1 \equiv \boldsymbol{r}_1 s_1$. The diagonal two-density,

$$\Gamma^{(2)}(1,2) \equiv \Gamma^{(2)}(1,1;2,2),$$

can be interpreted as the probability that two electrons are simultaneously at positions $\boldsymbol{r}_1$ and $\boldsymbol{r}_2$ with spins s_1 and s_2, respectively.

The one-particle density matrix is given as

$$\gamma(1',1) = \frac{1}{N-1}\int \Gamma^{(2)}(1',1;2',2)\Big|_{2'=2}\,\mathrm{d}2,$$

which is normalized to N electrons. The diagonal one-density (or simply density) is defined as

$$\rho(1) \equiv \gamma(1,1),$$

and is interpreted as the probability that an electron is at position $\boldsymbol{r}_1$ with spin s_1.

Now, the two-density can be expressed in terms of an uncorrelated density dependent part and an XC part

$$\Gamma^{(2)}(1,2) = \rho(1)\rho(2) + \Gamma^{(2)}_{XC}(1,2). \tag{5.12}$$

The XC two-density, $\Gamma^{(2)}_{XC}(1,2)$, describes the correlation of the electrons due to the antisymmetry of the wave function (exchange) and the Coulomb interaction. For the study of electron correlation we only need to analyse the XC two-density.

In the derivation of the total hole density (or XC hole density) it is customary to first define the concept of conditional density,

$$\Gamma^{(2)}(1,2) = \rho(1)\rho^{\text{cond}}(2|1) \quad \Rightarrow \quad \rho^{\text{cond}}(2|1) = \frac{\Gamma^{(2)}(1,2)}{\rho(1)}. \tag{5.13}$$

The conditional density may be interpreted as the density of the remaining $N-1$ electrons if one electron is known to be at the space-spin coordinate 1. The XC hole density is defined similarly

$$\Gamma^{(2)}_{XC}(1,2) = \rho(1)\rho^{\text{hole}}_{xc}(2|1) \quad \Rightarrow \quad \rho^{\text{hole}}_{xc}(2|1) = \frac{\Gamma^{(2)}_{XC}(1,2)}{\rho(1)}. \tag{5.14}$$

Thus, the conditional density may now be expressed in the form

$$\rho^{\text{cond}}(2|1) = \rho(2) + \rho_{xc}^{\text{hole}}(2|1), \tag{5.15}$$

in which the XC hole clearly describes how the conditional density deviates from the uncorrelated density $\rho(2)$.

From the above definitions it is not difficult to deduce the following properties

$$\int \rho^{\text{cond}}(2|1)\ \mathrm{d}2 = N - 1, \tag{5.16a}$$

and

$$\int \rho_{xc}^{\text{hole}}(2|1)\ \mathrm{d}2 = -1. \tag{5.16b}$$

5.3.1 Fermi and Coulomb holes

At this point it is proper to separate the XC hole in two terms, i.e. the Fermi and the Coulomb holes. The Fermi hole is defined to describe the correlation due to the exchange interaction and the Coulomb hole describes predominantly the correlation between electrons of unlike spin [Buijse and Baerends, 1995]. Thus, formally this is

$$\Gamma_{XC}^{(2)}(1,2) = \Gamma_{X}^{(2)}(1,2) + \Gamma_{C}^{(2)}(1,2), \tag{5.17a}$$

or

$$\rho_{xc}^{\text{hole}}(2|1) = \rho_{x}^{\text{hole}}(2|1) + \rho_{c}^{\text{hole}}(2|1). \tag{5.17b}$$

In practice, the study of Fermi and Coulomb holes is method dependent. For example, the Hartree–Fock and the density functional theory Fermi holes are not equal, usually. Also, the exchange part is conventionally defined to include the so-called self-interaction correction, which is why the exchange hole integrates to -1. This determines that the Coulomb hole must integrate to 0.

5.3.2 Two electron systems: H_2 and He

In case of two electrons with different spins the total hole is the same as the correlation hole. However, conventionally, e.g. in Hartree–Fock, the so-called exchange hole, $\rho_{\text{x}}(2|1)$, appears even in this case. This is due to the self-interaction correction, which in this case is given as

$$\rho_{x}^{\text{hole}}(2|1) = -\frac{1}{2}\rho(2). \tag{5.18}$$

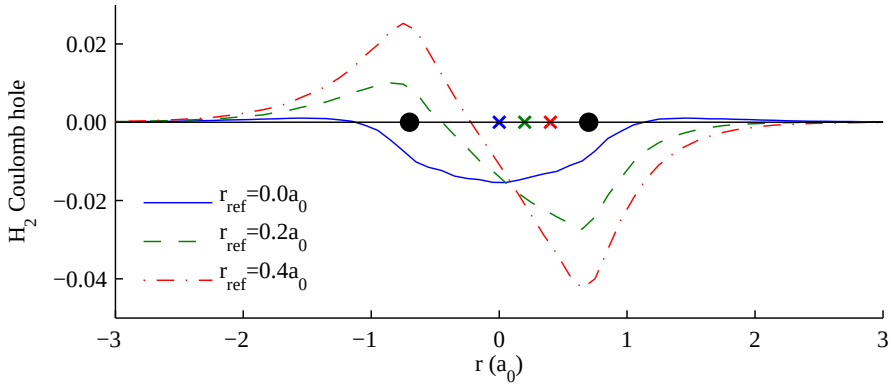

Figure 5.3: Coulomb hole according to Eq. (5.19) in the H_2 molecule along the internuclear axis for three different reference electron positions (crosses). Large dots represent the nuclei at $-0.7a_0$ and $0.7a_0$.

Note that the above expression does not depend on the position of the reference electron, i.e. $\rho_x^{\text{hole}}(2|1) = \rho_x^{\text{hole}}(2)$. Thus, conventionally for two distinguishable particles

$$\rho_{xc}^{\text{hole}}(2|1) = \rho_x^{\text{hole}}(2|1) + \rho_c^{\text{hole}}(2|1) = -\frac{1}{2}\rho(2) + \rho_c^{\text{hole}}(2|1). \tag{5.19}$$

Since the conditional and one-particle densities are relatively easily obtained using the PIMC method, the exchange and correlation holes for H_2 and He are straightforward to compute using Eqs. (5.15) and (5.19). Here, it should be further emphasized that for two electrons with unlike spin the exchange hole does not really exist — the total hole equals the correlation hole.

For two electrons systems, H_2 molecule and He atom, we have determined the XC hole, Fermi hole and the Coulomb hole using the PIMC method. For the molecule we use the Born–Oppenheimer approximation and the equilibrium internuclear distance $1.4a_0$, as is done in Buijse and Baerends [1995], Baerends and Gritsenko [1997] and Buijse and Baerends [2002].

The PIMC simulation energies are $-1.174(1)E_h^{-1}$ and $-2.307(7)E_h^{-1}$ hartree for H_2 and He, respectively. The simulations were carried out at about 160 K using time step $\tau = 0.03E_h^{-1}$. Illustrations of the Coulomb holes are given in Figs. 5.3 and 5.4, where the relatively large grid spacing $0.1a_0$ is evident from the figures. The distributions can be interpreted in the following way: the other electron is most likely found in that part of the space where the Coulomb hole has the largest values.

As expected, using the PIMC method the exchange and correlation hole results

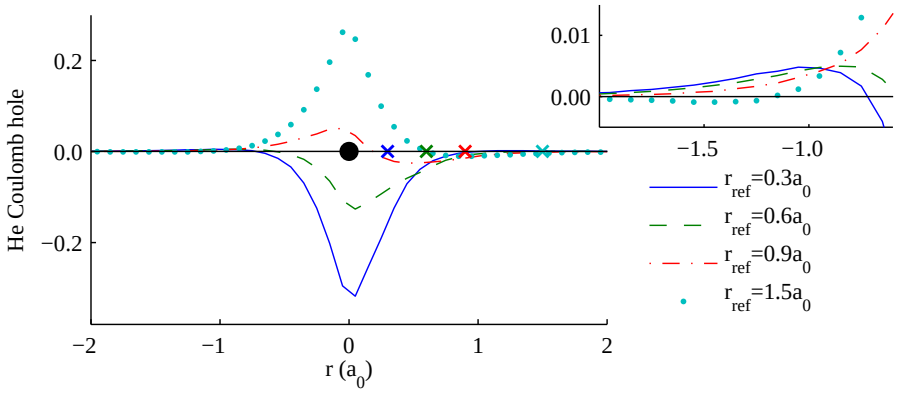

Figure 5.4: Coulomb hole according to Eq. (5.19) in the He atom for four different reference electron positions (crosses). Large dot represent the nucleus at the origin.

match perfectly with the configuration interaction results of Buijse and Baerends [1995], Baerends and Gritsenko [1997] and Buijse and Baerends [2002].

5.4 H_3^+ molecular ion

The triatomic molecular ion H_3^+ is a five-body system consisting of three protons and two electrons. Being the simplest polyatomic molecule it has been the subject of a number of theoretical and experimental studies over the years [Oka, 1992, Gottfried et al., 2003, Kutzelnigg and Jaquet, 2006, Kreckel et al., 2008, Pavanello and Adamowicz, 2009]. Experimentally, the H_3^+ ion was first detected in 1911 by Thomson [1911], however, definite spectroscopic studies were carried out not until 1980 by Oka [1980]. Since then, this five-body system has proven to be relevant, also in astrophysical studies concerning the interstellar media and the atmosphere of gas planets. Therefore, low-density high-temperature H_3^+ ion containing atmospheres have been studied experimentally [Lystrup et al., 2008] as well as computationally [Koskinen et al., 2009].

5.4.1 Quantum description of the nuclei

In Paper III we evaluate the full quantum statistics of the H_3^+ ion in a stationary state at temperatures below the thermal dissociation at about 4000 K. We monitor the fully nonadiabatic (AQ) correlated quantum distributions of particles and related energies

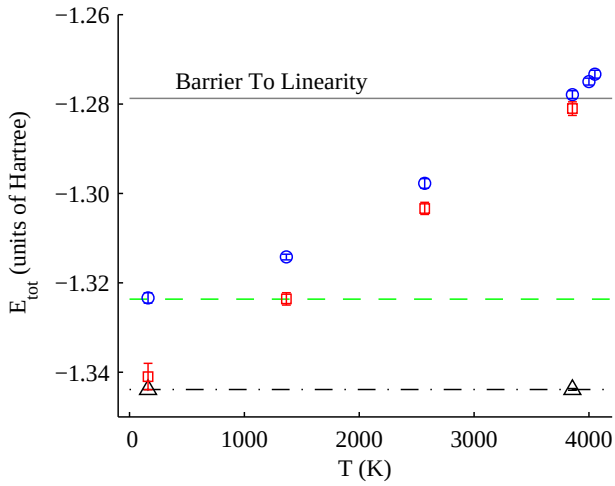

Figure 5.5: Total energy of the H_3^+ molecular ion as a function of temperature. Fully nonadiabatic quantum statistical simulations, AQ (blue circles), classical nuclei simulations, CN (red squares), and the equilibrium geometry Born–Oppenheimer simulation, BO (black triangles). Zero Kelvin data [Kutzelnigg and Jaquet, 2006, Pavanello and Adamowicz, 2009, Röhse et al., 1994] is given for comparison: BO ground state energy at equilibrium internuclear geometry (black dash-dotted line), energy including the nuclear zero-point motion (green dashed line) and energy at the barrier to linearity (grey solid line). 2SEM statistical error estimate is shown by the error bars from simulations at the H_3^+ ion density $(300a_0)^{-3}$ or $\sim 1.255 \times 10^{-6}$ gcm^{-3}.

as a function of temperature. Furthermore, we model the nuclei as classical mass points, in thermal motion (CN) and fixed as conventionally in quantum chemistry (BO), and find the difference between these and the quantum delocalized nuclei.

At our lowest simulation temperature, $T \approx 160$ K, the electronic system is essentially in its ground state. For the total energy we find $-1.3438(2)E_h$, see the BO black triangles in Fig. 5.5. The thermal energy is $k_{\mathrm{B}}T = 0.000507E_h$, and therefore, the contribution from the rotational and vibrational excited states is also small and for the total energy we find $-1.3406(29)E_h$, see the CN red square in the same Fig. The full quantum simulation includes vibrational zero-point contribution and yields $-1.3233(12)E_h$, about $0.0205(14)E_h$ above the BO energy in a good agreement with about $0.0202E_h$ in Röhse et al. [1994] and Kutzelnigg and Jaquet [2006].

From our AQ simulation we still find the equilateral triangle configuration of the nuclei with the internuclear distances increased to $\langle R \rangle = 1.723(4)a_0$, which indi-

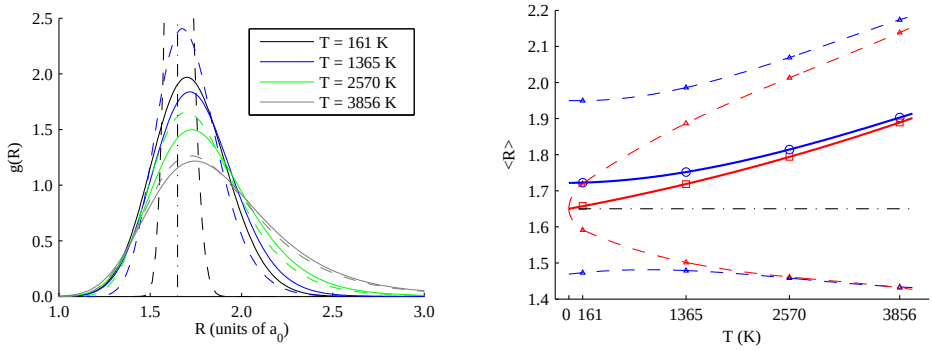

Figure 5.6: (LEFT) Nuclear pair correlation functions (bond length distributions) at different temperatures from the quantum statistical simulations (solid lines), and from the classical nuclei simulations (dashed lines). The zero Kelvin equilibrium internuclear distance is given as a vertical black dash-dotted line. The distributions include the r^2 weight and normalization to unity. (RIGHT) Expectation values of the internuclear distance at different temperatures from distributions on the left figure. Quantum statistical simulations (blue circles) and classical nuclei simulations (red squares). The FWHM limits are shown by triangles (all the lines are for guiding the eye). The zero Kelvin equilibrium internuclear distance is shown as a horizontal black dash-dotted line.

cates an increase of about $0.073(4)a_0$, as compared with the zero Kelvin BO equilibrium distance bond lengths. The thermal motion (CN), alone, increases the bond length to $\langle R \rangle = 1.658(4)a_0$, only, see the data in Fig. 5.6. This clearly points out the difference between quantum and thermal delocalization of nuclei at low T.

As expected, the increase in the total energy due to the classical rovibrational degrees of freedom is $9 \times \frac{1}{2} k_B T$, defining the slope of the CN line. The most prominent quantum feature in AQ curve is, of course, the zero-point vibration energy. At higher temperatures, however, by comparing the AQ and CN curves we see that the quantum nature of nuclear dynamics becomes less important.

The nuclear pair correlation function or bond length distributions, Fig. 5.6, follow the energetics discussed, above. There, the zero-point vibration in AQ case is seen even better. At the zero Kelvin limit both the expectation value and the distribution, in particular, are significantly different from those of the CN case. The temperature dependence in the other pair correlation functions is weak. Obviously, this is the case, because electrons do not present a quantum-to-classical transition in the temperature range considered, now.

5.4.2 First-principles dissociation–recombination equilibrium

Because of the rapid formation of H_3^+ through the exothermic reaction ($\Delta E \approx -1.7$ eV)

$$H_2 + H_2^+ \rightarrow H_3^+ + H \tag{5.20}$$

the molecular ion is expected in any active environment containing molecular hydrogen [Neale and Tennyson, 1995], and thus, it is encountered, e.g. in hydrogen plasma and in the atmosphere of giant planets [Lystrup et al., 2008, Koskinen et al., 2009]. This smallest polyatomic molecule dissociates to several fragments in a temperature and density dependent manner. Thus, at finite temperatures the equilibrium

$$\begin{aligned} H_3^+ &\leftrightarrow H_2 + p^+ \\ &\leftrightarrow H_2^+ + H \\ &\leftrightarrow 2H + p^+ \\ &\leftrightarrow H + 2p^+ + e^- \\ &\leftrightarrow 3p^+ + 2e^- \end{aligned} \tag{5.21}$$

needs to be considered, where the balance depends strongly on both the temperature and the density of H_3^+ ions.

In Paper IV the simulations of the Paper III are extended to higher temperatures where the molecular dissociation–recombination equilibrium is studied. There we also present a computationally tractable analytical function for the molecular partition function at low temperatures. In addition, we discuss about other relevant thermodynamic functions, such as heat capacity and Helmholtz free energy. Here, the main focus is given to the dissociation–recombination reaction.

To start with we first define the molecular partition function (and other molecular quantities) as the one of the system of particles that constitute the molecule. Thus, the low temperature limit gives us the conventional text book molecular partition function, in practice. However, this generalization allows us to extend the concept of molecular partition function (and the other molecular quantities) seamlessly to higher temperatures, where the molecule may dissociate and recombine in density and temperature dependent balance.

Similar definition of the molecule as a five-particle system allows us to carry out simulations of the full quantum statistics of the H_3^+ ion, now described by Eq. (5.21), at low densities and temperatures ranging from 160 K up to about 15000 K. The considered low densities given as mass densities are $\sim 1.255 \times 10^{-6}$ gcm^{-3}, $\sim 3.388 \times 10^{-5}$ gcm^{-3} and $\sim 2.710 \times 10^{-4}$ gcm^{-3}, which are relevant to H_3^+ ion containing atmospheres [Harris et al., 2004]. These correspond to blue circles, red squares and gray triangles in Fig. 5.7, respectively.

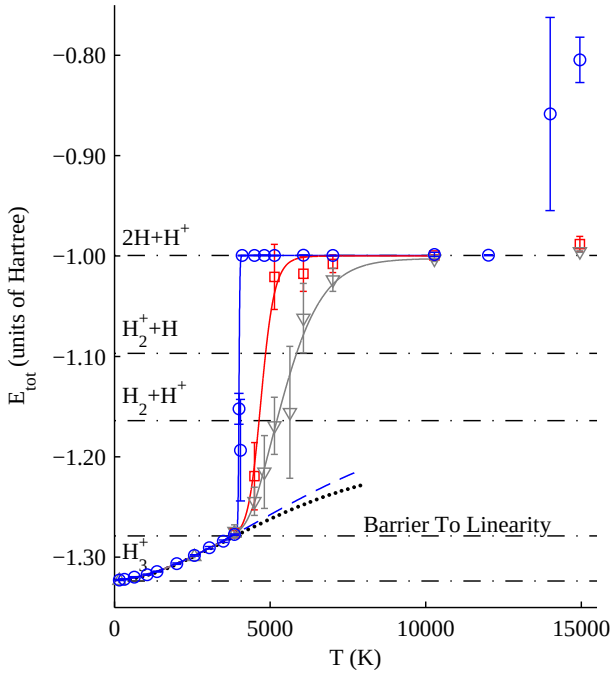

Figure 5.7: NVT total energy of the H_3^+ molecular ion as a function of temperature at three different densities. blue circles ($\sim 1.255 \times 10^{-6}$ gcm^{-3}), red squares ($\sim 3.388 \times 10^{-5}$ gcm^{-3}) and gray triangles ($\sim 2.710 \times 10^{-4}$ gcm^{-3}). The blue dashed line is the energy from the analytical fit of this work. The black dots give the energy computed using the partition function fit given in Neale and Tennyson [1995]. The horizontal dash-dotted lines are the nonadiabatic zero Kelvin energies for the ion, its fragments and the barrier to linearity. The high temperature solid lines are mainly for guiding the eye, but used for numerical evaluation of the partition function, later.

Molecular energetics

Within the considered molecular densities $T \approx 4000$ K can be regarded as apparent dissociation temperature. The energetics below 4000 K is so close to density independent that the differences between the three curves in Fig. 5.7 can not be seen.

Above 4000 K the density dependence is clearly seen as varying composition of fragments. In the range from 4000 to 10000 K the changing dissociation–recombination balance leads to distinctly different energetics, and above that, at our highest simulation temperatures the thermal ionization of hydrogen atoms starts contributing to the energy. However, it is worth pointing out that the temperature limits of these

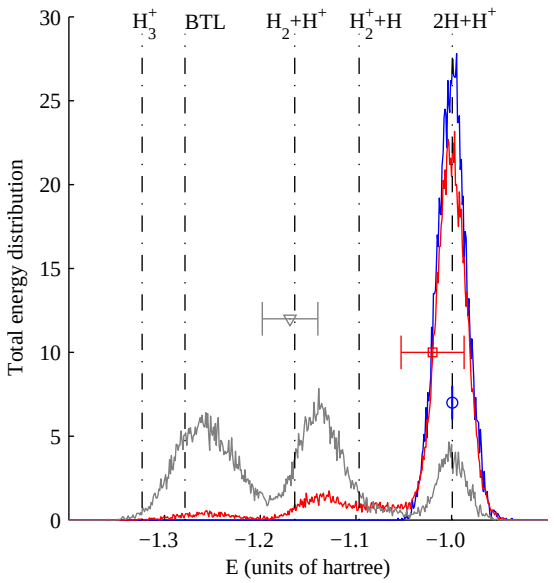

Figure 5.8: Histogram of total energy sampling pinned in boxes of width $0.001E_h$ from $(2 \times 10^4) \times 10^5$, or more, Monte Carlo samples averaged over blocks of 10^5 samples. The energy expectation values are also given with 2SEM error estimates. The temperature and Trotter number are ~ 5139.6 K and 2048, respectively. The histograms are normalized to unity for all three densities. Other notations are taken from Fig. 5.7.

three ranges, i.e. about $0 - 4000$ K, about $4000 - 10000$ K and above 10000 K, are subject to changes with larger variation of densities.

Above 10000 K in our lowest density case the thermal ionization of H atoms is evident, see Fig. 5.7, but for our higher density cases some 15000 K is needed to bring up first signs of ionization. Similar trend for the ionization is stated in Koskinen et al. [2010], although there the density is notably less than our lowest one.

Let us now consider the dissociation–recombination reaction chain, Eq. (5.21), and the contributing fragments to the quantum statistical NVT equilibrium trying to give an intuitive classical-like picture of the composition. At zero Kelvin β would be infinite, however, at finite T we have finite β, that brings classical nature to the system the more, the higher the temperature. In other words, the partial decoherence in our five particle quantum system increases with increasing temperature, that enables us to distinguish the fragments as separate molecules and atoms in thermal equilibrium. Based on this interpretation, we show the total energy distributions in Fig. 5.8 from

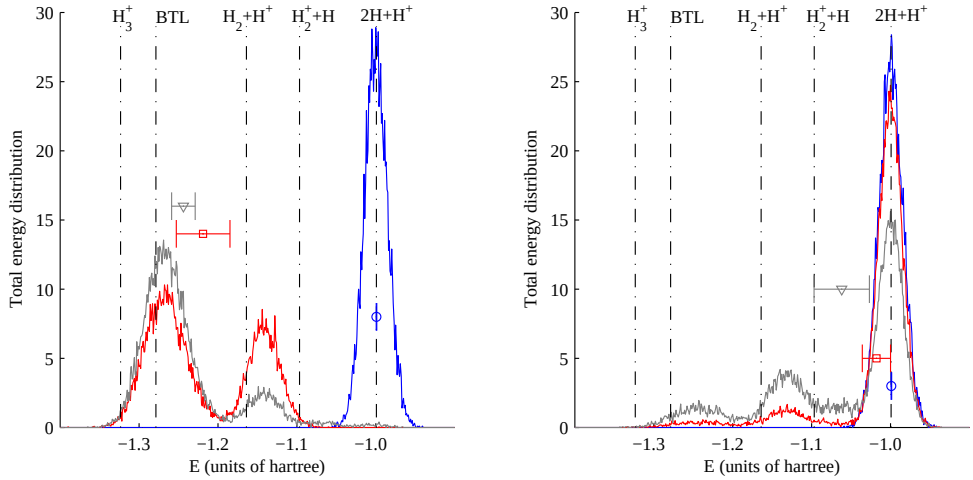

Figure 5.9: Simulation total energy distributions. (LEFT) $T \approx 4498.2$ K, (RIGHT) $T \approx 6070.3$ K. Notations are taken from Fig. 5.8.

sampling the imaginary time paths at about 5000 K with $M = 2048$ for all considered densities.

For example, for our highest density (gray in Fig. 5.8) we see three main peaks, and by inspection of that energy distribution the first and the second can clearly be assigned to the rovibrationally excited H_3^+ and H_2+H^+, respectively. As there are no rovibrational excitations available for 2H+H^+, the average position of the third main peak is very close to $-1E_h$. The fourth fragment, H_2^++H, can be identified as the small high-energy side shoulder of H_2+H^+ peak. With the interpretation of the area under the peak as the abundance of the fragment in the equilibrium we find this contribution to be much smaller than that of the others. In Fig. 5.9 the same is illustrated for two different temperatures, about 4500 K (left) and 6070 K (right), also. There at the higher temperature the amount of H_2^+ is found increased according to the same interpretation as above.

It is important to note, however, that the above illustration is dependent on the block averaging procedure, see the caption of Fig. 5.8. Pinning the energy data of each and every sample, i.e. choosing block of size one sample, would broaden the peaks in Fig. 5.8. At the opposite limit, all samples in one block, would give the single mean energy or the ensemble average corresponding to the quantum statistical expectation value. From the highest density to the lowest the expectation values are $-1.169(29)E_h$, $-1.020(33)E_h$ and $-0.9995(4)$, respectively, Figs. 5.7 and 5.8, where the statistical uncertainty decreases with increasing simulation length.

Conclusions

Path integral Monte Carlo (PIMC) method is shown to be a powerful tool for the study of quantum many-body effects. The method is basis set and trial wave function free approach and includes the Coulomb interactions exactly. Thus, we are able to extend the traditional *ab initio* quantum chemistry with full account of correlations to finite temperatures without approximations, also including the nonadiabatic contributions, if desired. Here, the method was applied to studies of the quantum chemistry of some small molecules.

It is fair to admit, however, that the PIMC method is computationally heavy for good statistical accuracy and approximations are needed, for example, to solve the "Fermion sign problem" in cases where exchange interaction becomes essential. For the articles included in this thesis the exchange interaction is either absent or can be considered negligible.

In Paper I, a three-body quantum system, hydrogen molecule ion H_2^+, was revisited, once again. There we concentrated on the electron–nuclei coupling effects in the three-body all-quantum, i.e. nonadiabatic, molecule. Among others we evaluated spectroscopic constants and molecular deformation, also considering the isotope effects. Quantum dynamics of the system is well described and distinct features of coupling are observed for the nuclei: shift in the equilibrium bond length, increase in the width of the pair correlation function of the nuclei, and a nonadiabatic correction to dissociation energy. Electronic distribution is less influenced by the coupling than the nuclear one upon the inclusion of nonadiabatic effects.

In Paper II, we have found and explained the surprising thermal instability of the dipositronium molecule, Ps_2. Due to the strong temperature dependence of the free energy of the considered four particle system the molecular form is less stable than two positronium atoms above about 900 K, though the molecular dissociation energy is ~ 0.4 eV. The transition in equilibrium from molecules to atoms is sharp in temperature and only weakly density dependent. This can be understood by the large entropy factor originating from strong delocalization of all of the molecular constituents. Our prediction remains to be experimentally verified.

In Paper III, the quantum statistics of the five-particle molecule, H_3^+ ion, was examined. There we show how contributions from quantum and thermal dynamics to particle distributions and correlation functions can be sorted out, and furthermore, how quantum to classical dynamics transition can be monitored. At our lowest temperature the zero Kelvin data from conventional quantum chemistry is reproduced accurately, as well as the vibrational zero-point energy. We find the increase in the bond length due to the nonadiabatic zero-point vibration to be about nine times larger than that given by the classical thermal motion of the nuclei. At low temperatures the necessity of the fully quantum mechanical approach for all five particles was established.

In Paper IV, the nonadiabatic simulations of Paper III are extended to higher temperatures, also, where the molecular dissociation–recombination equilibrium is found and analyzed. The temperature dependent mixed state description of the H_3^+ ion, the density dependent equilibrium dissociation–recombination balance and the energetics was evaluated for the first time. At about 4000 K the fragments of the molecule, H_2+H^+, H_2^++H and 2H+H^+, start contributing. Therefore, H_3^+ ion becomes less dominant, and eventually negligible in high enough T. In addition, using the partial decoherence in the mixed state we interpret the fragment composition of the equilibrium reaction. Also, an accurate analytical functional form for the internal energy is given below dissociation temperature. This study gives major additions to the earlier published studies found in the literature, where the dissociation–recombination reaction has been neglected.

Appendix A

s-wave "miracle" (derivation)

In this section we concentrate on deriving the relative motion density matrix in case of the Coulomb interaction, that is,

$$\rho_{\text{rel}}(\boldsymbol{r},\boldsymbol{r}';\tau) = -\frac{1}{4\pi(x-y)}\Big(\frac{\partial}{\partial x}-\frac{\partial}{\partial y}\Big)\rho_0(x,y;\tau). \tag{A.1}$$

The expression above was given in Eq. (3.8), already.

The derivation follows closely the paper by Hostler and Pratt [1963]. However, here we start from the Bloch equation for the density matrix of relative motion

$$\left[\frac{\partial}{\partial\beta}-\lambda\nabla_2^2+\frac{Z_1Z_2}{r_2}\right]\rho_{\text{rel}}(\boldsymbol{r}_1,\boldsymbol{r}_2;\beta)=0 \tag{A.2}$$

with appropriate initial conditions $\rho_{\text{rel}}(\boldsymbol{r}_1,\boldsymbol{r}_2;0)=\delta^{(3)}(\boldsymbol{r}_1-\boldsymbol{r}_2)$.

First, we define a function

$$F(r_1,r_2,|\boldsymbol{r}_2-\boldsymbol{r}_1|;\beta) = -4\pi|\boldsymbol{r}_2-\boldsymbol{r}_1|\rho_{\text{rel}}(\boldsymbol{r}_1,\boldsymbol{r}_2;\beta) \tag{A.3}$$

$$\Longrightarrow \rho_{\text{rel}}(\boldsymbol{r}_1,\boldsymbol{r}_2;\beta) = \frac{F(r_1,r_2,|\boldsymbol{r}_2-\boldsymbol{r}_1|;\beta)}{-4\pi|\boldsymbol{r}_2-\boldsymbol{r}_1|}. \tag{A.4}$$

Second, let's construct an equation for F. Then, we must calculate the Laplacian

$$\nabla_2^2\left(\frac{F(r_1,r_2,|\boldsymbol{r}_2-\boldsymbol{r}_1|;\beta)}{-4\pi|\boldsymbol{r}_2-\boldsymbol{r}_1|}\right) = \ ? \tag{A.5}$$

Since

$$\frac{\partial}{\partial x_2}\left(\frac{F(r_1,r_2,|\boldsymbol{r}_2-\boldsymbol{r}_1|;\beta)}{-4\pi|\boldsymbol{r}_2-\boldsymbol{r}_1|}\right) = -\frac{1}{4\pi}\left[-\frac{x_2-x_1}{|\boldsymbol{r}_2-\boldsymbol{r}_1|}F+\frac{1}{|\boldsymbol{r}_2-\boldsymbol{r}_1|}\frac{\partial F}{\partial x_2}\right], \tag{A.6}$$

we have

$$\frac{\partial^2}{\partial x_2^2}\left(\frac{F(r_1,r_2,|\boldsymbol{r}_2-\boldsymbol{r}_1|;\beta)}{-4\pi|\boldsymbol{r}_2-\boldsymbol{r}_1|}\right) = -\frac{1}{4\pi}\left[\left(3\frac{(x_2-x_1)^2}{|\boldsymbol{r}_2-\boldsymbol{r}_1|^5}-\frac{1}{|\boldsymbol{r}_2-\boldsymbol{r}_1|^3}\right)F - 2\frac{x_2-x_1}{|\boldsymbol{r}_2-\boldsymbol{r}_1|^3}\frac{\partial F}{\partial x_2} + \frac{1}{|\boldsymbol{r}_2-\boldsymbol{r}_1|}\frac{\partial^2 F}{\partial x_2^2}\right]. \tag{A.7}$$

Thus,

$$\nabla_2^2\left(\frac{F}{-4\pi|\boldsymbol{r}_2-\boldsymbol{r}_1|}\right) = -\frac{1}{4\pi|\boldsymbol{r}_2-\boldsymbol{r}_1|}\left[\nabla_2^2 - 2\frac{\boldsymbol{r}_2-\boldsymbol{r}_1}{|\boldsymbol{r}_2-\boldsymbol{r}_1|^2}\cdot\nabla_2\right]F. \tag{A.8}$$

So, the Bloch equation may be written as

$$\begin{aligned}
&\left[\frac{\partial}{\partial\beta}-\lambda\nabla_2^2+\frac{Z_1Z_2}{r_2}\right]\frac{F}{-4\pi|\boldsymbol{r}_2-\boldsymbol{r}_1|}=0\\
\Leftrightarrow&\frac{1}{-4\pi|\boldsymbol{r}_2-\boldsymbol{r}_1|}\left[\frac{\partial}{\partial\beta}-\lambda\left(\nabla_2^2-2\frac{\boldsymbol{r}_2-\boldsymbol{r}_1}{|\boldsymbol{r}_2-\boldsymbol{r}_1|^2}\cdot\nabla_2\right)+\frac{Z_1Z_2}{r_2}\right]F=0\\
\Leftrightarrow&\left[\frac{\partial}{\partial\beta}-\lambda\left(\nabla_2^2-2\frac{\boldsymbol{r}_2-\boldsymbol{r}_1}{|\boldsymbol{r}_2-\boldsymbol{r}_1|^2}\cdot\nabla_2\right)+\frac{Z_1Z_2}{r_2}\right]F=0.
\end{aligned} \tag{A.9}$$

At the end the equation was multiplied by $-4\pi|\boldsymbol{r}_2-\boldsymbol{r}_1|$ on both sides.

Next we will consider $F=F(\sigma,\rho,r_1;\beta)$, where $\sigma=r_1+r_2$ and $\rho=|\boldsymbol{r}_2-\boldsymbol{r}_1|$, and find out a new equation for F with these variables. Let's derive the derivatives. The first derivative is

$$\begin{aligned}
\frac{\partial F(\sigma,\rho,r_1;\beta)}{\partial x_2} &= \frac{\partial F}{\partial\sigma}\frac{\partial\sigma}{\partial x_2}+\frac{\partial F}{\partial\rho}\frac{\partial\rho}{\partial x_2}\\
&= \frac{\partial F}{\partial\sigma}\frac{x_2}{r_2}+\frac{\partial F}{\partial\rho}\frac{x_2-x_1}{|\boldsymbol{r}_2-\boldsymbol{r}_1|},
\end{aligned} \tag{A.10}$$

and the second derivative is

$$\begin{aligned}
\frac{\partial^2 F(\sigma,\rho,r_1;\beta)}{\partial x_2^2} &= \frac{\partial}{\partial x_2}\left[\frac{\partial F}{\partial\sigma}\frac{x_2}{r_2}+\frac{\partial F}{\partial\rho}\frac{x_2-x_1}{|\boldsymbol{r}_2-\boldsymbol{r}_1|}\right]\\
&= \left(\frac{\partial^2 F}{\partial\sigma^2}\frac{\partial\sigma}{\partial x_2}+\frac{\partial^2 F}{\partial\sigma\partial\rho}\frac{\partial\rho}{\partial x_2}\right)\frac{x_2}{r_2}+\frac{\partial F}{\partial\sigma}\frac{\partial}{\partial x_2}\left(\frac{x_2}{r_2}\right)\\
&\quad+\left(\frac{\partial^2 F}{\partial\sigma\partial\rho}\frac{\partial\sigma}{\partial x_2}+\frac{\partial^2 F}{\partial\rho^2}\frac{\partial\rho}{\partial x_2}\right)\frac{x_2-x_1}{|\boldsymbol{r}_2-\boldsymbol{r}_1|}+\frac{\partial F}{\partial\rho}\frac{\partial}{\partial x_2}\left(\frac{x_2-x_1}{|\boldsymbol{r}_2-\boldsymbol{r}_1|}\right)\\
&= \frac{\partial^2 F}{\partial\sigma^2}\frac{x_2^2}{r_2^2}+\frac{\partial^2 F}{\partial\rho^2}\frac{(x_2-x_1)^2}{|\boldsymbol{r}_2-\boldsymbol{r}_1|^2}+2\frac{\partial^2 F}{\partial\sigma\partial\rho}\frac{x_2(x_2-x_1)}{r_2|\boldsymbol{r}_2-\boldsymbol{r}_1|}\\
&\quad+\frac{\partial F}{\partial\sigma}\left(\frac{1}{r_2}-\frac{x_2^2}{r_2^3}\right)+\frac{\partial F}{\partial\rho}\left(\frac{1}{|\boldsymbol{r}_2-\boldsymbol{r}_1|}-\frac{(x_2-x_1)^2}{|\boldsymbol{r}_2-\boldsymbol{r}_1|^3}\right).
\end{aligned} \tag{A.11}$$

Thus,

$$\begin{aligned}&\nabla_2^2 F(\sigma,\rho,r_1;\beta)\\&= \frac{\partial^2 F}{\partial\sigma^2} + \frac{\partial^2 F}{\partial\rho^2} + 2\frac{\partial^2 F}{\partial\sigma\partial\rho}\frac{\boldsymbol{r}_2\cdot(\boldsymbol{r}_2-\boldsymbol{r}_1)}{r_2|\boldsymbol{r}_2-\boldsymbol{r}_1|} + \frac{\partial F}{\partial\sigma}\frac{2}{r_2} + \frac{\partial F}{\partial\rho}\frac{2}{|\boldsymbol{r}_2-\boldsymbol{r}_1|}\end{aligned} \tag{A.12}$$

and

$$\begin{aligned}&-2\frac{\boldsymbol{r}_2-\boldsymbol{r}_1}{|\boldsymbol{r}_2-\boldsymbol{r}_1|^2}\cdot\nabla_2 F(\sigma,\rho,r_1;\beta)\\&= -2\frac{\boldsymbol{r}_2-\boldsymbol{r}_1}{|\boldsymbol{r}_2-\boldsymbol{r}_1|^2}\cdot\frac{\partial F}{\partial\sigma}\frac{\boldsymbol{r}_2}{r_2} - 2\frac{\boldsymbol{r}_2-\boldsymbol{r}_1}{|\boldsymbol{r}_2-\boldsymbol{r}_1|^2}\cdot\frac{\partial F}{\partial\rho}\frac{\boldsymbol{r}_2-\boldsymbol{r}_1}{|\boldsymbol{r}_2-\boldsymbol{r}_1|}\\&= -\frac{\partial F}{\partial\sigma}\left[\frac{2\boldsymbol{r}_2\cdot(\boldsymbol{r}_2-\boldsymbol{r}_1)}{r_2|\boldsymbol{r}_2-\boldsymbol{r}_1|^2}\right] - \frac{\partial F}{\partial\rho}\left[\frac{2}{|\boldsymbol{r}_2-\boldsymbol{r}_1|}\right]\end{aligned} \tag{A.13}$$

Now, the derivative part of the Bloch equation for F can be written as

$$\begin{aligned}&\left(\nabla_2^2 - 2\frac{\boldsymbol{r}_2-\boldsymbol{r}_1}{|\boldsymbol{r}_2-\boldsymbol{r}_1|^2}\cdot\nabla_2\right)F\\&= \frac{\partial^2 F}{\partial\sigma^2} + \frac{\partial^2 F}{\partial\rho^2} + \frac{2\boldsymbol{r}_2\cdot(\boldsymbol{r}_2-\boldsymbol{r}_1)}{r_2|\boldsymbol{r}_2-\boldsymbol{r}_1|}\frac{\partial^2 F}{\partial\sigma\partial\rho} + \left(\frac{2}{r_2} - \frac{2\boldsymbol{r}_2\cdot(\boldsymbol{r}_2-\boldsymbol{r}_1)}{r_2|\boldsymbol{r}_2-\boldsymbol{r}_1|^2}\right)\frac{\partial F}{\partial\sigma}.\end{aligned} \tag{A.14}$$

Next, let's modify the r-dependent terms into the variables σ, ρ and r_1 defined earlier. First the cross-derivative term

$$\begin{aligned}\frac{2\boldsymbol{r}_2\cdot(\boldsymbol{r}_2-\boldsymbol{r}_1)}{r_2|\boldsymbol{r}_2-\boldsymbol{r}_1|} &= \frac{2\boldsymbol{r}_2\cdot\boldsymbol{r}_2 - 2\boldsymbol{r}_2\cdot\boldsymbol{r}_1}{r_2|\boldsymbol{r}_2-\boldsymbol{r}_1|}\\&= \frac{r_1^2+r_2^2-2\boldsymbol{r}_2\cdot\boldsymbol{r}_1 - r_1^2 - r_2^2 - 2r_1r_2 + 2\boldsymbol{r}_2\cdot\boldsymbol{r}_2 + 2r_1r_2}{r_2|\boldsymbol{r}_2-\boldsymbol{r}_1|}\\&= \frac{|\boldsymbol{r}_2-\boldsymbol{r}_1|^2 - (r_1+r_2)^2 + 2(r_1+r_2)r_2}{r_2|\boldsymbol{r}_2-\boldsymbol{r}_1|}\\&= \frac{\rho^2-\sigma^2+2\sigma(\sigma-r_1)}{(\sigma-r_1)\rho}\\&= \frac{\rho^2+\sigma^2-2\sigma r_1}{(\sigma-r_1)\rho},\end{aligned} \tag{A.15}$$

and then the other term

$$\begin{aligned}\frac{2}{r_2} - \frac{2\boldsymbol{r}_2\cdot(\boldsymbol{r}_2-\boldsymbol{r}_1)}{r_2|\boldsymbol{r}_2-\boldsymbol{r}_1|^2} &= \frac{2|\boldsymbol{r}_2-\boldsymbol{r}_1|^2 - 2\boldsymbol{r}_2\cdot(\boldsymbol{r}_2-\boldsymbol{r}_1)}{r_2|\boldsymbol{r}_2-\boldsymbol{r}_1|^2}\\&= \frac{2\rho^2 - (\rho^2+\sigma^2-2\sigma r_1)}{(\sigma-r_1)\rho^2}\\&= \frac{\rho^2-\sigma^2+2\sigma r_1}{(\sigma-r_1)\rho^2}.\end{aligned} \tag{A.16}$$

So, the Bloch equation now becomes

$$\left[\frac{\partial}{\partial\beta} - \lambda\left(\frac{\partial^2}{\partial\sigma^2} + \frac{\partial^2}{\partial\rho^2} + \frac{\rho^2+\sigma^2-2\sigma r_1}{(\sigma-r_1)\rho}\frac{\partial^2}{\partial\sigma\partial\rho} + \frac{\rho^2-\sigma^2+2\sigma r_1)}{(\sigma-r_1)\rho^2}\frac{\partial}{\partial\sigma}\right) + \frac{Z_1Z_2}{\sigma-r_1}\right] F(\sigma,\rho,r_1;\beta) = 0. \tag{A.17}$$

Defining $F = \frac{\partial}{\partial\rho}D$, the equation above can be written as

$$\frac{\partial}{\partial\rho}\left[\frac{\partial}{\partial\beta} - \lambda\left(\frac{\partial^2}{\partial\sigma^2} + \frac{\partial^2}{\partial\rho^2} + \frac{\rho^2+\sigma^2-2\sigma r_1}{(\sigma-r_1)\rho}\frac{\partial^2}{\partial\sigma\partial\rho}\right) + \frac{Z_1Z_2}{\sigma-r_1}\right] D(\sigma,\rho,r_1;\beta) = 0, \tag{A.18}$$

since

$$\begin{aligned}
&\frac{\partial}{\partial\rho}\left(\frac{\partial^2}{\partial\sigma^2} + \frac{\partial^2}{\partial\rho^2} + \frac{\rho^2+\sigma^2-2\sigma r_1}{(\sigma-r_1)\rho}\frac{\partial^2}{\partial\sigma\partial\rho}\right) D(\sigma,\rho,r_1;\beta) \\
&= \frac{\partial^2}{\partial\sigma^2}\frac{\partial D}{\partial\rho} + \frac{\partial^2}{\partial\rho^2}\frac{\partial D}{\partial\rho} + \frac{\rho^2+\sigma^2-2\sigma r_1}{(\sigma-r_1)\rho}\frac{\partial^2}{\partial\sigma\partial\rho}\frac{\partial D}{\partial\rho} \\
&\quad + \left[\frac{2\rho}{(\sigma-r_1)\rho} - \frac{\rho^2+\sigma^2-2\sigma r_1}{(\sigma-r_1)^2\rho^2}(\sigma-r_1)\right]\frac{\partial}{\partial\sigma}\frac{\partial D}{\partial\rho} \\
&= \frac{\partial^2}{\partial\sigma^2}F + \frac{\partial^2}{\partial\rho^2}F + \frac{\rho^2+\sigma^2-2\sigma r_1}{(\sigma-r_1)\rho}\frac{\partial^2}{\partial\sigma\partial\rho}F + \frac{\rho^2-\sigma^2+2\sigma r_1}{(\sigma-r_1)\rho^2}\frac{\partial}{\partial\sigma}F.
\end{aligned} \tag{A.19}$$

Then we again define new variables: $x = (\sigma+\rho)/2$ and $y = (\sigma-\rho)/2$. And once more we have to derive the respective derivatives for $D(x,y;\beta)$.

$$\frac{\partial}{\partial\rho}D(x,y;\beta) = \frac{\partial D}{\partial x}\frac{\partial x}{\partial\rho} + \frac{\partial D}{\partial y}\frac{\partial y}{\partial\rho} = \frac{1}{2}\left(\frac{\partial D}{\partial x} - \frac{\partial D}{\partial y}\right). \tag{A.20}$$

$$\begin{aligned}
\frac{\partial^2}{\partial\rho^2}D(x,y;\beta) &= \frac{1}{2}\frac{\partial}{\partial\rho}\left(\frac{\partial D}{\partial x} - \frac{\partial D}{\partial y}\right) \\
&= \frac{1}{2}\left(\frac{\partial^2 D}{\partial x^2}\frac{\partial x}{\partial\rho} + \frac{\partial^2 D}{\partial x\partial y}\frac{\partial y}{\partial\rho} - \frac{\partial^2 D}{\partial x\partial y}\frac{\partial x}{\partial\rho} - \frac{\partial^2 D}{\partial y^2}\frac{\partial y}{\partial\rho}\right) \\
&= \frac{1}{4}\left(\frac{\partial^2 D}{\partial x^2} + \frac{\partial^2 D}{\partial y^2} - 2\frac{\partial^2 D}{\partial x\partial y}\right).
\end{aligned} \tag{A.21}$$

$$\frac{\partial}{\partial\sigma}D(x,y;\beta) = \frac{\partial D}{\partial x}\frac{\partial x}{\partial\sigma} + \frac{\partial D}{\partial y}\frac{\partial y}{\partial\sigma} = \frac{1}{2}\left(\frac{\partial D}{\partial x} + \frac{\partial D}{\partial y}\right). \tag{A.22}$$

$$\begin{aligned}\frac{\partial^2}{\partial\sigma^2}D(x,y;\beta) &= \frac{1}{2}\frac{\partial}{\partial\sigma}\left(\frac{\partial D}{\partial x}+\frac{\partial D}{\partial y}\right)\\ &= \frac{1}{2}\left(\frac{\partial^2 D}{\partial x^2}\frac{\partial x}{\partial\sigma}+\frac{\partial^2 D}{\partial x\partial y}\frac{\partial y}{\partial\sigma}+\frac{\partial^2 D}{\partial x\partial y}\frac{\partial x}{\partial\sigma}+\frac{\partial^2 D}{\partial y^2}\frac{\partial y}{\partial\sigma}\right)\\ &= \frac{1}{4}\left(\frac{\partial^2 D}{\partial x^2}+\frac{\partial^2 D}{\partial y^2}+2\frac{\partial^2 D}{\partial x\partial y}\right).\end{aligned} \tag{A.23}$$

$$\begin{aligned}\frac{\partial^2}{\partial\sigma\partial\rho}D(x,y;\beta) &= \frac{\partial}{\partial\sigma}\frac{\partial D(x,y;\beta)}{\partial\rho}\\ &= \frac{1}{2}\frac{\partial}{\partial\sigma}\left(\frac{\partial D}{\partial x}-\frac{\partial D}{\partial y}\right)\\ &= \frac{1}{2}\left(\frac{\partial^2 D}{\partial x^2}\frac{\partial x}{\partial\sigma}+\frac{\partial^2 D}{\partial x\partial y}\frac{\partial y}{\partial\sigma}-\frac{\partial^2 D}{\partial x\partial y}\frac{\partial x}{\partial\sigma}-\frac{\partial^2 D}{\partial y^2}\frac{\partial y}{\partial\sigma}\right)\\ &= \frac{1}{4}\left(\frac{\partial^2 D}{\partial x^2}-\frac{\partial^2 D}{\partial y^2}\right).\end{aligned} \tag{A.24}$$

Now let's modify the derivative part of differential equation

$$\begin{aligned}&\left(\frac{\partial^2}{\partial\sigma^2}+\frac{\partial^2}{\partial\rho^2}+\frac{\rho^2+\sigma^2-2\sigma r_1}{(\sigma-r_1)\rho}\frac{\partial^2}{\partial\sigma\partial\rho}\right)D(x,y;\beta)\\ &=\frac{1}{4}\left(\left[2+\frac{\rho^2+\sigma^2-2\sigma r_1}{(\sigma-r_1)\rho}\right]\frac{\partial^2}{\partial x^2}+\left[2-\frac{\rho^2+\sigma^2-2\sigma r_1}{(\sigma-r_1)\rho}\right]\frac{\partial^2}{\partial y^2}\right)D(x,y;\beta)\end{aligned} \tag{A.25}$$

We see that we do not have the cross-derivative anymore. We still need to work out the coefficients in terms of x and y. The first coefficient on the right-hand side of Eq. (A.25) is

$$\begin{aligned}2+\frac{\rho^2+\sigma^2-2\sigma r_1}{(\sigma-r_1)\rho} &= \frac{2(\sigma-r_1)\rho+\rho^2+\sigma^2-2\sigma r_1}{(\sigma-r_1)\rho}\\ &= \frac{\sigma^2+\rho^2+2\sigma\rho-2\rho r_1-2\sigma r_1}{(\sigma-r_1)\rho}\\ &= \frac{(\sigma+\rho)^2-2r_1(\sigma+\rho)}{(\sigma-r_1)\rho}\\ &= \frac{(2x)^2-2r_1(2x)}{(x+y-r_1)(x-y)}\\ &= 4\frac{x^2-xr_1}{x^2-xr_1-(y^2-yr_1)},\end{aligned} \tag{A.26}$$

and the second coefficient is

$$\begin{aligned}
2-\frac{\rho^2+\sigma^2-2\sigma r_1}{(\sigma-r_1)\rho} &= \frac{2(\sigma-r_1)\rho-\rho^2-\sigma^2+2\sigma r_1}{(\sigma-r_1)\rho} \\
&= \frac{-(\sigma^2+\rho^2-2\sigma\rho)-2\rho r_1+2\sigma r_1}{(\sigma-r_1)\rho} \\
&= \frac{-(\sigma-\rho)^2+2r_1(\sigma-\rho)}{(\sigma-r_1)\rho} \\
&= -\frac{(2y)^2-2r_1(2y)}{(x+y-r_1)(x-y)} \\
&= -4\frac{y^2-yr_1}{x^2-xr_1-(y^2-yr_1)}. \qquad \text{(A.27)}
\end{aligned}$$

Therefore, the differential part may be written as

$$\begin{aligned}
&\left(\frac{\partial^2}{\partial\sigma^2}+\frac{\partial^2}{\partial\rho^2}+\frac{\rho^2+\sigma^2-2\sigma r_1}{(\sigma-r_1)\rho}\frac{\partial^2}{\partial\sigma\partial\rho}\right)D(x,y;\beta) \\
&=\left(\frac{x^2-xr_1}{x^2-xr_1-(y^2-yr_1)}\frac{\partial^2}{\partial x^2}-\frac{y^2-yr_1}{x^2-xr_1-(y^2-yr_1)}\frac{\partial^2}{\partial y^2}\right)D(x,y;\beta) \qquad \text{(A.28)}
\end{aligned}$$

Now we may write

$$\begin{aligned}
&\frac{\partial}{\partial\rho}\left[\frac{\partial}{\partial\beta}-\lambda\left(\frac{\partial^2}{\partial\sigma^2}+\frac{\partial^2}{\partial\rho^2}+\frac{\rho^2+\sigma^2-2\sigma r_1}{(\sigma-r_1)\rho}\frac{\partial^2}{\partial\sigma\partial\rho}\right)+\frac{Z_1Z_2}{\sigma-r_1}\right]D(\sigma,\rho,r_1;\beta)=0 \\
\Leftrightarrow&\frac{\partial}{\partial\rho}\left[\frac{\partial}{\partial\beta}-\lambda\left(\frac{x^2-xr_1}{x^2-xr_1-(y^2-yr_1)}\frac{\partial^2}{\partial x^2}-\frac{y^2-yr_1}{x^2-xr_1-(y^2-yr_1)}\frac{\partial^2}{\partial y^2}\right)\right. \\
&\qquad\left.+\frac{Z_1Z_2}{\sigma-r_1}\right]D(x,y;\beta)=0 \\
\Leftrightarrow&\frac{\partial}{\partial\rho}\left(\frac{1}{x^2-xr_1-(y^2-yr_1)}\right. \\
&\left[(x^2-xr_1-(y^2-yr_1))\frac{\partial}{\partial\beta}\right. \\
&-\lambda\left((x^2-xr_1)\frac{\partial^2}{\partial x^2}-(y^2-yr_1)\frac{\partial^2}{\partial y^2}\right) \\
&\left.\left.+Z_1Z_2(x-y)\right]\right)D(x,y;\beta)=0
\end{aligned}$$

$$
\begin{aligned}
\Leftrightarrow & \frac{\partial}{\partial\rho}\left(\frac{1}{x^2-xr_1-(y^2-yr_1)}\right. \\
& \Big[(x^2-xr_1-(y^2-yr_1))\frac{\partial}{\partial\beta} \\
& -\lambda\left((x^2-xr_1)\frac{\partial^2}{\partial x^2}-(y^2-yr_1)\frac{\partial^2}{\partial y^2}\right) \\
& \quad \left.+Z_1Z_2(x-r_1)-Z_1Z_2(y-r_1)\Big]\right)D(x,y;\beta)=0 \\
\Leftrightarrow & \frac{\partial}{\partial\rho}\left(\frac{1}{x^2-xr_1-(y^2-yr_1)}\right. \\
& \Big[(x^2-xr_1)\left\{\frac{\partial}{\partial\beta}-\lambda\frac{\partial^2}{\partial x^2}+\frac{Z_1Z_2}{x}\right\} \\
& -(y^2-yr_1)\left\{\frac{\partial}{\partial\beta}-\lambda\frac{\partial^2}{\partial y^2}+\frac{Z_1Z_2}{y}\right\}\Big]\Big)D(x,y;\beta)=0 \\
\Leftrightarrow & \frac{1}{2}\left(\frac{\partial}{\partial x}-\frac{\partial}{\partial y}\right)\left(\frac{1}{x^2-xr_1-(y^2-yr_1)}\right. \\
& \Big[(x^2-xr_1)\left\{\frac{\partial}{\partial\beta}-\lambda\frac{\partial^2}{\partial x^2}+\frac{Z_1Z_2}{x}\right\} \\
& -(y^2-yr_1)\left\{\frac{\partial}{\partial\beta}-\lambda\frac{\partial^2}{\partial y^2}+\frac{Z_1Z_2}{y}\right\}\Big]\Big)D(x,y;\beta)=0. \qquad \text{(A.29)}
\end{aligned}
$$

The function F defined using $D(x,y;\beta)$ is given as

$$
\begin{aligned}
F &= \frac{\partial}{\partial\rho}D(x,y;\beta) \\
&\Longrightarrow F(x,y;\beta)=\frac{1}{2}\left(\frac{\partial}{\partial x}-\frac{\partial}{\partial y}\right)D(x,y;\beta), \qquad \text{(A.30)}
\end{aligned}
$$

and thus, the density matrix is

$$
\begin{aligned}
\rho_{\text{rel}}(\boldsymbol{r}_1,\boldsymbol{r}_2;\beta) &= \frac{F(x,y;\beta)}{-4\pi(x-y)} \\
&= -\frac{1}{8\pi(x-y)}\left(\frac{\partial}{\partial x}-\frac{\partial}{\partial y}\right)D(x,y;\beta). \qquad \text{(A.31)}
\end{aligned}
$$

Now let's consider the solution $D(x,y;\beta)$ for the derived differential equation, Eq. (A.29). Trivially $D(x,y;\beta)=\rho_0(x,y;\beta)$ is one solution, since

$$
\left\{\frac{\partial}{\partial\beta}-\lambda\frac{\partial^2}{\partial x^2}+\frac{Z_1Z_2}{x}\right\}\rho_0(x,y;\beta)=0 \qquad \text{(A.32)}
$$

and

$$\left\{\frac{\partial}{\partial\beta}-\lambda\frac{\partial^2}{\partial y^2}+\frac{Z_1Z_2}{y}\right\}\rho_0(x,y;\beta)=0. \tag{A.33}$$

Therefore, also $D(x,y;\beta)=\alpha\rho_0(x,y;\beta)$, where α is an arbitrary constant, is a solution. So, we can write

$$\rho_{\text{rel}}(\boldsymbol{r}_1,\boldsymbol{r}_2;\beta)=-\frac{\alpha}{8\pi(x-y)}\left(\frac{\partial}{\partial x}-\frac{\partial}{\partial y}\right)\rho_0(x,y;\beta). \tag{A.34}$$

The constant α can be derived using the known result for the free particle, for which the s-wave "miracle" is also valid — just set the term Z_1Z_2 equal to zero. For the free particle we have

$$\begin{aligned}\rho^{\text{K}}_{\text{rel}}(\boldsymbol{r}_1,\boldsymbol{r}_2;\beta)&=-\frac{\alpha}{8\pi(x-y)}\left(\frac{\partial}{\partial x}-\frac{\partial}{\partial y}\right)\rho^{\text{K}}_0(x,y;\beta)\\&=-\frac{\alpha}{8\pi(x-y)}\left[-\frac{x-y}{\sqrt{4\pi}\,(\lambda\tau)^{3/2}}\exp\left(-\frac{(x-y)^2}{4\lambda\tau}\right)\right]\\&=\frac{\alpha}{8\pi\sqrt{4\pi}\,(\lambda\tau)^{3/2}}\exp\left(-\frac{(x-y)^2}{4\lambda\tau}\right).\end{aligned} \tag{A.35}$$

The coefficient for the free particle is known, and thus,

$$\frac{1}{\alpha}8\pi\sqrt{4\pi}\,(\lambda\tau)^{3/2}=(4\pi\lambda\tau)^{3/2}\quad\Longrightarrow\alpha=2. \tag{A.36}$$

Substitution of $\alpha=2$ to Eq. (A.31) gives us the familiar expression

$$\rho_{\text{rel}}(\boldsymbol{r}_1,\boldsymbol{r}_2;\beta)=-\frac{1}{4\pi(x-y)}\left(\frac{\partial}{\partial x}-\frac{\partial}{\partial y}\right)\rho_0(x,y;\beta). \tag{A.37}$$

At least in practice the constant $\alpha=2$ is universal, if not otherwise. Since

$$\begin{aligned}\rho_{\text{rel}}&=-\frac{\alpha}{8\pi(x-y)}\Big(\frac{\partial}{\partial x}-\frac{\partial}{\partial y}\Big)\rho_0\\&=-\frac{\alpha}{8\pi(x-y)}\Big(\frac{\partial}{\partial x}-\frac{\partial}{\partial y}\Big)\rho^{\text{K}}_0e^{-u_0}\\&=-\frac{\alpha}{8\pi(x-y)}\Big[e^{-u_0}\Big(\frac{\partial}{\partial x}-\frac{\partial}{\partial y}\Big)\rho^{\text{K}}_0-\rho^{\text{K}}_0e^{-u_0}\Big(\frac{\partial}{\partial x}-\frac{\partial}{\partial y}\Big)u_0\Big]\\&=\frac{\alpha}{2}\Big[e^{-u_0}\rho^{\text{K}}_{\text{rel}}+\frac{1}{4\pi(x-y)}\rho^{\text{K}}_0e^{-u_0}\Big(\frac{\partial}{\partial x}-\frac{\partial}{\partial y}\Big)u_0\Big]\\&=\frac{\alpha}{2}\left(\rho^{\text{K}}_{\text{rel}}e^{-u_0}+\rho^{\text{K}}_0e^{-u_0}f\right)\\&=\frac{\alpha}{2}e^{-u_0}\left(\rho^{\text{K}}_{\text{rel}}+\rho^{\text{K}}_0f\right),\end{aligned} \tag{A.38}$$

the potential is

$$\begin{aligned} u &= -\ln\left[\frac{\alpha}{2}e^{-u_0}\left(\rho_{\text{rel}}^{\text{K}}+\rho_0^{\text{K}}f\right)/\rho_{\text{rel}}^{\text{K}}\right] \\ &= -\ln\left(\frac{\alpha}{2}\right)+u_0-\ln\left(1+\frac{\rho_0^{\text{K}}}{\rho_{\text{rel}}^{\text{K}}}f\right). \end{aligned} \tag{A.39}$$

If the constant α would have a value different from 2 it could be neglected, in practice at least, since it does not modify the shape of the potential.

Appendix B

Matrix squaring: computational details

B.1 Integration

Below we give brief introductions to the integration methods used in the matrix squaring, i.e. Gauss–Hermite and Gauss–Kronrod integration. Extremely accurate values for the abscissa (x_i) and for the corresponding weight (w_i) are given in Esler [2006].

B.1.1 Gauss–Hermite

The integral derived earlier, Eq. (3.25) is of the form

$$e^{-u} = \int_{-\bar{x}}^{\infty} \mathrm{d}s f(s) e^{-\frac{s^2}{2\lambda\tau}}. \tag{B.1}$$

When $\bar{x}$ is large enough, we can write

$$e^{-u} \approx \int_{-\infty}^{\infty} \mathrm{d}s f(s) e^{-\frac{s^2}{2\lambda\tau}}, \tag{B.2}$$

in which the approximately symbol could as well be changed to equality, in practical applications. With the change of variable $x^2 = \frac{s^2}{2\lambda\tau}$ we have $\mathrm{d}s = \sqrt{2\lambda\tau}\,\mathrm{d}x$ and

$$\begin{aligned} e^{-u} &= \sqrt{2\lambda\tau} \int_{-\infty}^{\infty} \mathrm{d}x f(x\sqrt{2\lambda\tau}) e^{-x^2} \\ &\approx \sqrt{2\lambda\tau} \sum_{i=1}^{n} w_i f(x_i\sqrt{2\lambda\tau}) e^{-x_i^2} \end{aligned} \tag{B.3}$$

B.1.2 Gauss–Kronrod

Near the origin the Gauss–Hermite integration is not adequate, and thus, we use the adaptive Gauss–Kronrod (GK) integration instead. Basics of this method is given briefly here.

$$\int_a^b f(y)\mathrm{d}y = \int_{-1}^{1} g(x)\mathrm{d}x \approx \sum_{i=1}^{n} w_i g(x_i), \tag{B.4}$$

in which

$$g(x) = \frac{b-a}{2} f(\frac{b-a}{2}x + \frac{a+b}{2}). \tag{B.5}$$

Considering for example GK 7-15 an error estimate can be given as the absolute difference of the two methods

$$\epsilon = |G7 - K15|. \tag{B.6}$$

However, commonly the following is used

$$\epsilon = (200\,|G7 - K15|)^{1.5}. \tag{B.7}$$

In the adaptive scheme, if the wanted error is not achieved then we divide the interval into two segments of equal size and apply the above integration on both segments. The error criteria is also divided. If the new error criteria is met for one region, that specific region need not be further divided. This will be continued for all regions until the wanted error is achieved — or until some minimum segment size comes across.

B.2 Modified spherical Bessel function of the first kind

Modified spherical Bessel functions are defined in terms of the spherical Bessel functions. See Abramowitz and Stegun pages 443-444. For the first kind we have

$$i_l(z) = \sqrt{\frac{\pi}{2z}}\, I_{l+1/2}(z), \tag{B.8}$$

where $I_{l+1/2}(z)$ is the modified Bessel function of the first kind. Thus,

$$i_0(z) = \frac{\sinh(z)}{z}, \tag{B.9}$$

$$i_1(z) = -\frac{\sinh(z)}{z^2} + \frac{\cosh(z)}{z}, \tag{B.10}$$

$$i_2(z) = \left(\frac{3}{z^3} + \frac{1}{z}\right)\sinh(z) - \frac{3}{z^2}\frac{\cosh(z)}{z}, \tag{B.11}$$

$$\text{etc.} \tag{B.12}$$

Recurrence relations

$$i_{l-1}(z) - i_{l+1}(z) = (2l+1)z^{-1}i_l(z) \tag{B.13}$$

$$li_{l-1}(z) + (l+1)i_{l+1}(z) = (2l+1)\frac{\mathrm{d}i_l(z)}{\mathrm{d}z} \tag{B.14}$$

$$-\frac{l}{z}i_l(z) + \frac{\mathrm{d}i_l(z)}{\mathrm{d}z} = i_{l+1}(z). \tag{B.15}$$

Ascending series

$$i_l(z) = \frac{z^l}{1\cdot 3\cdot 5\ldots(2l+1)}\left[1 + \frac{\frac{1}{2}z^2}{1!(2l+3)} + \frac{\left(\frac{1}{2}z^2\right)^2}{2!(2l+3)(2l+5)} + \ldots\right]. \tag{B.16}$$

B.2.1 Computation of the $l = 0$ terms

During the squaring procedure we need to compute an exponentially scaled modified spherical bessel function of the first kind

$$m_l(z) = i_l(z)e^{-z}, \tag{B.17}$$

where $z \geq 0$. In addition, we need to calculate the derivative

$$\widetilde{m}_l'(z) = e^{-z}\frac{\mathrm{d}i_l(z)}{\mathrm{d}z}. \tag{B.18}$$

The m_0 function may be expressed as

$$\begin{aligned} m_0(z) = i_0(z)e^{-z} = \frac{\sinh(z)}{z}e^{-z} &= \frac{e^z - e^{-z}}{2z}e^{-z} \\ &= \frac{1}{2z}\left[1 - e^{-2z}\right] \qquad \text{(B.19)} \\ &= e^{-z}\left[1 + \frac{z^2}{6} + \frac{z^4}{120} + \ldots\right]. \qquad \text{(B.20)} \end{aligned}$$

For small values of z you can use the first few terms of the ascending series, Eq. (B.20). Otherwise use Eq. (B.19), which for large z (e.g. $z \geq 50$) may be approximated by $1/2z$.

The function $\widetilde{m}_0'$ may be given as

$$\begin{aligned} \widetilde{m}_0'(z) &= e^{-z}\frac{\mathrm{d}i_0(z)}{\mathrm{d}z} \\ &= \frac{(z-1) + e^{-2z}(z+1)}{2z^2} \qquad \text{(B.21)} \\ &= e^{-z}\left[\frac{z}{3} + \frac{z^3}{30} + \ldots\right]. \qquad \text{(B.22)} \end{aligned}$$

For small values of z you may use the first few terms of the ascending series, Eq. (B.22). Otherwise use Eq. (B.21), which for large z (e.g. $z \geq 50$) may be approximated by $1/2z - 1/2z^2$.

During the squaring procedure for the β-derivative you also need to evaluate the expression

$$z\frac{\widetilde{m}_0'(z)}{m_0(z)} = z\frac{\frac{(z-1)+e^{-2z}(z+1)}{2z^2}}{\frac{1}{2z}\left[1-e^{-2z}\right]} = \frac{(z-1)+e^{-2z}(z+1)}{1-e^{-2z}}. \tag{B.23}$$

For large values of z this may be approximated by

$$z\frac{\widetilde{m}_0'(z)}{m_0(z)} \approx z-1, \qquad z \geq 20. \tag{B.24}$$

The error of this approximation goes approximately as e^{-2z}.

B.3 Cubic Splines

This summary of the needed cubic splines follows that of the Thesis by Esler [2006].

B.3.1 Cubic Splines (1d)

In one dimension the basic idea of the cubic splines is to approximate a function $f(x)$ by piecewise cubic polynomials. For a discrete set of points x_i the cubic polynomials need to satisfy the following three requirements:

$$f(x_i) = y_i, \tag{B.25}$$
$$f'(x_i^-) = f'(x_i^+), \tag{B.26}$$
$$f''(x_i^-) = f''(x_i^+). \tag{B.27}$$

That is, we require the polynomials as well as their first and second derivatives to be continous at the connection points x_i.

One convenient expression for the interpolating cubic polynomial in an interval $x \in (x_i, x_{i+1}]$ is given as

$$S(x) = y_i p_1(t) + y_{i+1} p_2(t) + h_i \left[y_i' q_1(t) + y_{i+1}' q_2(t)\right], \tag{B.28}$$

where $h_i = x_{i+1} - x_i$, $t = \frac{x - x_i}{h_i}$ and

$$p_1(t) = (1 + 2t)(t - 1)^2, \tag{B.29}$$
$$p_2(t) = t^2(3 - 2t), \tag{B.30}$$
$$q_1(t) = t(t - 1)^2, \tag{B.31}$$
$$q_2(t) = t^2(t - 1), \tag{B.32}$$

are the so called Hermite basis functions. This approach is also called as cubic Hermite spline. It can be easily verified that $S(x)$ satisfies the first two requirement for the polynomials, Eqs. (B.25) and (B.26) — assuming we already know the first derivatives y'_i and y'_{i+1}. The still unknown values for the first derivatives can be solved from the third requirement, ie. Eq. (B.27),

$$S''(x_i^-) = S''(x_i^+). \tag{B.33}$$

Since

$$\begin{aligned} S''(x) &= y_i \frac{\mathrm{d}^2 p_1(t)}{\mathrm{d}x^2} + y_{i+1} \frac{\mathrm{d}^2 p_2(t)}{\mathrm{d}x^2} + h_i \left[y'_i \frac{\mathrm{d}^2 q_1(t)}{\mathrm{d}x^2} + y'_{i+1} \frac{\mathrm{d}^2 q_2(t)}{\mathrm{d}x^2} \right] \\ &= \frac{y_i}{h_i^2} \frac{\mathrm{d}^2 p_1(t)}{\mathrm{d}t^2} + \frac{y_{i+1}}{h_i^2} \frac{\mathrm{d}^2 p_2(t)}{\mathrm{d}t^2} + h_i \left[\frac{y'_i}{h_i^2} \frac{\mathrm{d}^2 q_1(t)}{\mathrm{d}t^2} + \frac{y'_{i+1}}{h_i^2} \frac{\mathrm{d}^2 q_2(t)}{\mathrm{d}t^2} \right], \end{aligned} \tag{B.34}$$

we get

$$\begin{aligned} S''(x_i^-) &= \frac{y_{i-1}}{h_{i-1}^2} \frac{\mathrm{d}^2 p_1(t^-)}{\mathrm{d}t^2} + \frac{y_i}{h_{i-1}^2} \frac{\mathrm{d}^2 p_2(t^-)}{\mathrm{d}t^2} + h_{i-1} \left[\frac{y'_{i-1}}{h_{i-1}^2} \frac{\mathrm{d}^2 q_1(t^-)}{\mathrm{d}t^2} + \frac{y'_i}{h_{i-1}^2} \frac{\mathrm{d}^2 q_2(t^-)}{\mathrm{d}t^2} \right] \\ &= \frac{1}{h_{i-1}^2} \left[6y_{i-1} - 6y_i + h_{i-1}(2y'_{i-1} + 4y'_i) \right] \end{aligned} \tag{B.35}$$

and

$$\begin{aligned} S''(x_i^+) &= \frac{y_i}{h_i^2} \frac{\mathrm{d}^2 p_1(t^+)}{\mathrm{d}t^2} + \frac{y_{i+1}}{h_i^2} \frac{\mathrm{d}^2 p_2(t^+)}{\mathrm{d}t^2} + h_i \left[\frac{y'_i}{h_i^2} \frac{\mathrm{d}^2 q_1(t^+)}{\mathrm{d}t^2} + \frac{y'_{i+1}}{h_i^2} \frac{\mathrm{d}^2 q_2(t^+)}{\mathrm{d}t^2} \right] \\ &= \frac{1}{h_i^2} \left[-6y_i + 6y_{i+1} + h_i(-4y'_i - 2y'_{i+1}) \right] \end{aligned} \tag{B.36}$$

Now, using the third requirement and rearranging terms a little we have

$$\begin{aligned} & S''(x_i^-) = S''(x_i^+) \\ \Leftrightarrow & \frac{1}{h_{i-1}^2} \left[6y_{i-1} - 6y_i + h_{i-1}(2y'_{i-1} + 4y'_i) \right] = \frac{1}{h_i^2} \left[-6y_i + 6y_{i+1} + h_i(-4y'_i - 2y'_{i+1}) \right] \\ \Leftrightarrow & 2h_i y'_{i-1} + 4(h_i + h_{i-1}) y'_i + 2h_{i-1} y'_{i+1} = d_i, \end{aligned} \tag{B.37}$$

where

$$d_i = 6\left(\frac{h_i}{h_{i-1}} - \frac{h_{i-1}}{h_i}\right) y_i - 6\frac{h_i}{h_{i-1}} y_{i-1} + 6\frac{h_{i-1}}{h_i} y_{i+1} \tag{B.38}$$

The expression above is valid for all $1 < i < N$ and gives us a tridiagonal set of equations.

$$\begin{pmatrix} - & - & - & - & - & \dots \\ 2h_2 & 4(h_2+h_1) & 2h_1 & 0 & 0 & \dots \\ 0 & 2h_3 & 4(h_3+h_2) & 2h_2 & 0 & \dots \\ \vdots & \vdots & \ddots & & & \\ - & - & - & - & - & \dots \end{pmatrix} \begin{pmatrix} - \\ y'_2 \\ y'_3 \\ \vdots \\ y'_{N-1} \\ - \end{pmatrix} = \begin{pmatrix} - \\ d_2 \\ d_3 \\ \vdots \\ d_{N-1} \\ - \end{pmatrix}$$

The equations for the $i = 1$ and $i = N$ depend on the boundary conditions. Thus, in order to use Eq. (B.28) for interpolation we must first define the boundary conditions, after which we can solve the matrix equation for the derivatives and interpolate.

B.3.2 Complete boundary conditions

For the complete boundary conditions one needs to specify the first derivatives for $i = 1$ and $i = N$, i.e. $y'_1 = d_1$ and $y'_N = d_N$, where d_1 and d_N are somehow known or approximated. Then the matrix equation is

$$\begin{pmatrix} 1 & 0 & 0 & 0 & 0 & \dots & 0 \\ 2h_2 & 4(h_2+h_1) & 2h_1 & 0 & 0 & \dots & 0 \\ 0 & 2h_3 & 4(h_3+h_2) & 2h_2 & 0 & \dots & 0 \\ \vdots & \vdots & \ddots & & & \vdots & \\ 0 & 0 & 0 & 0 & 0 & \dots & 1 \end{pmatrix} \begin{pmatrix} y'_1 \\ y'_2 \\ y'_3 \\ \vdots \\ y'_{N-1} \\ y'_N \end{pmatrix} = \begin{pmatrix} d_1 \\ d_2 \\ d_3 \\ \vdots \\ d_{N-1} \\ d_N \end{pmatrix}$$

B.3.3 Natural boundary conditions

If we do not know a proper approximation for the first derivatives we may construct the so-called natural splines, which assume that the second derivatives of the bound-

ary splines are zero. Then the matrix equation is

$$\begin{pmatrix} 1 & \frac{1}{2} & 0 & 0 & 0 & \dots & 0 & 0 \\ 2h_2 & 4(h_2+h_1) & 2h_1 & 0 & 0 & \dots & 0 & 0 \\ 0 & 2h_3 & 4(h_3+h_2) & 2h_2 & 0 & \dots & 0 & 0 \\ \vdots & \vdots & \ddots & & & \vdots & & \\ 0 & 0 & 0 & 0 & 0 & \dots & \frac{1}{2} & 1 \end{pmatrix} \begin{pmatrix} y'_1 \\ y'_2 \\ y'_3 \\ \vdots \\ y'_{N-1} \\ y'_N \end{pmatrix} = \begin{pmatrix} d_1 \\ d_2 \\ d_3 \\ \vdots \\ d_{N-1} \\ d_N \end{pmatrix},$$

with

$$d_1 = \frac{3}{2}\frac{y_2 - y_1}{h_1}$$

and

$$d_N = \frac{3}{2}\frac{y_N - y_{N-1}}{h_{N-1}}.$$

(B.39)

B.3.4 Bicubic Splines

Extension of the above described cubic splines to two dimensions is relatively straightforward. Now, the function to be interpolated is $f(x, y)$, and thus, the values $f(x_i, y_j) = f_{ij}$ and its derivatives need to be stored in two dimensional grids. Instead of only one derivative, as in one dimension, we now have derivatives with respect to both x and y, and also the cross-derivative that are needed. Thus, for the bicubic splines we need at each grid point the values for

$$f_{ij} = f(x_i, y_j) \tag{B.40}$$

$$f^x_{ij} = \frac{\partial f(x_i, y_j)}{\partial x} \tag{B.41}$$

$$f^y_{ij} = \frac{\partial f(x_i, y_j)}{\partial y} \tag{B.42}$$

$$f^{xy}_{ij} = \frac{\partial^2 f(x_i, y_j)}{\partial x \partial y}. \tag{B.43}$$

The interpolated value is then obtained from

$$S(x,y) = \begin{pmatrix} p_1(u) \\ p_2(u) \\ hq_1(u) \\ hq_2(u) \end{pmatrix}^T \begin{pmatrix} f_{i,j} & f_{i,j+1} & f^y_{i,j} & f^y_{i,j+1} \\ f_{i+1,j} & f_{i+1,j+1} & f^y_{i+1,j} & f^y_{i+1,j+1} \\ f^x_{i,j} & f^x_{i,j+1} & f^{xy}_{i,j} & f^{xy}_{i,j+1} \\ f^x_{i+1,j} & f^x_{i+1,j+1} & f^{xy}_{i+1,j} & f^{xy}_{i+1,j+1} \end{pmatrix} \begin{pmatrix} p_1(v) \\ p_2(v) \\ lq_1(v) \\ lq_2(v) \end{pmatrix},$$

(B.44)

where

$$h = x_{i+1} - x_i$$
$$l = y_{j+1} - y_j$$
$$u = \frac{x - x_i}{h}$$
$$v = \frac{y - y_j}{l}$$

for $x_i \leq x < x_{i+1}$ and $y_j \leq y < y_{j+1}$.

The derivatives required here are easily obtained using the same matrix equations as for the one dimensional case. For f^x_{ij} solve the matrix equation for each column of f_{ij}, for f^x_{ij} do the same for each row of f_{ij} and for the cross-derivative go through each row of f^x_{ij}, for example.

B.4 Squaring grid

Using a special kind of grid for the squaring can easily speed up the process and also give more accuracy. The algorithm for the grid we have been using is given here:

$$r_i = r_{i-1} + \left(1 - \frac{1}{e^{f_i} + 1}\right) \Delta r, \tag{B.45}$$

where Δr is the maximum spacing and f_i is evenly spaced between $-a$ and a using the number of grid points (N) as a divider, i.e. $f_{i+1} - f_i = 2a/N$.

Commonly we use $r_0 = 10^{-4} a_0$, $\Delta r = 0.2 a_0$ and $a = 10$. Thus, with 60×60 grid points the largest distance with the above parameters is about $6a_0$. 100×100 grid is found very accurate, for which the largest tabulated distance is about $10a_0$. For accurate matrix squaring values outside the grid are also needed — depending on the final time step τ. With the above parameters the grid shown here is good for relatively small time steps, $\tau < 10 E_h^{-1}$. For larger time steps larger distances are needed and the parameters of the grid should be adjusted.

References

S. A. Alexander and R. L. Coldwell. Spectroscopic constans of H_2^+ using Monte Carlo methods. *Chem. Phys. Lett.* 413, 253 (2005).

J. B. Anderson. Quantum chemistry by random walk. H ^{2}P, H_3^+ D_{3h} $^1A_1$, H_2 $^3\sigma_u^+$, H_4 $^1\sigma_g^+$, Be ^{1}S. *J. Chem. Phys.* 65, 4121 (1976).

E. J. Baerends and O. V. Gritsenko. A quantum chemical view of density functional theory. *J. Phys. Chem. A* 101, 5383 (1997).

D. H. Bailey and A. M. Frolov. Positron annihilation in the dipositronium Ps_2. *Phys. Rev. A* 72, 014501 (2005).

D. Bressanini, M. Mella and G. Morosi. Stability of four–unit–charge systems: A quantum Monte Carlo study. *Phys. Rev. A* 55, 200 (1997).

S. Bubin and L. Adamowicz. Nonrelativistic variational calculations of the positronium molecule and the positronium hydride. *Phys. Rev. A* 74, 052502 (2006).

M. A. Buijse and E. J. Baerends. An approximate exchange-correlation hole density as functional of the natural orbitals. *Mol. Phys.* 100, 401 (2002).

M. A. Buijse and E. J. Baerends. *Density Functional Theory of Molecules, Clusters, and Solids, pages 1-46*. Ed. D. E. Ellis, Kluwer Academic Publishers, Printed in the Netherlands (1995).

A. Bürgers, D. Wintgen and J.-M. Rest. Highly doubly excited S states of the helium atom. *J. Phys. B* 28, 3163 (1995).

D. B. Cassidy and A. P. Mills Jr. Interactions between positronium atoms in porous silica. *Phys. Rev. Lett.* 100, 013401 (2008).

D. B. Cassidy and A. P. Mills Jr. The production of molecular positronium. *Nature* 449, 195 (2007).

D. Ceperley. The simulation of quantum systems with random walks: A new algorithm for charged systems. *J. Comp. Phys.* 51, 404 (1983).

D. M. Ceperley. Fermion nodes. *J. Stat. Phys.* 63, 1237 (1991).

D. M. Ceperley. Path integrals in the theory of condensed helium. *Rev. Mod. Phys.* 67, 279 (1995).

D. M. Ceperley. *Path Integral Monte Carlo Methods for Fermions*. Ed. K. Binder and G. Ciccotti, Editrice Compositori, Bologna, Italy (1996).

C. Chakravarty, M. C. Gordillo and D. M. Ceperley. A comparision of the efficiency of fourier- and discrete time-path integral Monte Carlo. *J. Chem. Phys.* 109, 2123 (1998).

A. Dal Corso, A. Pasquarello and A. Baldereschi. Generalized-gradient approximations to density-functional theory: A comparative study for atoms and solids. *Phys. Rev. B* 53, 1180 (1996).

H. DeRaedt and B. DeRaedt. Applications of generalized trotter formula. *Phys. Rev. A* 28, 3575 (1983).

R. Egger, L. Mühlbacher and C. H. Mak. Path-integral Monte Carlo simulations without the sign problem: Multilevel blocking approach for effective actions. *Phys. Rev. E* 61, 5961 (2000).

M. Emami-Razavi. Relativistic n-fermion wave equations in quantum electrodynamics. *Phys. Rev. A* 77, 042104 (2008).

K. Esler. *Advancement in the path integral Monte Carlo method for many-body quantum systems at finite temperature*. Ph.D. thesis, University of Illinois at Urbana-Champaign (2006).

R. P. Feynman. *Statistical Mechanics*. Perseus Books, Reading, MA (1972, 1998).

R. P. Feynman and A. R. Hibbs. *Quantum Mechanics and Path Integrals*. New York: McGraw-Hill (1965).

A. M. Frolov, S. I. Kryuchkov and V. H. Smith. (e^-,e^+)-pair annihilation in the positronium molecule Ps_2. *Phys. Rev. A* 51, 4514 (1995).

J. L. Gottfried, B. J. McCall and T. Oka. Near-infrared spectroscopy of H_3^+ above the barrier to linearity. *J. Chem. Phys.* 118, 10890 (2003).

G. F. Gribakin, J. A. Young and C. M. Surko. Positron-molecule interactions: Resonant attachment, annihilation, and bound states. *Rev. Mod. Phys.* 82, 2557 (2010).

G. J. Harris, A. E. Lynas-Gray, S. Miller and J. Tennyson. The effect of the electron donor H_3^+ on the pre–main-sequence and main-sequence evolution of low-mass, zero-metallicity stars. *Astrophys. J.* 600, 1025 (2004).

M. F. Herman, E. J. Bruskin and B. J. Berne. On path integral Monte Carlo simulations. *J. Chem. Phys.* 76, 5150 (1982).

L. Hostler and R. H. Pratt. Coulomb Green's function in closed form. *Phys. Rev. Lett.* 10, 469 (1963).

E. A. Hylleraas and A. Ore. Binding energy of the positronium molecule. *Phys. Rev.* 71, 493 (1947).

M. H. Kalos and P. A. Whitlock. *Monte Carlo Methods, Second, Revised and Enlarged Edition*. Wiley-VCH, Weinheim (2008).

M. H. Kalos and P. A. Whitlock. *Monte Carlo Methods, Volume I: Basics*. Wiley, New York (1986).

D. B. Kinghorn and R. D. Poshusta. Nonadiabatic variational calculations on dipositronium using explicitly correlated gaussian basis functions. *Phys. Rev. A* 47, 3671 (1993).

H. Kleinert. *Path Integrals in Quantum Mechanics, Statistics, Polymer Physics, and Financial Markets*. World Scientific Publishing Co. Pte. Ltd, Singapore (2004). 3rd Edition.

A. D. Klemm and R. G. Storer. The structure of quantum fluids: Helium and Neon. *Aust. J. Phys.* 26, 43 (1973).

T. T. Koskinen, A. D. Aylward and S. Miller. The upper atmosphere of HD17156b. *Astrophys. J.* 693, 868 (2009).

T. T. Koskinen, R. V. Yelle, P. Lavvas and N. K. Lewis. Characterizing the thermosphere of HD209458b with uv transit observations. *Astrophys. J.* 723, 116 (2010).

H. Kreckel, D. Bing, S. Reinhardt, A. Petrignani, M. Berg, and A. Wolf. Chemical probing spectroscopy of H_3^+ above the barrier to linearity. *J. Chem. Phys.* 129, 164312 (2008).

W. Kutzelnigg and R. Jaquet. Explicitly correlated potential energy surface of H_3^+ including relativistic and adiabatic corrections. *Phil. Trans. R. Soc. A* 364, 2855 (2006).

I. Kylänpää. Application of the path integral Monte Carlo method for solving the quantum statistics of electron–proton systems. Master's thesis, Tampere University of Technology (2006).

I. Kylänpää, M. Leino and T. T. Rantala. Hydrogen molecule ion: Path integral Monte Carlo approach. *Phys. Rev. A* 76, 052508 (2007).

I. Kylänpää and T. T. Rantala. Thermal dissociation of dipositronium: Path-integral Monte Carlo approach. *Phys. Rev. A* 80, 024504 (2009).

I. Kylänpää and T. T. Rantala. Finite temperature quantum statistics of H_3^+ molecular ion. *J. Chem. Phys.* 133, 044312 (2010).

I. Kylänpää and T. T. Rantala. First-principles simulation of molecular dissociation–recombination equilibrium *J. Chem. Phys.* 135, 104310 (2011).

G. Laricchia, M. Charlton, C. D. Beling and T. C. Griffith. Density dependence of positron annihilation and positronium formation in H_2 gas at temperatures between 77 and 297 K. *J. Phys. B* 20, 1865 (1987).

M. Leino. *Finite-Temperature Quantum Statistics of a Few Confined Electrons and Atoms — Path-Integral Approach.* Ph.D. thesis, Tampere University of Technology (2007).

X.-P. Li and J. Q. Broughton. High-order correction to the Trotter expansion for use in computer simulation. *J. Chem. Phys* 86, 5094 (1987).

M. B. Lystrup, S. Miller, N. Dello Russo, Jr. R. J. Vervack and T. Stallard. First vertical ion density profile in Jupiter's auroral atmosphere: Direct observations using the Keck II telescope. *Astrophys. J.*, 677, 790 (2008).

A. P. Lyubartsev and P. N. Vorontsov-Velyaminov. Path-integral Monte Carlo method in quantum statistics for a system of n identical fermions. *Phys. Rev. A* 48, 4075 (1993).

A. P. Lyubartsev. Simulation of excited states and the sign problem in path integral Monte Carlo method. *J. Phys. A: Math. Gen.* 38, 6659 (2005).

C. H. Mak, R. Egger and H. Weber-Gottschick. Multilevel Blocking Approach to the Fermion Sign Problem in Path-Integral Monte Carlo Simulations. *Phys. Rev. Lett.* 81, 4533 (1998).

R. D. Mattuck. *A Guide to Feynman Diagrams in the Many-Body Problem*. Dover (1992).

D. K. McKenzie and G. W. F. Drake. Variational calculation for the ground state of lithium and QED corrections for Li-like ions. *Phys. Rev. A* 44, R6973 (1991).

J. D. McNutt, S. C. Sharma and R. D. Brisbon. Positron annihilation in gaseous hydrogen and hydrogen-neon mixtures. I. Low-energy positrons. *Phys. Rev. A* 20, 347 (1979).

N. Metropolis, A. W. Rosenbluth, M. N. Rosenbluth, A .H. Teller and E. Teller. Equation of state calculations by fast computing machines. *J. Chem. Phys.* 21, 1087 (1953).

B. Militzer and D. M. Ceperley. Path integral Monte Carlo simulation of the low-density hydrogen plasma. *Phys. Rev. E* 63, 066404 (2001).

J. Mitroy. Expectation values of the e^+Li system. *Phys. Rev. A* 70, 024502 (2004).

J. Mitroy. Determination and applications of enhancement factors for positron and ortho-positronium annihilations. *Phys. Rev. A* 72, 062707 (2005).

L. Neale and J. Tennyson. A high-temperature partition function for H_3^+. *Astrophys. J.* 454, L169 (1995).

T. Oka. Observation of the infrared spectrum of H_3^+. *Phys. Rev. Lett.* 45, 531 (1980).

T. Oka. The infrared spectrum of H_3^+ in laboratory and space plasmas. *Rev. Mod. Phys.* 64, 1141 (1992).

R. G. Parr and W. Yang. *Density-Functional Theory of Atoms and Molecules*. Oxford (1989).

M. Pavanello and L. Adamowicz. High-accuracy calculations of the ground, $1\ ^1A_1'$, and the $2\ ^1A_1'$, $2\ ^3A_1'$, and $1\ ^1E'$ excited states of H_3^+. *J. Chem. Phys.* 130, 034104 (2009).

E. L. Pollock. Properties and computation of the coulomb pair density matrix. *Comp. Phys. Commun.* 52, 49 (1988).

E. L. Pollock and D. M. Ceperley. Path-integral computation of superfluid densities. *Phys. Rev. B* 36, 8343 (1987).

R. D. Poshusta and D. B. Kinghorn. Density matrices for correlated gaussians: Helium and Dipositronium. *Int. J. Quantum Chem.* 60, 213 (1996).

R. Röhse, W. Kutzelnigg, R. Jaquet and W. Klopper. Potential energy surface of the H_3^+ ground state in the neighborhood of the minimum with microhartree accuracy and vibrational frequencies derived from it. *J. Chem. Phys.* 101, 2231 (1994).

C. E. Scheu, D. B. Kinghorn and L. Adamowicz. Non-Born–Oppenheimer calculations on the LiH molecule with explicitly correlated Gaussian functions. *J. Chem. Phys.* 114, 3393 (2001).

D. M. Schrader. Symmetry of dipositronium Ps_2. *Phys. Rev. Lett.* 92, 043401 (2004).

L. S. Schulman. *Techniques and Applications of Path Integration*. Dover (2005).

M. Stanke, D. Kedziera, S. Bubin and L. Adamowicz. Lowest Excitation Energy of ^{9}Be. *Phys. Rev. Lett.* 99, 043001 (2007).

R. G. Storer. Path-integral calculation of the quantum-statistical density matrix for attractive coulomb froces. *J. Math. Phys.* 9, 964 (1968).

M. Suzuki. Generalized Trotter's formula and systematic approximants of exponential operators and inner derivations with applications to many-body problems. *Comm. Math. Phys.* 51, 183 (1976).

J. J. Thomson. Rays of positive electricity. *Phil. Mag.* 21, 225 (1911).

H. F. Trotter. On the product of semi-groups of operators. *Proc. Am. Math. Soc.* 10, 545 (1959).

J. Usukura and Y. Suzuki. Resonances of positronium complexes. *Phys. Rev. A* 66, 010502 (1998).

J. Usukura, K. Varga and Y. Suzuki. Signature of the existence of the positronium molecule. *Phys. Rev. A* 58, 1918 (1998).

G. L. Wright, M. Charlton, G. Clark, T. C. Griffith and G. R. Heyland. Positron lifetime parameters in H_2, CO_2 and CH_4. *J. Phys. B* 16, 4065 (1983).

Paper I

I. Kylänpää, M. Leino and T. T. Rantala
Hydrogen molecule ion: Path integral Monte Carlo approach

Reprinted with permission from:
Physical Review A 76, 052508 (2007)

Hydrogen molecule ion: Path-integral Monte Carlo approach

I. Kylänpää, M. Leino, and T. T. Rantala
Institute of Physics, Tampere University of Technology, P.O. Box 692, FI-33101 Tampere, Finland
(Received 17 August 2007; published 15 November 2007)

The path-integral Monte Carlo approach is used to study the coupled quantum dynamics of the electron and nuclei in hydrogen molecule ion. The coupling effects are demonstrated by comparing differences in adiabatic Born-Oppenheimer and nonadiabatic simulations, and inspecting projections of the full three-body dynamics onto the adiabatic Born-Oppenheimer approximation. Coupling of the electron and nuclear quantum dynamics is clearly seen. The nuclear pair correlation function is found to broaden by $0.040a_0$, and the average bond length is larger by $0.056a_0$. Also, a nonadiabatic correction to the binding energy is found. The electronic distribution is affected less than the nuclear one upon inclusion of nonadiabatic effects.

DOI: 10.1103/PhysRevA.76.052508 PACS number(s): 31.15.Kb, 31.50.Gh

I. INTRODUCTION

There are a number of phenomena in molecular and chemical physics which are influenced by the quantum behavior of both nuclei and electrons, rovibrational dynamics being a good example; see Refs. [1–3] and references therein. In case of light-mass nuclei, protons in particular, treatment of the quantum nature of the nuclei is essential [4–6]. This has proven to be important in a description of the hydrogen bond, for example [7].

The hydrogen molecule ion (H_2^+), being the simplest molecule, has been studied extensively [8], and it has often been used as an example or a test case for an improved method or accuracy [9–14]. In addition to the free molecule, H_2^+ influenced by an electric or magnetic field is a well studied subject [15–21]. Furthermore, there is interest in descriptions that are not restricted to Born-Oppenheimer (BO) or other adiabatic approximations [22–28]. Such extensions can be easily realized by using quantum Monte Carlo (QMC) methods [29,30], for example.

Among the QMC methods the path-integral MC (PIMC) formalism offers a finite-temperature approach together with a transparent tool to trace the correlations between the particles involved. Though computationally extremely demanding, with some approximations it is capable of treating low-dimensional systems, such as small molecules or clusters accurately enough. Some examples found in the literature are H [31], HD^+, and H_3^+ [32] and H_2 clusters [33–37] with special attention laid on ^{4}He [38–42]. The approximations in these approaches relate to *ad hoc*–type potentials describing the interactions between particles.

In this work we evaluate the density matrix of the full three-body quantum dynamics in a stationary state and finite temperature. This is what we call "all-quantum" (AQ) simulations. Second, the electronic part only is evaluated as a function of internuclear distance in the spirit of the BO approximation, and third, the adiabatic nuclear dynamics is evaluated in the BO potential curve. These allow us to demonstrate the nonadiabatic electron-nuclei coupling by a projection of the AQ dynamics onto the adiabatic approximations.

We need to approximate the $-1/r$ Coulomb potential of electron-nucleus interactions at short range to make the calculations feasible. We realize this with a carefully tested pseudopotential (PP). Also, the absent (ortho) or negligible (para) exchange interaction of nuclei is not taken into account. Finally, we want to emphasize that our purpose is to simulate a finite-temperature mixed state including correlations exactly, which is a challenging task for other methods. However, if high-accuracy zero-kelvin computations are preferred, one should turn to other methods such as the variational Monte Carlo (VMC) method, for example. For convenience, we have chosen 300 K, which essentially, but not exactly, restricts the system to its electronic ground state.

We begin with a brief introduction to the theory and methods in the next section. This includes a description of the PP and tools and concepts for the analysis in the following section. Then we carry on to the results. Throughout the paper atomic units are used: hartrees (E_H) for energies and Bohr radius (a_0) for distances.

II. THEORY AND METHODS

For a quantum many-body system in thermal equilibrium the partition function contains all the information of the system [43]. The local thermodynamical properties, however, are included in the density matrix from which all the properties of the quantum system may be derived [44]. The nonadiabatic effects are directly taken into account in the PIMC approach. In addition, finite-temperature and correlation effects are exactly included.

A. Path-integral Monte Carlo approach

According to the Feynman formulation of statistical quantum mechanics [45] the partition function for interacting distinguishable particles is given by the trace of the density matrix,

$$Z = \mathrm{Tr}\hat{\rho}(\beta) = \lim_{M\to\infty} \int dR_0\, dR_1\, dR_2 \cdots dR_{M-1} \prod_{i=0}^{M-1} e^{-S(R_i,R_{i+1};\tau)}, \tag{1}$$

where $\hat{\rho}(\beta)=e^{-\beta\hat{H}}$, S is the action, $\beta=1/k_BT$, $\tau=\beta/M$, and $R_M=R_0$. M is called the Trotter number, and it characterizes the accuracy of the discretized path. In the limit $M\to\infty$ we

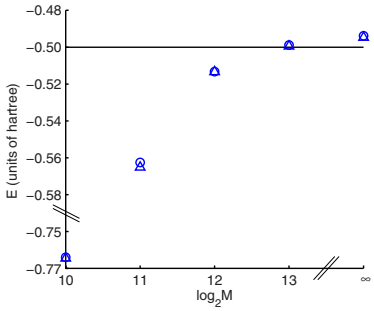

FIG. 1. (Color online) Hydrogen atom total energies with different Trotter numbers: infinite nuclear mass (triangles) and AQ (circles). Extrapolated ground-state energies are $-0.4947(1)E_H$ and $-0.4938(3)E_H$ for infinite nuclear mass and AQ simulations, respectively.

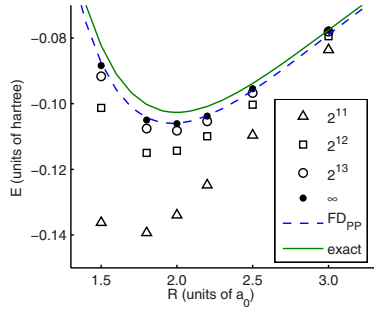

FIG. 2. (Color online) H_2^+ potential curves with different Trotter numbers $M=2^{11}$ (squares), $M=2^{12}$ (triangles), $M=2^{13}$ (circles), extrapolated values (dots), and finite-difference calculations with the pseudopotential (dashed line) and with exact e^--p^+ potential (solid line).

are ensured to get the correct partition function Z, but in practice sufficient convergence at some finite M is found, depending on the steepness of the Hamiltonian $\hat{H}$.

In the primitive approximation scheme of the PIMC formalism the action is written as [46]

$$S(R_i,R_{i+1};\tau)=\frac{3N}{2}\ln(4\pi\lambda\tau)+\frac{(R_i-R_{i+1})^2}{4\lambda\tau}+U(R_i,R_{i+1};\tau), \tag{2}$$

where $U(R_i,R_{i+1};\tau)=\frac{\tau}{2}[V(R_i)+V(R_{i+1})]$ and $\lambda=\hbar^2/2m$.

Sampling of the configuration space is carried out using the Metropolis procedure [47] with the bisection moves [48]. This way the kinetic part of the action is sampled exactly and only the interaction part is needed in the Metropolis algorithm. The level of the bisection sampling ranges from 3 to 6 in our simulations, respectively with the increase in the Trotter number. The bisection sampling turns out to be essential with large Trotter numbers to achieve feasible convergence, for nuclei in particular. Total energy is calculated using the virial estimator [49].

B. Extrapolation of expectation values

The Trotter scaling procedure [32] for expectation values is used to obtain estimates for energetics in the limit $M\to\infty$. To use this procedure one needs expectation values with several different Trotter numbers. For the Trotter number M the scaling scheme is

$$\langle\hat{A}\rangle_\infty=\langle\hat{A}\rangle_M+\sum_{i=1}^{N}\frac{c_{2i}}{M^{2i}}, \tag{3}$$

where coefficients c_{2i} are constants for a given temperature and N represents the order of extrapolation. In this paper $N=2$ has been used for the energies of H_2^+, and $N=3$ for hydrogen atom energies; see Figs. 1 and 2.

C. Pseudopotential of the electron

For the hydrogen molecule ion the potential energy is

$$V(\mathbf{r}_1,\mathbf{r}_2,\mathbf{R})=-\frac{1}{r_1}-\frac{1}{r_2}+\frac{1}{R}, \tag{4}$$

where $r_i=|\mathbf{r}-\mathbf{R}_i|$ and $R=|\mathbf{R}_1-\mathbf{R}_2|$, $\mathbf{r}$ being the coordinates of the electron and R the internuclear distance. Equation (4) sets challenges for the PIMC approach arising from the singularity of the attractive Coulomb interaction [50,51], which in this work is replaced by a PP of the form [52]

$$V_{\mathrm{PP}}(r)=-\frac{\mathrm{erf}(\alpha_c r)}{r}+(a+br^2)e^{-\alpha r^2}. \tag{5}$$

The parametres $\alpha_c=3.8638$, $\alpha=7.8857$, $a=1.6617$, and $b=-18.2913$ were fitted using direct numerical solution to give the exact ground-state energy of hydrogen atoms and the wave function accurately outside a cutoff radius of about $0.6a_0$. Also, a number of lowest-energy orbitals of the hydrogen atom are obtained accurately outside the same cutoff radius [53]. Because the bond length of H_2^+ is about $2a_0$, it is expected that bonding of the hydrogen molecule ion becomes properly described.

Hydrogen atom reference energies for different Trotter numbers are shown in Fig. 1, where triangles are obtained from infinite nuclear mass and circles are from AQ simulations. Extrapolated ground-state values are $-0.4947(1)E_H$ and $-0.4938(3)E_H$ for infinite nuclear mass and AQ simulations, respectively, statistical standard error of mean (SEM) given as the uncertainty in parentheses. We can note that within the 2SEM limits the proportion of these energies 0.9982 reproduces that of the Rydberg constants, $R_H/R_\infty=0.9995$.

D. Spectroscopic constants

Within the BO approximation of diatomic molecules the corrections to electronic energies due to rovibrational motion of the nuclei can be evaluated from a Dunham polynomial [54]

$$E_{vJ} = -D_e + \omega_e\left(v+\frac{1}{2}\right) - \omega_e x_e\left(v+\frac{1}{2}\right)^2 + B_e J(J+1) - \alpha_e J(J+1)\left(v+\frac{1}{2}\right) + \cdots, \quad (6)$$

where v and J are vibrational and rotational quantum numbers, respectively, and B_e, ω_e, $\omega_e x_e$, and α_e are the spectroscopic constants.

The spectroscopic constants of H_2^+ and D_2^+ are obtained as introduced in Ref. [54]. In atomic units,

$$B_e = \frac{1}{2I} = \frac{1}{2\mu R^2}, \quad (7)$$

$$\omega_e = \left(\frac{1}{\mu}\frac{d^2E}{dR^2}\right)^{1/2}, \quad (8)$$

$$\omega_e x_e = \frac{1}{48\mu}\left[5\left(\frac{d^3E/dR^3}{d^2E/dR^2}\right)^2 - 3\frac{d^4E/dR^4}{d^2E/dR^2}\right], \quad (9)$$

$$\alpha_e = -\frac{6B_e^2}{\omega_e}\left[\frac{R}{3}\frac{d^3E/dR^3}{d^2E/dR^2} + 1\right]. \quad (10)$$

Instead of determining these constants at the equilibrium distance only, as in Ref. [54], we evaluate expectation values from the distribution of nuclei, e.g., for the rotational constant

$$B_e = \frac{1}{2\mu}\int g(R)\frac{1}{R^2}dR, \quad (11)$$

where the pair correlation function $g(R)$ is normalized to unity. The other constants, Eqs. (8)–(10), are evaluated similarly.

E. Centrifugal distortion

The effects caused by the centrifugal distortion, arising from rotational motion of the nuclei, on the equilibrium distance can be assessed by inspecting the extremum values of the energy of the harmonic oscillator in rotational motion: $E_J(r) = \frac{1}{2}k(r-r_e)^2 + J(J+1)/2\mu r^2$. We find an approximate equation

$$\Delta R = \frac{4B_e}{\mu\omega_e^2 R_e^2}J(J+1), \quad (12)$$

where R_e is the equilibrium distance. Equation (12), however, does not include the anharmonic effects shown in Eq. (6), which evidently increase the bond length.

At finite temperature the rotational energy states should be weighted by the Boltzmann factor, which leads to

$$\Delta R = \frac{4B_e}{\mu\omega_e^2 R_e^2}\frac{\sum_J J(J+1)\exp[-\beta B_e J(J+1)]}{\sum_J \exp[-\beta B_e J(J+1)]}, \quad (13)$$

where $J = 0, 1, 2, \ldots$. Using the spectroscopic constants from Ref. [54] (see Table I) and temperature of 300 K we obtain $\Delta R = 0.0043a_0$. This approximation will be compared to our direct evaluation, below.

TABLE I. Expectation values of spectroscopic constants, Eqs. (7)–(11). A Morse potential [55] fitted to the FD_{PP} potential curve is used in the evaluation of the energy derivatives. Corresponding pair correlation functions are shown in Fig. 3. The first two columns are adiabatic nuclear dynamics results, and AQ results are in the last column.

	H_2^+ (hartree)	H_2^+ (cm^{-1})	D_2^+ (cm^{-1})	H_2^+ (AQ) (cm^{-1})	
B_e	0.0001366	30.35	15.24	29.26	This work
	0.0001344	29.85705			Ref. [54]
ω_e	0.0104816	2328.96	1668.25	2229.77	This work
	0.0104201	2315.3		(2232)[a]	Ref. [54]
$\omega_e x_e$	0.0003552	78.92	35.33	90.73	This work
	0.0003029	67.3			Ref. [54]
α_e	6.445×10^{-6}	1.432	0.45	1.636	This work
	7.201×10^{-6}	1.600			Ref. [54]

[a]MCDFT, nonadiabatic [28].

III. RESULTS

We consider three different cases separately in order to demonstrate the nonadiabatic effects. First, the electronic part only is evaluated as a function of internuclear distance in the spirit of the BO approximation. Second, the adiabatic nuclear dynamics is evaluated in the BO potential curve. Finally, H_2^+ is treated fully nonadiabatically with the AQ simulation. These allow us to demonstrate the nonadiabatic electron-nuclei coupling by a projection of the AQ dynamics onto the adiabatic approximations. In addition, spectroscopic constants and isotope effects are looked into.

A. Adiabatic electron dynamics

Though the PP, Eq. (5), reproduces the hydrogen atom energy exactly, an error of $-0.00342E_H$ from the exact value $-0.10263E_H$ results in the binding of another proton to the form H_2^+. This is demonstrated in Fig. 2, where potential curves of H_2^+ from finite-difference calculations with V_{PP} from Eq. (5) and exact $V(r) = -r^{-1}$ are shown.

Our PIMC energies with increasing Trotter number M and the extrapolation to $M=\infty$ using Eq. (3) are shown in the same figure. These indicate clearly that the Trotter number has to be at least 2^{13} in order to find the minimum of the potential curve at the nuclear separation $R = 2.0a_0$. The extrapolated values are in good agreement with the potential curve FD_{PP}, and there is almost a perfect match at $R = 2.0a_0$, where the value of the extrapolated dissociation energy is $0.1061(2)E_H$.

For larger nuclear separations than $3.5a_0$, however, we are not able to reproduce the potential curve with these Trotter numbers: we get a too weakly binding molecule. This is assumed to be a consequence of the electronic wave function becoming more delocalized as the internuclear distance in-

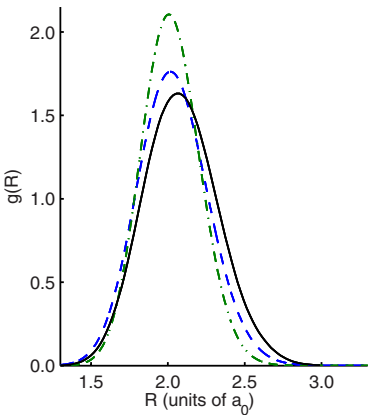

FIG. 3. (Color online) Nuclear pair correlation functions: H_2^+ AQ (solid line), H_2^+ QN (dashed line), and D_2^+ QN (dash-dotted line). The difference in the average nuclear separation between QN and AQ H_2^+ is $0.056(3)a_0$.

creases, and thus the "polymer ring" representing the electron is not capable of sufficient sampling of configuration space. This error should diminish with increasing M.

The electron-nucleus pair correlation function is shown in Fig. 4 and will be discussed below.

B. Adiabatic nuclear dynamics

For the quantum dynamics of the nuclei only (QN) we consider both H_2^+ and D_2^+ to see the isotope effect, too. The FD_{PP} potential curve in Fig. 2 is used, for which convergence with respect to Trotter number is found at $M \geqslant 2^6$ for both isotopes. The resulting pair correlation functions are shown in Fig. 3.

An average nuclear separation of $2.019(1)a_0$ for H_2^+ and $2.007(2)a_0$ for the isotope D_2^+ is found with $M \geqslant 2^6$. The full widths at half maximum (FWHM) of the pair correlation functions are $0.539(1)a_0$ and $0.454(1)a_0$ for these isotopes, respectively.

The difference in the bond length of H_2^+ between the adiabatic electron and adiabatic nuclei simulations—i.e., total distortion—is $0.019a_0$. The centrifugal contribution to this, the difference between one- and three-dimensional (1D and 3D) simulations of the nuclei, is $0.009(1)a_0$, which unexpectedly is about twice as much as the value $0.0043a_0$ evaluated from the approximate equation (13). The anharmonic contribution—i.e., difference between total and centrifugal distortions—is $0.010(1)a_0$. In Ref. [56] it was shown that anharmonic effects in H_2 molecules contribute about the same amount to total distortion as centrifugal force, which turns out to be the case here, too.

The difference between the total energies of the previous simulations (3D vs 1D) is $0.0009383(2)E_H$, which is close to $k_BT \approx 0.00095E_H$ as expected due to the presence of the two rotational degrees of freedom in 3D. The difference between the dissociation energies of adiabatic electron and nuclear simulations—i.e., the zero-point vibrational energy—is $0.0064(2)E_H$.

TABLE II. H_2^+ energetics (atomic units). The first three rows are BO and the next three are nonadiabatic values. For high-accuracy energetics see, for example, Ref. [14].

Method	E_{tot}	D_e	D_0^0	R
HF[a]	−0.6026	0.1026		2.000
VMC[b]	−0.6026	0.1026		2.000
PIMC[e]	−0.6061(2)	0.1061(2)	0.0997(1)	2.0
VMC[c]	−0.5971		0.0971	2.064
MCDFT[d]	−0.581		0.081	2.08
PIMC[e]	−0.59872(3)		0.09872(3)	2.075(2)

[a]Hartree-Fock [58].
[b]VMC, Born-Oppenheimer [54].
[c]VMC, nonadiabatic [30].
[d]MCDFT, nonadiabatic (SAO) [28].
[e]This work.

A Morse potential [55] fitted to the FD_{PP} potential curve is used in the evaluation of the spectroscopic constants; see Table I. This is justified because the nuclear simulations and analytical Morse wave function [57] calculations coincide. The spectroscopic constants of H_2^+ are close to those given in Ref. [54], which have been determined at the equilibrium distance of the nuclei, only. The same procedure is used for the spectroscopic constants of the other isotope. In Table I the same constants evaluated using the AQ instead of BO nuclear pair correlation function are also shown.

C. Nonadiabatic "all-quantum" dynamics

For H_2^+ the total energy of the AQ simulation with the Trotter number $M=2^{13}$ is $-0.60159(3)E_H$. The extrapolation procedure yields total energy $-0.59872(3)E_H$, which is only $0.0016E_H$ more binding than the value $-0.5971E_H$ from VMC simulations [30]. The zero-point energy obtained from simulations is $D_e - D_0^0 = 0.0074E_H$; see Table II. It should be pointed out that the error due to the pseudopotential in the AQ total energy is only about half of that found for the BO total energies.

The difference in dissociation energies of AQ and the 3D QN H_2^+ simulations is $0.00097E_H$, which is about k_BT, revealing additional electronic energy degrees of freedom in the first. AQ simulation for H_2^+ gives for the average nuclear separation $R=2.075(2)a_0$, which is $0.056a_0$ larger than that in the QN simulation. The AQ FWHM of the nuclear pair correlation function is $0.5785(2)a_0$, which shows a spreading of $0.040a_0$ compared to the QN results; see Fig. 3. With the Trotter number $M=2^{13}$ we find the AQ nuclear pair correlation function sufficiently converged.

In Fig. 4, BO and AQ electron-nucleus pair correlation functions are compared. AQ projection onto the BO bond length, $R=2.0a_0$, and BO results coincide, which indicates that the adiabatic BO approach for the electron dynamics is sufficient. Thus, it seems that the electron-nuclei coupling

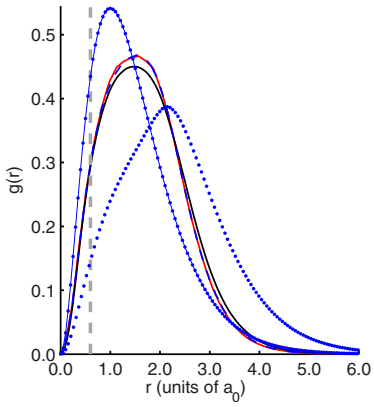

FIG. 4. (Color online) H_2^+ electron-nucleus pair correlation functions: AQ (solid line, second lowest curve), AQ projection to $R \approx 2.0a_0$ (solid line), and BO at $R=2.0a_0$ (dashed line). The latter two almost coincide. The dashed vertical line indicates the size of the pseudopotential core, $r=0.6a_0$. For comparison corresponding pair correlation functions for the hydrogen atom (dotted solid line) and H_2^+ (dotted line) obtained by using the analytical ground-state wave function of the hydrogen atom are also shown.

effects are more clearly seen in the dynamics of the nuclei; see Fig. 3. As one might expect, there is a noticeable difference between the AQ and BO electron-nucleus pair correlation functions due to varying bond length; see Fig. 4.

The AQ average nuclear separation is close to the value $2.064a_0$ obtained by a nonadiabatic VMC simulation [30]. The AQ pair correlation function of the nuclei (see Fig. 3) coincides with the scaled atomic orbital (SAO) one in Ref. [28] computed within the multicomponent density functional theory (MCDFT) scheme, not shown here.

All the spectroscopic constants in Table I are defined using the derivatives from a fitted Morse potential—i.e., BO potential energy surface. Thus, the "AQ spectroscopic constants" should be interpreted mainly as the direction of change in the values, except for B_e. The expectation values of the spectroscopic constants are obtained by weighting the equations by the nuclear pair correlation function from the corresponding simulation.

A projection of the AQ simulation to a potential curve of the nuclei is constructed with the help of the known solutions to the Morse potential. The distribution from the Morse wave function is fitted to the pair correlation function of the AQ simulation. The three-body system is then presented by an effective two-body potential. The projected potential curve shows clear differences in the dynamics of the nuclei between BO and AQ simulations; see Fig. 5. The minima of the potentials are set to zero: the difference in the dissociation energies between BO approach and AQ projection is about $0.036E_H$ and the shift in the equilibrium distance is $0.036a_0$. The spectroscopic constants with the projected potential curve are $B_e=29.26\ \mathrm{cm}^{-1}$, $\omega_e=2047.94\ \mathrm{cm}^{-1}$, $\omega_e x_e = 78.12\ \mathrm{cm}^{-1}$, and $\alpha_e=2.110\ \mathrm{cm}^{-1}$. All this indicates that an effective Morse potential is not capable of describing nonadiabatic effects correctly.

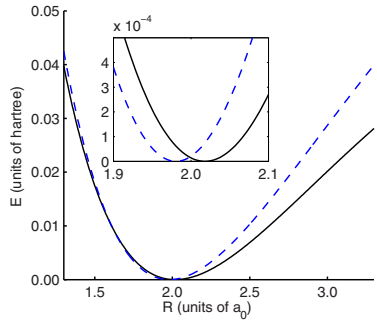

FIG. 5. (Color online) H_2^+ potential curves: Morse potential fitted to FD_{PP} (dashed line) and the effective Morse potential obtained from the projection of the AQ simulation (solid line); see the text for details. Corresponding nuclear pair correlation functions are shown in Fig. 3. The shift in the bond length is $0.036a_0$.

Finally, it may be of interest to see a visualization of the "polymer rings" representing the quantum particles in the PIMC simulation. So Fig. 6 presents the *xy*-plane (*z*-projection) snapshot from AQ simulation with Trotter number 2^{13} for all three particles. The "polymer ring" describing the electron is in the background and those of the nuclei are placed on top.

IV. CONCLUSIONS

The three-body quantum system, the hydrogen molecule ion (H_2^+), is reexamined, once again. The path-integral Monte Carlo method is used for evaluation of the stationary-state quantum dynamics. The PIMC method offers a finite-temperature approach together with a transparent tool to describe the correlations between the particles involved. We aim at tracing the electron-nuclei coupling effects in the three-body all-quantum—i.e., nonadiabatic—molecule. This is carried out by comparing the differences in adiabatic Born-Oppenheimer and AQ simulations and inspecting the projections from the AQ simulation onto the BO description

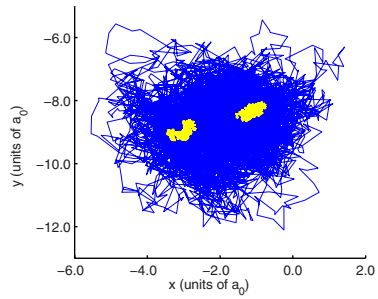

FIG. 6. (Color online) *xy*-plane (*z*-projection) snapshot from AQ simulation with Trotter number 2^{13} for all particles. The "polymer ring" describing the electron is in the background and those of the nuclei are placed on top.

of the electron-only and nuclear-only subsystems.

The approach turns out to be computationally demanding, but with the chosen pseudopotential for the attractive Coulomb potential and extrapolation to infinite Trotter number the task becomes feasible. By choosing low enough temperature, 300 K, we are able to compare our data to those from zero-kelvin quantum methods available in literature. Among others we have evaluated spectroscopic constants and molecular deformation, also considering the isotope effects.

With our fully basis set free, trial wave function free, and model free approach we are not able to compete in accuracy with the zero-kelvin benchmark values. However, due to the mixed-state density matrix formalism of the PIMC method, we are able to present the most transparent description of the particle-particle correlations.

Total energies from our simulations are more binding in nature compared to the benchmark values; see Table II. This is an expected effect of the pseudopotential in use; see Fig. 2 and FD_{PP} therein. The quantum dynamics of the system is well described, and distinct features of the coupling are observed for the nuclei: a shift of $0.056a_0$ in the equilibrium bond length, increase of $0.040a_0$ in the width of the pair correlation function of the nuclei, and nonadiabatic correction of about $0.00097E_H$ to the dissociation energy. The electronic distribution is less influenced by the coupling than the nuclear one upon the inclusion of nonadiabatic effects; see Figs. 3 and 4.

The projection of the nonadiabatic three-body system with the help of Morse wave functions onto the two-body nuclei-only subsystem indicates that the Morse potential is not capable of describing nonadiabatic effects correctly; see Fig. 5.

ACKNOWLEDGMENTS

For financial support we thank the Graduate School of Tampere University of Technology and the Academy of Finland and for computational resources the facilities of Finnish IT Center for Science (CSC) and Material Sciences National Grid Infrastructure (M-grid, akaatti).

[1] D. Marx and M. Parrinello, J. Chem. Phys. **104**, 4077 (1996).
[2] T. Lopez-Ciudad, R. Ramìrez, J. Schulte, and M. C. Böhm, J. Chem. Phys. **119**, 4328 (2003).
[3] R. Ramìrez, C. P. Herrero, and E. R. Hernàndez, Phys. Rev. B **73**, 245202 (2006).
[4] H.-P. Cheng, R. N. Barnett, and U. Landman, Chem. Phys. Lett. **237**, 161 (1995).
[5] M. Leino, J. Nieminen, and T. T. Rantala, Surf. Sci. **600**, 1860 (2006).
[6] M. Leino, I. Kylänpää, and T. T. Rantala, Surf. Sci. **601**, 1246 (2007).
[7] M. E. Tuckerman, D. Marx, M. L. Klein, and M. Parrinello, Science **275**, 817 (1997).
[8] B. N. Dickinson, J. Chem. Phys. **1**, 317 (1933).
[9] J. N. Silverman, D. M. Bishop, and J. Pipin, Phys. Rev. Lett. **56**, 1358 (1986).
[10] L. Adamowicz and R. J. Bartlett, J. Chem. Phys. **84**, 4988 (1986).
[11] H. W. Jones and B. Etemadi, Phys. Rev. A **47**, 3430 (1993).
[12] J. H. Macek and S. Y. Ovchinnikov, Phys. Rev. A **49**, R4273 (1994).
[13] V. V. Serov, B. B. Joulakian, D. V. Pavlov, I. V. Puzynin, and S. I. Vinitsky, Phys. Rev. A **65**, 062708 (2002).
[14] V. I. Korobov, Phys. Rev. A **74**, 052506 (2006).
[15] M. Vincke and D. Baye, J. Phys. B **18**, 167 (1985).
[16] J. F. Babb and A. Dalgarno, Phys. Rev. Lett. **66**, 880 (1991).
[17] K. T. Tang, J. P. Toennies, and C. L. Yiu, J. Chem. Phys. **94**, 7266 (1991).
[18] U. Kappes and P. Schmelcher, Phys. Rev. A **53**, 3869 (1996).
[19] A. Bouferguene, C. A. Weatherford, and H. W. Jones, Phys. Rev. E **59**, 2412 (1999).
[20] R. E. Moss, Phys. Rev. A **61**, 040501(R) (2000).
[21] C. Amovilli and N. H. March, Int. J. Quantum Chem. **106**, 533 (2006).
[22] A. K. Bhatia and R. J. Drachman, Phys. Rev. A **59**, 205 (1999).
[23] J. M. Taylor, A. Dalgarno, and J. F. Babb, Phys. Rev. A **60**, R2630 (1999).
[24] V. I. Korobov, Phys. Rev. A **63**, 044501 (2001).
[25] R. E. Moss and L. Valenzano, Mol. Phys. **64**, 649 (2002).
[26] Y. Ohta, J. Maki, H. Nagao, H. Kono, and Y. Fujimura, Int. J. Quantum Chem. **91**, 105 (2003).
[27] T. Kreibich and E. K. U. Gross, Phys. Rev. Lett. **86**, 2984 (2001).
[28] T. Kreibich, R. van Leeuwen, and E. K. U. Gross, e-print arXiv:cond-mat/0609697.
[29] C. A. Traynor, J. B. Anderson, and B. M. Boghosian, J. Chem. Phys. **94**, 3657 (1991).
[30] D. Bressanini, M. Mella, and G. Morosi, Chem. Phys. Lett. **272**, 370 (1997).
[31] X.-P. Li and J. Q. Broughton, J. Chem. Phys. **86**, 5094 (1987).
[32] L. Knoll and D. Marx, Eur. Phys. J. D **10**, 353 (2000).
[33] M. P. Surh, K. J. Runge, T. W. Barbee, E. L. Pollock, and C. Mailhiot, Phys. Rev. B **55**, 11330 (1997).
[34] M. C. Gordillo, Phys. Rev. B **60**, 6790 (1999).
[35] M. C. Gordillo and D. M. Ceperley, Phys. Rev. B **65**, 174527 (2002).
[36] M. Boninsegni, Phys. Rev. B **70**, 125405 (2004).
[37] J. E. Cuervo and P.-N. Roy, J. Chem. Phys. **125**, 124314 (2006).
[38] F. F. Abraham and J. Q. Broughton, Phys. Rev. Lett. **59**, 64 (1987).
[39] D. M. Ceperley, Rev. Mod. Phys. **67**, 279 (1995).
[40] M. Pierce and E. Manousakis, Phys. Rev. Lett. **81**, 156 (1998).
[41] M. Pierce and E. Manousakis, Phys. Rev. B **59**, 3802 (1999).
[42] Y. Kwon and K. B. Whaley, Phys. Rev. Lett. **83**, 4108 (1999).
[43] H. Kleinert, *Path Integrals in Quantum Mechanics, Statistics, Polymer Physics, and Financial Markets*, 3rd ed. (World Scientific, Singapore, 2004).
[44] E. L. Pollock and D. M. Ceperley, Phys. Rev. B **36**, 8343

(1987).
[45] R. P. Feynman, *Statistical Mechanics* (Perseus Books, Reading, Massachusetts, 1998).
[46] D. M. Ceperley, Rev. Mod. Phys. **67**, 279 (1995).
[47] N. Metropolis, A. W. Rosenbluth, M. N. Rosenbluth, A. H. Teller, and E. Teller, J. Chem. Phys. **21**, 1087 (1953).
[48] C. Chakravarty, M. C. Gordillo, and D. M. Ceperley, J. Chem. Phys. **109**, 2123 (1998).
[49] M. F. Herman, E. J. Bruskin, and B. J. Berne, J. Chem. Phys. **76**, 5150 (1982).
[50] J. M. Thijssen, *Computational Physics* (Cambridge University Press, Cambridge, England, 2000).
[51] S. D. Ivanov, A. P. Lyubartsev, and A. Laaksonen, Phys. Rev. E **67**, 066710 (2003).
[52] A. Dal Corso, A. Pasquarello, A. Baldereschi, and R. Car, Phys. Rev. B **53**, 1180 (1996).
[53] I. Kylänpää, Master's thesis, Tampere University of Technology, 2006.
[54] S. A. Alexander and R. L. Coldwell, Chem. Phys. Lett. **413**, 253 (2005).
[55] P. M. Morse, Phys. Rev. **34**, 57 (1929).
[56] J. Lounila and T. T. Rantala, Phys. Rev. A **44**, 6641 (1991).
[57] D. ter Haar, Phys. Rev. **70**, 222 (1946).
[58] J. Kobus, L. Laaksonen, and D. Sundholm, URL http://scarecrow.1g.fi/num2d.html

Paper II

I. Kylänpää and T. T. Rantala
Thermal dissociation of dipositronium: Path-integral Monte Carlo approach

Reprinted with permission from:
Physical Review A 80, 024504 (2009)

Thermal dissociation of dipositronium: Path-integral Monte Carlo approach

Ilkka Kylänpää and Tapio T. Rantala
Department of Physics, Tampere University of Technology, P.O. Box 692, FI-33101 Tampere, Finland
(Received 23 December 2008; published 27 August 2009)

Path-integral Monte Carlo simulation of the dipositronium "molecule" Ps_2 reveals its surprising thermal instability. Although, the binding energy is ~0.4 eV, due to the strong temperature dependence of its free-energy Ps_2 dissociates, or does not form, above ~1000 K, except for high densities where a small fraction of molecules are in equilibrium with Ps atoms. This prediction is consistent with the recently reported first observation of stable Ps_2 molecules by Cassidy and Mills, Jr., [Nature (London) **449**, 195 (2007); Phys. Rev. Lett. **100**, 013401 (2008)] at temperatures below 1000 K. The relatively sharp transition from molecular to atomic equilibrium, which we find, remains to be experimentally verified. To shed light on the origin of the large entropy factor in free-energy, we analyze the nature of interatomic interactions of these strongly correlated quantum particles. The conventional diatomic potential curve is given by the van der Waals interaction at large distances; but due to the correlations and high delocalization of constituent particles, the concept of potential curve becomes ambiguous at short atomic distances.

DOI: 10.1103/PhysRevA.80.024504 PACS number(s): 31.15.xk, 31.15.ae, 36.10.Dr

Dipositronium or positronium molecule Ps_2 is a four-body system consisting of two electrons and two positrons. The dynamical stability of dipositronium was established in 1947 by Hylleraas and Ore [1]. However, the molecule was not observed experimentally until recently [2], even though a lot of knowledge had been provided by a number of theoretical studies (see Refs. [3–9] and references therein). In addition to the fundamental issues of physics, Ps_2 is of interest also in astrophysical applications and in solid-state physics [10,11].

In laboratory conditions, Ps_2 formation has recently been observed resulting from implantation of intense pulses of positrons into porous silica films [2,12].

The positronium molecule, with all the four particles of the same mass, sets challenges to modeling since quantum calculations are to be performed fully nonadiabatically [13]. This, however, can be realized with quantum Monte Carlo (QMC) methods [14–16]. It should be pointed out that also for other systems, approaches that are not restricted by the Born-Oppenheimer or other adiabatic approximations are gaining more attention [16–23].

Among the QMC methods, the path-integral Monte Carlo (PIMC) offers a finite-temperature approach together with a transparent tool to trace the correlations between the particles involved. Though computationally challenging, with the carefully chosen approximations PIMC is capable of treating low-dimensional systems, such as small molecules or clusters, accurately enough for good quantum statistics for a finite-temperature mixed state [24–29].

In this study, using PIMC, we evaluate the density matrix of the full four-body quantum statistics in temperature-dependent stationary states. Thus, the temperature-dependent distributions of structures and energetics of Ps_2 are established. The main focus here is to find the preferred configuration of the four-body system at each temperature—Ps_2 molecule or two Ps atoms.

According to the Feynman formulation of the statistical quantum mechanics [30], the partition function for interacting distinguishable particles is given by the trace of the density matrix $\hat{\rho}(\beta)=e^{-\beta\hat{H}}$,

$$Z = \mathrm{Tr}\ \hat{\rho}(\beta) = \int dR_0 dR_1 \ldots dR_{M-1} \prod_{i=0}^{M-1} e^{-S(R_i,R_{i+1};\tau)},$$

where S is the action, $\beta=1/k_B T$, $\tau=\beta/M$, and M is called the Trotter number ($R_M=R_0$). In present simulations, we use the pair approximation of the action and matrix squaring for the evaluation of the Coulomb interactions [25,31]. Sampling of the paths in the configuration space is carried out using the Metropolis algorithm [32] with the bisection moves [33]. The Coulomb potential energy is obtained as an expectation value from sampling and the kinetic energy is calculated using the virial estimator [34].

The error estimate for the PIMC scheme is commonly given in powers of the imaginary time step τ [25]. Therefore, in order to determine comparable thermal effects on the system, we have carried out the simulations with similar sized time steps regardless of the temperature. This way the temperature-dependent properties can be compared avoiding temperature-dependent systematic errors. The standard error of the mean with two-sigma limits is used to indicate the statistical uncertainty, where relevant. The average of the chosen time step is $\langle\tau\rangle\approx 0.0146 E_H^{-1}$, where E_H denotes the atomic unit of energy, hartree (≈27.2 eV). The other atomic unit we use here is Bohr radius for the length a_0 (≈0.529 Å).

The total energy of positronium "atom" Ps is −0.25 at 0 K and the binding energy of the molecule Ps_2 is 0.0160 (≈0.435 eV) [8]. We find these values as zero Kelvin extrapolates from our simulations at low temperatures. We point out that with PIMC we evaluate energetics as statistical expectation values from sampling with less accuracy than that from conventional solutions of wave functions and the zero Kelvin data we obtain as extrapolates only.

In Fig. 1 we present the "apparent dissociation energy" of Ps_2 at several different temperatures. In each temperature, this is the negative total energy of the molecule with respect to two atoms as $D_T=-[\langle E_{\mathrm{tot}}^{\mathrm{Ps}_2}\rangle_T - 2\langle E_{\mathrm{tot}}^{\mathrm{Ps}}\rangle_T]$. At $T\leq 900$ K, we find for the average over shown temperatures $\bar{D}_T$

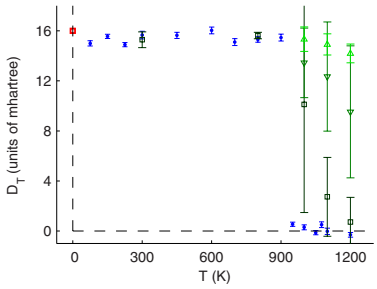

FIG. 1. (Color online) Apparent temperature-dependent dissociation energy of dipositronium in units of mhartree: zero Kelvin reference (square without error bars, red) and finite-temperature simulation results at the low-density limit (blue dots). Data from higher Ps density simulations are also shown (green): 0.50 (□), 14 (▽), and 100×10^{24} m^{-1} (△).

$=0.0154(5)$, which is very close to the dissociation energy at 0 K, D_0. However, at higher temperatures the apparent dissociation energy vanishes because $\langle E_{\rm tot}^{\rm Ps_2}\rangle_T$ and $2\langle E_{\rm tot}^{\rm Ps}\rangle_T$ become the same. This is because of molecular dissociation, or to be more exact, the two atoms do not bind in our equilibrium state simulation at $T\geq 900$ K and the predominant configuration is that of two separate positronium atoms.

Simulations in a well-defined Ps density are time consuming and, therefore, studies of this kind have been carried out at the transition region around 1000 K only. Using the periodic boundary conditions and the cubic supercells of sizes from $(300a_0)^3$ to $(50a_0)^3$ with two Ps atoms, we have simulated three densities from 0.5 to 100×10^{24} m^{-1}, respectively. We see that with increasing density, the equilibrium shifts to the molecular direction making the transition smoother and raising it to higher temperatures compared to the more sharp low-density limit.

For completeness, we should point out that in equilibrium at any finite temperature the zero density limit consists of Ps atoms only. Correspondingly, increasing density will eventually smoothen the transition away.

In the recent experiment cited above [2,12], the formation of Ps_2 molecules was observed below 900 K in about two orders of magnitude lower densities than our lowest, above (Fig. 1). Formation was not observed at higher temperatures, however, because the Ps atoms desorbed from the confining porous silica surface with the activation energy $k_BT\sim0.074$ eV (~850 K). Thus, our prediction of thermal dissociation of Ps_2 above 900 K in the experimentally achievable densities remains to be verified in forthcoming experiments in higher temperatures.

Next, we compare our finite-temperature Ps_2 data to the published zero Kelvin results, discuss the details of Ps-Ps interaction and, finally, conclude with the explanation of the higher-temperature instability.

The conventional zero Kelvin like Ps_2 state of the system is confirmed below 900 K from the distributions in Fig. 2 and related data in Table I. The pair-correlation functions for like and opposite charged particles are essentially identical with those reported elsewhere [6], and the expectation values of various powers of these distributions match with other

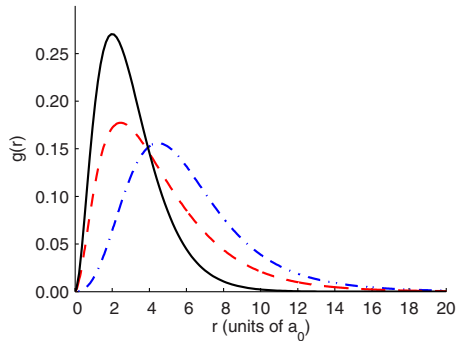

FIG. 2. (Color online) Temperature averaged pair-correlation functions for different particle pairs ($T\leq900$ K): e^- e^- and e^+ e^+ (dash dotted) and e^- e^+ (dashed). The ground-state ($T=300$ K) radial distribution of the free positronium atom is given as a reference (solid line). The pair-correlation functions are averaged over temperatures below 900 K. The distributions include the r^2 weight and normalization to one to allow direct comparison to other published data (see Table I).

published reference data. At higher temperatures, where $D_T\approx0$ K, the corresponding distributions and data become that of the free Ps atoms.

At 900 K, the thermal energy $k_BT=0.0030E_{\rm H}\approx0.08$ eV only. Therefore, the obvious question arises: why the Ps_2 molecule with binding energy 0.44 eV is unstable above 900 K? Is there a temperature dependence hidden in the interactions? What does the potential energy curve of this diatomic molecule look like?

It is the van der Waals interaction or so called dispersion forces that are expected to contribute to the potential curve at larger atomic distances. These arise from the "dynamic dipole-dipole correlations," as usually quoted. Now, within our approach we have a transparent way to consider these interactions: the dipoles and their relative orientations. Thus, we monitor the dipole-dipole orientation correlation function,

$$\left\langle \frac{\mathbf{p}_1\cdot\mathbf{p}_2}{p_1p_2}\right\rangle, \tag{1}$$

as a function of interatomic distance R, where $\mathbf{p}_1$ and $\mathbf{p}_2$ are the two e^-e^+ dipoles. This function assumes values from −1

TABLE I. Simulated and reference data [3,6,9,10,15] in atomic units. Our data are given as averages from temperatures $T\leq900$ K. Apart from the energy, the values are calculated using the averaged pair-correlation functions shown in Fig. 2. Electrons are labeled 1 and 2; positrons are 3 and 4. Because of symmetry $\langle r_{12}\rangle=\langle r_{34}\rangle$ and $\langle r_{13}\rangle=\langle r_{23}\rangle=\langle r_{14}\rangle=\langle r_{24}\rangle$.

	$\langle E_{\rm tot}\rangle$	$\langle r_{12}\rangle$	$\langle r_{13}\rangle$	$\langle r_{12}^{-1}\rangle$	$\langle r_{13}^{-1}\rangle$	$\langle r_{12}^{2}\rangle$	$\langle r_{13}^{2}\rangle$
Refs.	−0.5160	6.033	4.487	0.221	0.368	46.375	29.113
PIMC	−0.5154(5)	6.02	4.48	0.22	0.37	45.67	28.78

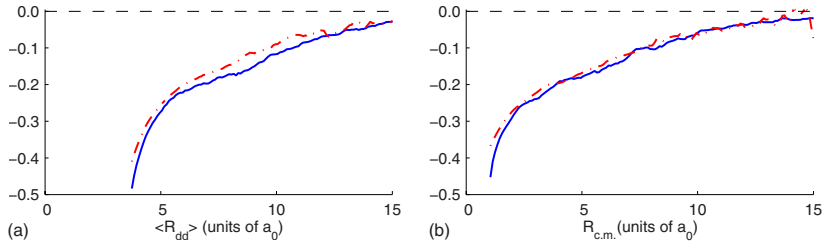

FIG. 3. (Color online) Dipole-dipole correlation functions [Eq. (1)]. The upper (dash dotted, red) and lower (solid, blue) curves correspond to 1000 K and 800 K, respectively. See the two definitions of the interatomic distances R_{dd} and $R_{c.m.}$ in text.

to 0, corresponding orientations from perfectly opposite to fully random.

The concept of interatomic distance needs to be defined for evaluation. We should note that at the "equilibrium distance" the centers-of-mass (c.m.) of all four particles are superimposed on the same location, as evaluated from their one-particle distributions (or wave functions). However, the particles do have well-defined (correlated) average distances (see Table I). Thus, the definition is not trivial.

We can define the center-of-mass interatomic distance $R_{c.m.}$ using the expectation value of the c.m. of one e^-e^+ pair and that of the other pair. An alternative (correlated) definition is the expectation value of the separation of the two e^-e^+ dipoles R_{dd}. At large distances, these two coincide; but at the opposite limit, in Ps_2 molecule, the former becomes zero whereas the latter remains at about 4 a_0.

Another problem is that in an equilibrium simulation we are not able to choose or fix the interatomic distance R ($R_{c.m.}$ or R_{dd}). Therefore, evaluation of R-dependent quantities presumes that sampling in the chosen temperature includes the relevant R with good enough statistics. This kind of data hunting turns out to be computationally challenging.

To overcome this, we have used a "close-to-equilibrium" technique by starting from 800 K distribution and rising the temperature to 1000 K, and then, applying the reverse change in temperature to obtain another estimate. In the former case, we are able to follow the increase in R from the molecular region to "dissociation," while the latter follows "recombination."

In Fig. 3 we show the estimates from these two temperatures to the correlation function with respect to the interatomic distances R_{dd} and $R_{c.m.}$. We emphasize that these are estimates, only, because at different temperatures the equilibrium sampling regions of R are very different. However, we see that the difference between these two estimates is very small and the equilibrium simulation correlation function between these two is easily conceived. Thus, we conclude that the dipole-dipole correlation is not temperature dependent.

Using the same close-to-equilibrium technique, we evaluate the van der Waals interaction energy next. This is shown in Fig. 4. There too, the true equilibrium curve can be estimated as the average of the two shown ones. Simple fit reveals that the large distance limit ($R_{dd} > 12a_0$) shows the asymptotic $R^{-\alpha}$ behavior (α roughly 6) as expected.

Sampling all the energy contributions with the same close-to-equilibrium technique allows us to evaluate the total energy or the diatomic potential energy curve as a function of interatomic distance $E_{tot}^{Ps_2}(R)$, where $R=R_{dd}$ or $R_{c.m.}$. It shows the same temperature-independent behavior, though the statistics is not good enough to allow showing the curve here. As expected, we find that the true dissociation energy is not temperature dependent, as is the apparent dissociation energy D_T shown in Fig. 1.

Now, the "thermal dissociation" can be explained by the strong temperature dependence of the Ps_2 free-energy. With the rising temperature, the free-energy of the two atoms decreases below that of the molecule, leading to transition from the molecular dominance to the atomic one. This is not a surprise, but the usual behavior of the conventional molecules. From our simulations, we find, however, the following surprising features: (i) the low temperature, where the transition takes place, (ii) sharpness of the transition, and (iii) almost negligible density dependence at the experimentally relevant densities.

The transition temperature is usually estimated by matching the thermal energy k_BT with the dissociation energy. This is where the entropic contribution in free-energy $-TS$ becomes comparable with the dissociation energy. In the present case, this gives about 5000 K. Conventionally, the transition is smooth following from the equilibrium between molecular dissociation and formation, where the former depends on the temperature and, the latter, on the density, the density being the main factor in the entropy.

The Ps_2 molecule lacking in the heavy nuclei is peculiar. All of its constituents are strongly delocalized, barely fitting into the binding regime of the molecular potential curve. This is what they do below 900 K in experimentally relevant densities, but not above 1000 K. This is a consequence from

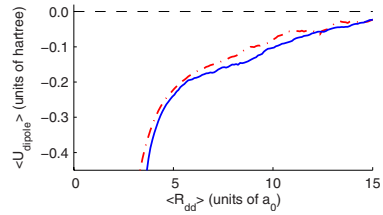

FIG. 4. (Color online) Dipole-dipole interaction energy with the same notations as in Fig. 3. The upper (dash dotted, red) and lower (solid, blue) curves correspond to 1000 K and 800 K, respectively.

the exceptionally large entropy factor originating from the strong quantum delocalization more than the density.

In summary, with path-integral Monte Carlo simulations of the dipositronium molecule Ps_2, we have found and explained its surprising thermal instability. Due to the strong temperature dependence of the free-energy of the considered four particle system, the molecular form is less stable than two positronium atoms above about 900 K, though the molecular dissociation energy is $\sim$0.4 eV. The transition in equilibrium from molecules to atoms is sharp in temperature and only weakly density dependent. This can be understood by the large entropy factor originating from strong delocalization of all of the molecular constituents. Our prediction remains to be experimentally verified.

We thank David Ceperley for his attention and interest in our work. For financial support, we thank the Academy of Finland, and for computational resources the facilities of Finnish IT Center for Science (CSC) and Material Sciences National Grid Infrastructure (M-grid, akaatti).

[1] E. A. Hylleraas and A. Ore, Phys. Rev. **71**, 493 (1947).
[2] D. B. Cassidy and A. P. Mills, Jr., Nature (London) **449**, 195 (2007).
[3] D. B. Kinghorn and R. D. Poshusta, Phys. Rev. A **47**, 3671 (1993).
[4] R. D. Poshusta and D. B. Kinghorn, Int. J. Quantum Chem. **60**, 213 (1996).
[5] D. Bressanini, M. Mella, and G. Morosi, Phys. Rev. A **55**, 200 (1997).
[6] J. Usukura, K. Varga, and Y. Suzuki, Phys. Rev. A **58**, 1918 (1998).
[7] J. Usukura and Y. Suzuki, Phys. Rev. A **66**, 010502(R) (2002).
[8] D. M. Schrader, Phys. Rev. Lett. **92**, 043401 (2004).
[9] D. H. Bailey and A. M. Frolov, Phys. Rev. A **72**, 014501 (2005).
[10] S. Bubin and L. Adamowicz, Phys. Rev. A **74**, 052502 (2006).
[11] M. Emami-Razavi, Phys. Rev. A **77**, 042104 (2008).
[12] D. B. Cassidy and A. P. Mills, Jr., Phys. Rev. Lett. **100**, 013401 (2008).
[13] P. M. Kozlowski and L. Adamowicz, Phys. Rev. A **48**, 1903 (1993).
[14] C. A. Traynor, J. B. Anderson, and B. M. Boghosian, J. Chem. Phys. **94**, 3657 (1991).
[15] D. Bressanini, M. Mella, and G. Morosi, Chem. Phys. Lett. **272**, 370 (1997).
[16] I. Kylänpää, M. Leino, and T. T. Rantala, Phys. Rev. A **76**, 052508 (2007).
[17] A. K. Bhatia and R. J. Drachman, Phys. Rev. A **59**, 205 (1999).
[18] J. M. Taylor, A. Dalgarno, and J. F. Babb, Phys. Rev. A **60**, R2630 (1999).
[19] V. I. Korobov, Phys. Rev. A **63**, 044501 (2001).
[20] T. Kreibich and E. K. U. Gross, Phys. Rev. Lett. **86**, 2984 (2001).
[21] Y. Ohta, J. Maki, H. Nagao, H. Kono, and Y. Fujimura, Int. J. Quantum Chem. **91**, 105 (2003).
[22] A. Chakraborty, M. V. Pak, and S. Hammes-Schiffer, Phys. Rev. Lett. **101**, 153001 (2008).
[23] T. Kreibich, R. van Leeuwen, and E. K. U. Gross, Phys. Rev. A **78**, 022501 (2008).
[24] X.-P. Li and J. Q. Broughton, J. Chem. Phys. **86**, 5094 (1987).
[25] D. M. Ceperley, Rev. Mod. Phys. **67**, 279 (1995).
[26] M. Pierce and E. Manousakis, Phys. Rev. B **59**, 3802 (1999).
[27] Y. Kwon and K. B. Whaley, Phys. Rev. Lett. **83**, 4108 (1999).
[28] L. Knoll and D. Marx, Eur. Phys. J. D **10**, 353 (2000).
[29] J. E. Cuervo and P.-N. Roy, J. Chem. Phys. **125**, 124314 (2006).
[30] R. P. Feynman, *Statistical Mechanics* (Perseus Books, Reading, Massachusetts, 1998).
[31] R. G. Storer, J. Math. Phys. **9**, 964 (1968).
[32] N. Metropolis, A. W. Rosenbluth, M. N. Rosenbluth, A. H. Teller, and E. Teller, J. Chem. Phys. **21**, 1087 (1953).
[33] C. Chakravarty, M. C. Gordillo, and D. M. Ceperley, J. Chem. Phys. **109**, 2123 (1998).
[34] M. F. Herman, E. J. Bruskin, and B. J. Berne, J. Chem. Phys. **76**, 5150 (1982).

Paper III

I. Kylänpää and T. T. Rantala
Finite temperature quantum statistics of H_3^+ molecular ion

Reprinted with permission from:
Journal of Chemical Physics 133, 044312 (2010)

Finite temperature quantum statistics of H_3^+ molecular ion

Ilkka Kylänpää[a] and Tapio T. Rantala
Department of Physics, Tampere University of Technology, P.O. Box 692, Tampere FI-33101, Finland

(Received 10 May 2010; accepted 26 June 2010; published online 30 July 2010; publisher error corrected 18 August 2010)

Full quantum statistical *NVT* simulation of the five-particle system H_3^+ has been carried out using the path integral Monte Carlo method. Structure and energetics are evaluated as a function of temperature up to the thermal dissociation limit. The weakly density dependent dissociation temperature is found to be around 4000 K. Contributions from the quantum dynamics and thermal motion are sorted out by comparing differences between simulations with quantum and classical nuclei. The essential role of the quantum description of the protons is established. © *2010 American Institute of Physics*. [doi:10.1063/1.3464758]

I. INTRODUCTION

The triatomic molecular ion H_3^+ is a five-body system consisting of three protons and two electrons. Being the simplest polyatomic molecule, it has been the subject of a number of theoretical and experimental studies over the years.[1–5] Experimentally, the H_3^+ ion was first detected in 1911 by Thompson;[6] however, definite spectroscopic studies were carried out not until 1980 by Oka.[7] Since then, this five-body system has proven to be relevant, also in astrophysical studies concerning the interstellar media and the atmosphere of gas planets. Therefore, low-density high-temperature H_3^+ ion containing atmospheres have been studied experimentally[8] as well as computationally.[9]

Until now, the computational approaches have consistently aimed at finding ever more accurate potential energy surfaces (PESs) for H_3^+ at 0 K and consequent calculations of the rovibrational states.[10,11] These calculations include Born–Oppenheimer (BO) electronic energies in various geometries often supplemented with adiabatic and relativistic corrections.[12,13] For the study of rovibrational transitions, it is desirable to have an analytical expression for the PES, which is usually generated using Morse polynomial fits.[10] Inclusion of the nonadiabatic effects, however, has turned out to be a cumbersome task, and so far they have not been rigorously taken into account.[4]

In this work, we evaluate the full five-body quantum statistics of the H_3^+ ion in a stationary state at temperatures below the thermal dissociation at about 4000 K. We use the path integral Monte Carlo (PIMC) approach, which allows us to include the Coulomb correlations between the particles exactly in a transparent way. Thus, we are able to monitor the fully nonadiabatic correlated quantum distributions of particles and related energies as a function of temperature. Furthermore, we are able to model the nuclei as classical mass points, in thermal motion or fixed as conventionally in quantum chemistry, and find the difference between these and the quantum delocalized nuclei.

The PIMC method is computationally expensive, but within the chosen models and numerical approximations, it has been proven to be useful with exact correlations and finite temperature.[14–21] For 0 K data with benchmark accuracies, however, the conventional quantum chemistry or other Monte Carlo methods, such as the diffusion Monte Carlo,[22] are more appropriate. Thus, it should be emphasized that we do not aim at competing in precision or number of decimals with the other approaches. Instead, we will concentrate on physical phenomena behind the finite-temperature quantum statistics.

Next, we will briefly describe the basics of the PIMC method and the model we use for the ion. In Sec. IV, we first compare our 160 K PIMC "ground state" to the 0 K ground state and then consider the higher temperature effects.

II. METHOD

According to the Feynman formulation of the quantum statistical mechanics,[23] the partition function for interacting distinguishable particles is given by the trace of the density matrix

$$Z = \mathrm{Tr}\ \hat{\rho}(\beta) = \int \mathrm{d}R_0 \mathrm{d}R_1 \cdots \mathrm{d}R_{M-1} \prod_{i=0}^{M-1} e^{-S(R_i,R_{i+1};\tau)},$$

where $\hat{\rho}(\beta)=e^{-\beta\hat{H}}$, S is the action, $\beta=1/k_\mathrm{B}T$, $\tau=\beta/M$, $R_M=R_0$, and M is called the Trotter number. In this paper, we use the pair approximation in the action[15,24] for the Coulomb interaction of charges. Sampling in the configuration space is carried out using the Metropolis procedure[25] with bisection moves.[26] The total energy is calculated using the virial estimator.[27]

The error estimate in the PIMC scheme is commonly given in powers of the imaginary time time-step τ.[15] Therefore, in order to systematically determine thermal effects on the system, we have carried out all the simulations with $\tau=0.03E_\mathrm{H}^{-1}$, where E_H denotes the unit of hartree. Thus, the temperatures and Trotter number M become fixed by the relation $T=(k_\mathrm{B}M\tau)^{-1}$.

In the following, we mainly use the atomic units, where the lengths, energies, and masses are given in units of the

[a]Electronic mail: ilkka.kylanpaa@tut.fi.

bohr radius (a_0), hartree (E_H), and free electron mass (m_e), respectively. The statistical standard error of the mean (SEM) with 2SEM limits is used as an error estimate for the observables, unless otherwise mentioned.

III. MODELS

Two of the five particles composing the H_3^+ ion are electrons. For these, we do not need to sample the exact Fermion statistics, but it is sufficient to assign spin-up to one electron and spin-down to the other one. This is accurate enough, as long as the thermal energy is well below that of the lowest electronic triplet excitation.

We apply the same particle statistics for the three protons, too. This is even safer because the overlap of well localized nuclear wave functions is negligible and related effects become very hard to evaluate, anyway. On the other hand, however, the nuclear exchange due to the molecular rotation results in the so called zero-point rotations. These too contribute to energetics less than the statistical accuracy of our simulations. Therefore, we ignore the difference between ortho-H_3^+ ($I=3/2$) and para-H_3^+ ($I=1/2$). Thus, the protons are modeled as "boltzmannons" with the mass $m_p = 1.836\,152\,672\,48 \times 10^3 m_e$. The higher the temperature, the better is the Boltzmann statistics in describing the ensemble composed of ortho-H_3^+ and para-H_3^+.

For the NVT simulations, we place one H_3^+ ion into a cubic box with the volume of $(300a_0)^3$ and apply periodic boundary conditions and minimum image principle. This corresponds to the mass density of $\sim 1.255 \times 10^{-6}$ gcm^{-3}. This has no essential effect at low T, but at high T the finite density gives rise to the molecular recombination balancing the possible dissociation. Within the considered temperature range, the contributions from the dissociated states are negligible.

The electrons are always simulated with the full quantum dynamics. For the nuclei, however, we use three models to trace the quantum and thermal fluctuations separately. The case of full quantum dynamics of all particles we denote by AQ (all-quantum), the mass point model of protons by CN (classical nuclei), and the adiabatic case of fixed nuclei by BO (Born–Oppenheimer potential energy surface).

IV. RESULTS AND DISCUSSION

A. Ground state: 0 K reference data

The equilibrium geometry of the H_3^+ ion in its ground state is an equilateral triangle D_{3h} for which the internuclear equilibrium distance is $R=1.65a_0$.[4] The best upper bound for the electronic ground state BO energy to date is $-1.343\,835\,625\,02E_H$.[4] The vibrational normal modes of H_3^+ are the symmetric-stretch mode ν_1 and the doubly degenerate bending mode ν_2. The latter one breaks the full symmetry of the molecule, and therefore it is infrared active.[5]

The vibrational zero-point energy is $0.019\,87E_H$ and the so called rotational zero-point energies are $0.000\,29E_H$ and $0.000\,40E_H$ for para-H_3^+ and ortho-H_3^+, respectively.[3,11] These yield about $0.020\,215E_H$ for the average zero-point energy. Note, however, that the nuclear spins and zero point rotation are not included in our model of H_3^+.

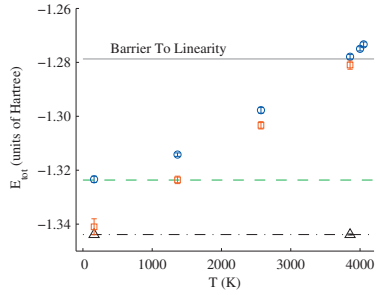

FIG. 1. Total energy of the H_3^+ molecular ion as a function of temperature. Fully nonadiabatic quantum statistical simulations [AQ (blue circles)], classical nuclei simulations [CN (red squares)], and the equilibrium geometry Born–Oppenheimer simulation [BO (black triangles)]. 0 K data (Refs. 3, 4, and 11) are given for comparison: BO ground state energy at equilibrium internuclear geometry (black dashed-dotted line), energy including the nuclear zero-point motion (green dashed line), and energy at the barrier to linearity (gray solid line). 2SEM statistical error estimate is shown by the error bars from simulations at the H_3^+ ion density $(300a_0)^{-3}$ or $\sim 1.255 \times 10^{-6}$ g cm^{-3}.

The lowest electronic excitation from the BO ground state is a direct Franck–Condon one ($0.710E_H$) (Refs. 4 and 5) to dissociative potential curve: $H_3^+ \rightarrow H_2 + H^+$ or $H_3^+ \rightarrow H_2^+ + H$.[4,28] The dissociation energies (D_e) are $0.169E_H$ and $0.241E_H$, respectively.

The linear geometry with equal bond lengths $1.539\,12a_0$ ($D_{\infty h}$) is a saddle point on the BO PES at $-1.278\,681\,90E_H$ (Ref. 11) or $0.065\,15E_H$ above the BO energy at the equilibrium geometry. This energy is usually called as the barrier to linearity.[2] The 0 K energetics is shown in Fig. 1 by the three horizontal lines.

B. PIMC ground state: 160 K

At our lowest simulation temperature $T \approx 160$ K, the electronic system is essentially in its ground state. For the total energy we find $-1.3438(2)E_H$, see the BO black triangles in Fig. 1. The thermal energy is $k_B T = 0.000\,507E_H$, and therefore, the contribution from the rotational and vibrational excited states is also small and we find $-1.3406(29)E_H$, see the CN red square in the same figure. The full quantum simulation includes vibrational zero-point contribution and yields $-1.3233(12)E_H$, about $0.0205(14)E_H$ above the BO energy in a good agreement with about $0.0202E_H$ in Refs. 3 and 11.

From our AQ simulation we still find the equilateral triangle configuration of the nuclei with the internuclear distances increased to $\langle R \rangle = 1.723(4)a_0$, which indicates an increase of about $0.073(4)a_0$, as compared with the 0 K BO equilibrium distance bond lengths. Interestingly, within the error limits, this is the same as the bond length increase of the hydrogen molecule ion H_2^+. The zero-point energy of H_3^+ is about 2.7 times as large as that of the H_2^+ ion,[21] as expected from the increase of vibrational modes from one to three—the zero-point energy of our model does not contain the rotational zero-point energy, as mentioned earlier.

The thermal motion (CN) alone increases the bond length to $\langle R \rangle = 1.658(4)a_0$ only (see the data in Figs. 2 and 3).

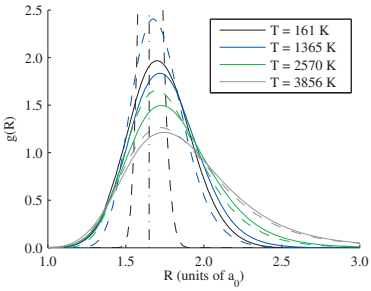

FIG. 2. Nuclear pair correlation functions (bond length distributions) at different temperatures from the quantum statistical simulations (solid lines) and from the classical nuclei simulations (dashed lines). The 0 K equilibrium internuclear distance is given as a vertical black dashed-dotted line. The distributions include the r^2 weight and normalization to unity. (Note that the r^2 weight is usually not included in description of extended or periodic systems.)

This clearly points out the difference between quantum and thermal delocalization of the nuclei at low T.

For the proton-electron and electron-electron interactions, the differences between our two approaches are smaller than in the proton-proton case but still distinctive. Comparison of the fixed nuclei simulation to the CN one shows that the two schemes give almost identical distributions. The AQ distributions, however, cannot be labeled identical with those from the CN or fixed nuclei simulations. The distributions are given in Figs. 4 and 5, where the notations are the same as in Fig. 2.

The calculations of the relativistic corrections involve, among other things, evaluation of the contact densities $\langle\delta(r_{ij})\rangle$ for the electron-nuclei and the electron-electron pairs.[12] For the electron-nuclei contact density at the BO equilibrium configuration, we get 0.1814(20) and for the AQ case, 0.1765(20). For the electron-electron pair we get 0.0182(3) and 0.0166(3) for BO and AQ approaches, respectively. The estimated uncertainties due to extrapolation to the contact are given in parentheses. The 0 K reference values[12] for the BO case are 0.181 242 (electron-nuclei) and 0.018 386 63 (electron-electron). Thus, the quantum dynamics of the nuclei turns out to be a significant factor in lowering the contact densities, too. See the snapshot of the AQ simulation in Fig. 6 for some intuition of the low-temperature quantum distributions in imaginary time.

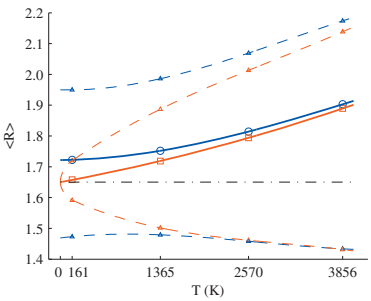

FIG. 3. Expectation values of the internuclear distance at different temperatures from distributions in Fig. 2. Quantum statistical simulations (blue circles) and classical nuclei simulations (red squares). The FWHM limits are shown by triangles (all the lines are for guiding the eye). The 0 K equilibrium internuclear distance is shown as a horizontal black dashed-dotted line.

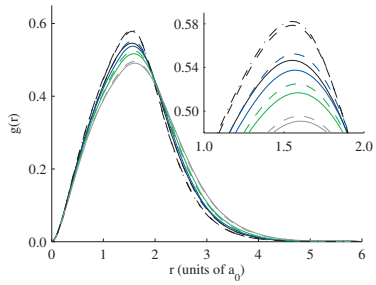

FIG. 4. Proton-electron pair correlation functions at the four temperatures from the full quantum statistical simulations [AQ (solid lines)] and from simulations with the classical nuclei [CN (dashed lines)]. That from the BO scheme is given at the lowest (electronic) temperature only (dashed-dotted line). Notations are the same as in Fig. 2.

C. High temperature phenomena

With the increasing temperature, the increasing contribution from rovibrational excitations is clearly seen in the total energies shown in Fig. 1. Contributions from the electronic excitations do not appear because the lowest excitation energy $0.710E_H$ is much too high as compared to the thermal energy k_BT. Consequently, the equilibrium geometry BO energy depends on the temperature almost negligibly. For convenience, the essential energetics related data have been collected into Table I also.

As expected, the increase in the total energy due to the classical rovibrational degrees of freedom is $9\times\frac{1}{2}k_BT$, defining the slope of the CN line. The most prominent quantum feature in AQ curve is, of course, the zero-point vibration energy. At higher temperatures, however, by comparing the AQ and CN curves we see that the quantum nature of nuclear dynamics becomes less important, except for dissociation.

At the dissociation limit we find the molecule with quantum nuclei somewhat more stable than the one with classical nuclei. With the relatively low density $(300a_0)^{-3}$, the molecule is mainly kept in one piece above 4000 K in the former case, whereas more dissociated in the latter. The total energy becomes higher for the CN than the AQ case slightly below

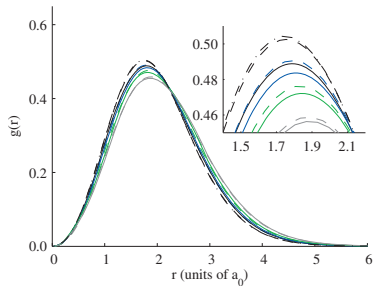

FIG. 5. Electron-electron pair correlation functions from the same simulations as those in Fig. 4. Notations are the same as in Figs. 2 and 4.

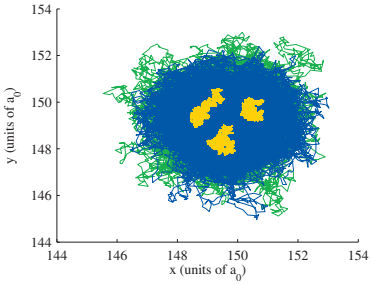

FIG. 6. xy-plane (z-projection) snapshot of the H_3^+ ion from quantum statistical simulation with Trotter number 2^{16}, i.e., temperature of about 160 K, for all particles. "Polymer rings" describing the electrons are in the background (green and blue) and those of the nuclei are placed on top (yellow).

4000 K (see Table I). The total energies at this crossing point are above the "barrier to linearity,"[2,11] already.

At higher temperatures $T \geq 4100$ K, other configurations, such as H_2+H^+, $H_2^+ + H$, and $2H+H^+$, start playing more significant roles in the equilibrium dissociation-recombination processes. These will be considered in our next study.

The nuclear pair correlation function or bond length distributions (Figs. 2 and 3) follow the energetics discussed above. There, the zero-point vibration in AQ case is seen even better. At the 0 K limit both the expectation value and the distribution, in particular, are significantly different from those of the CN case.

The temperature dependence in the other pair correlation functions is weak (see Figs. 4 and 5). Obviously, this is the case, because electrons do not present a quantum-to-classical transition in the temperature range considered, now. Thus, the evolution in distributions in Figs. 4 and 5 following the rising temperature arises from the changes in the nuclear dynamics, and mostly, from the change in the conformation or the bond lengths, presented in Fig. 3.

V. CONCLUSIONS

In this study, the path integral Monte Carlo method was shown to be a successful approach for examination of quantum statistics of the five-particle molecule, H_3^+ ion. The method is based on the finite temperature mixed state description, and thus, it gives information, which is complementary to the high-accuracy 0 K description of conventional quantum chemistry. It was also shown how contributions from quantum and thermal dynamics to particle distributions and correlation functions can be sorted out, and furthermore, quantum-to-classical dynamics transition can be monitored.

Our approach is fully basis set and trial wave function free. It is based on the Coulomb interactions only and allows the most transparent interpretation of consequent particle-particle correlations.

Simulation at 160 K essentially reproduces the 0 K data from conventional quantum chemistry. Of course, a proper extrapolation to 0 K can be done for more accuracy. BO potential energy surface and the equilibrium geometry can be found by using classical nuclei with fixed coordinates. Description of the zero-point motion within our nonadiabatic five-body quantum simulation gives the vibrational zero-point energy accurately. We find an increase of $0.073(4)a_0$ in the bond length due to the nonadiabatic zero-point vibration. The classical thermal contribution at 160 K is $0.008(4)a_0$, only.

With the raising temperature the rovibrational excitations contribute to the energetics, as expected, whereas the electronic part remains in its ground state in the spirit of BO approximation. At about 4000 K the H_3^+ ion dissociates, weakly depending on the ion density. We find that the full quantum molecule dissociates at slightly higher temperature compared to the one where the nuclei are modeled by classical particles with thermal dynamics only. Thus, we conclude the necessity of the quantum character of the protons in the correct description of dissociation.

We find that the nuclear quantum dynamics has a distinctive effect on the pair correlation functions, too. This is least for the electron-electron pair correlation function, stronger for the electron-proton one and largely increased in the proton-proton correlations. These are seen in the contact densities and, consequently, in the relativistic corrections where relevant.

TABLE I. Energetics of the H_3^+ molecular ion. The energies are given in units of hartree (atomic units). Simulation data are given with 2SEM error estimates. BO refers to Born–Oppenheimer calculation at equilibrium geometry. The reference data are rounded to convenient accuracy. The barrier to linearity is $0.065\ 15E_H \approx 1.8$ eV above the E_{BO} at 0 K.

	T (K)	E_{BO}	E_{CN}	E_{AQ}
Reference 4	0	−1.343 836		−1.323 568[a]
PIMC	~161	−1.3438(2)	−1.3406(29)	−1.3233(12)
PIMC	~1365		−1.3236(8)	−1.3142(4)
PIMC	~2570		−1.3033(7)	−1.2977(6)
PIMC	~3856	−1.3438(2)	−1.2810(8)	−1.2770(2)
PIMC	~3999		−1.1469(9)	−1.2750(4)
PIMC	~4050			−1.2734(9)

[a]For ortho-H_3^+ estimated by using Refs. 3 and 4.

ACKNOWLEDGMENTS

For financial support we thank the Academy of Finland and for computational resources the facilities of Finnish IT Center for Science (CSC) and Material Sciences National Grid Infrastructure (M-grid, Akaatti). We also thank Kenneth Esler and Bryan Clark for their advice concerning the pair approximation.

[1] T. Oka, Rev. Mod. Phys. **64**, 1141 (1992).
[2] J. L. Gottfried, B. J. McCall, and T. Oka, J. Chem. Phys. **118**, 10890 (2003).
[3] W. Kutzelnigg and R. Jaquet, Philos. Trans. R. Soc. London, Ser. A **364**, 2855 (2006).
[4] M. Pavanello and L. Adamowicz, J. Chem. Phys. **130**, 034104 (2009).
[5] H. Kreckel, D. Bing, S. Reinhardt, A. Petrignani, M. Berg, and A. Wolf, J. Chem. Phys. **129**, 164312 (2008).
[6] J. J. Thomson, Philos. Mag. **21**, 225 (1911).
[7] T. Oka, Phys. Rev. Lett. **45**, 531 (1980).
[8] M. B. Lystrup, S. Miller, N. D. Russo, J. R. J. Vervack, and T. Stallard, Astrophys. J. **677**, 790 (2008).
[9] T. T. Koskinen, A. D. Aylward, and S. Miller, Astrophys. J. **693**, 868

(2009).
[10] W. Meyer, P. Botschwina, and P. Burton, J. Chem. Phys. **84**, 891 (1986).
[11] R. Röhse, W. Kutzelnigg, R. Jaquet, and W. Klopper, J. Chem. Phys. **101**, 2231 (1994).
[12] W. Cencek, J. Rychlewski, R. Jaquet, and W. Kutzelnigg, J. Chem. Phys. **108**, 2831 (1998).
[13] R. A. Bachorz, W. Cencek, R. Jaquet, and J. Komasa, J. Chem. Phys. **131**, 024105 (2009).
[14] X.-P. Li and J. Q. Broughton, J. Chem. Phys. **86**, 5094 (1987).
[15] D. M. Ceperley, Rev. Mod. Phys. **67**, 279 (1995).
[16] M. Pierce and E. Manousakis, Phys. Rev. B **59**, 3802 (1999).
[17] Y. Kwon and K. B. Whaley, Phys. Rev. Lett. **83**, 4108 (1999).
[18] L. Knoll and D. Marx, Eur. Phys. J. D **10**, 353 (2000).
[19] J. E. Cuervo and P.-N. Roy, J. Chem. Phys. **125**, 124314 (2006).
[20] I. Kylänpää and T. T. Rantala, Phys. Rev. A **80**, 024504 (2009).
[21] I. Kylänpää, M. Leino, and T. T. Rantala, Phys. Rev. A **76**, 052508 (2007).
[22] J. Anderson, J. Chem. Phys. **96**, 3702 (1992).
[23] R. P. Feynman, *Statistical Mechanics* (Perseus, Reading, MA, 1998).
[24] R. G. Storer, J. Math. Phys. **9**, 964 (1968).
[25] N. Metropolis, A. W. Rosenbluth, M. N. Rosenbluth, A. H. Teller, and E. Teller, J. Chem. Phys. **21**, 1087 (1953).
[26] C. Chakravarty, M. C. Gordillo, and D. M. Ceperley, J. Chem. Phys. **109**, 2123 (1998).
[27] M. F. Herman, E. J. Bruskin, and B. J. Berne, J. Chem. Phys. **76**, 5150 (1982).
[28] L. P. Viegas, A. Alijah, and A. J. C. Varandas, J. Chem. Phys. **126**, 074309 (2007).

Paper IV

I. Kylänpää and T. T. Rantala
First-principles simulation of molecular dissociation–recombination equilibrium

Reprinted with permission from:
Journal of Chemical Physics 135, 104310 (2011)

First-principles simulation of molecular dissociation–recombination equilibrium

Ilkka Kylänpää[a] and Tapio T. Rantala[b]
Department of Physics, Tampere University of Technology, P.O. Box 692, FI-33101 Tampere, Finland

(Received 25 May 2011; accepted 17 August 2011; published online 9 September 2011)

For the first time, the equilibrium composition of chemical dissociation–recombination reaction is simulated from first-principles, only. Furthermore, beyond the conventional *ab initio* Born–Oppenheimer quantum chemistry the effects from the thermal and quantum equilibrium dynamics of nuclei are consistently included, as well as, the nonadiabatic coupling between the electrons and the nuclei. This has been accomplished by the path integral Monte Carlo simulations for full NVT quantum statistics of the H_3^+ ion. The molecular total energy, partition function, free energy, entropy, and heat capacity are evaluated in a large temperature range: from below room temperature to temperatures relevant for planetary atmospheric physics. Temperature and density dependent reaction balance of the molecular ion and its fragments above 4000 K is presented, and also the density dependence of thermal ionization above 10 000 K is demonstrated. © *2011 American Institute of Physics*. [doi:10.1063/1.3633516]

I. INTRODUCTION

The H_3^+ molecular ion has been the subject of a number of theoretical and experimental studies since its first experimental detection.[1] Because of its rapid formation through the exothermic reaction ($\Delta E \approx -1.7$ eV),

$$H_2 + H_2^+ \rightarrow H_3^+ + H, \tag{1}$$

the H_3^+ ion is expected in any active environment containing molecular hydrogen,[2] and thus, it is encountered, e.g., in hydrogen plasma and in the atmosphere of giant planets.[3,4] This smallest polyatomic molecule dissociates to several fragments in a temperature and density dependent manner. It is a five-particle system, and therefore, small enough to allow related simulations based on first-principles, only.

In planetary atmospheric physics, importance of the H_3^+ ion lies in its capability to act as a cooling agent via infrared radiation.[5–7] The atmospheric models taking into account this cooling are commonly based on the high temperature molecular partition function of the H_3^+ ion.[2] Conventional evaluation of the partition function faces, however, a few challenges of which the first one is finding a good approximation to the infinite summation over all rovibrational quantum states with accurate enough energies.[2] This has usually been worked out with the calculations of a finite number of states from, e.g., a semi-empirical potential energy surface.[8]

The next challenge comes with the changing geometry of the H_3^+ ion at finite temperature. The rovibrational model needs to be extended for calculations of correct energetics for the emerging linear geometry of the weakly bound molecule.[5]

Finally, as pointed out above, at finite temperatures the molecule may also dissociate to its fragments, and in fact, the equilibrium reaction

$$\begin{aligned} H_3^+ &\leftrightarrow H_2 + p^+ \\ &\leftrightarrow H_2^+ + H \\ &\leftrightarrow 2H + p^+ \\ &\leftrightarrow H + 2p^+ + e^- \\ &\leftrightarrow 3p^+ + 2e^-, \end{aligned} \tag{2}$$

needs to be considered, the balance depending strongly on both the temperature and the density of H_3^+ ions.

This brings forth two questions, at the least. First, how relevant it is to consider the molecular energetics and related partition function at temperatures where the molecule has dissociated and appears in form of fragments of the equilibrium reaction, Eq. (2), only. Second, the balance of the equilibrium reaction may be strongly affected, not only by the density, but also by the environment including the neutralizing negative counterparts of the positive H_3^+. Thus, the thermal dissociation–recombination balance above dissociation temperature gives rise to problems, which have yet not been taken into account in this context.

To start with we first define the molecular partition function (and other molecular quantities) as the one of the system of particles that constitute the molecule. Thus, the low temperature limit gives us, in practice, the conventional textbook molecular partition function. However, this generalization allows us to extend the concept of molecular partition function (and the other molecular quantities) seamlessly to higher temperatures, where the molecule may dissociate and recombine in density and temperature dependent balance.

Similar definition of the molecule as a five-particle system allows us to carry out simulations of the full quantum statistics of the H_3^+ ion, now described by Eq. (2), at low densities and temperatures ranging from 160 K up to about 15 000 K using the path integral quantum Monte Carlo

[a]Electronic mail: ilkka.kylanpaa@tut.fi.
[b]Electronic mail: tapio.rantala@tut.fi.

(PIMC) method. PIMC is the method to meet the above challenges: we need not make any approximations or restrictions in the summing over states, geometries, or quantum effects in equilibrium dynamics. The finite temperature is inherent in the PIMC approach and the Coulomb many-body treatment of the particle–particle interactions is exact. The PIMC method is computationally expensive, but feasible for small enough systems.[9–14]

The conventional quantum chemical *ab initio* description of the H_3^+ ion emerges as the zero Kelvin extrapolate from the PIMC simulations as we have shown earlier.[15] There, we evaluated the differences between three models for the description of the nuclear dynamics: the Born–Oppenheimer approximation, nuclei in thermal motion and nuclei in both thermal and quantum dynamics. At low temperatures the necessity of the fully quantum mechanical approach for all five particles was established.

In Sec. II, we present the essential details of the Feynman path integral quantum statistical approach, numerical simulation method, and the model of the H_3^+ ion. In Sec. III, we present and analyze the energetics, partition function, and other thermodynamic functions of the system fitting to analytical forms where pertinent. In the last section the conclusions are given.

II. METHOD AND MODELS

According to the Feynman path integral formulation of the quantum statistical mechanics[16] the partition function of interacting distinguishable particles is given by the trace of the density matrix $\hat{\rho}(\beta) = e^{-\beta \hat{H}}$ as

$$Z = \mathrm{Tr}\hat{\rho}(\beta) = \int \mathrm{d}R_0 \mathrm{d}R_1 \ldots \mathrm{d}R_{M-1} \prod_{i=0}^{M-1} e^{-S(R_i, R_{i+1}; \tau)}, \tag{3}$$

where the action $S(R_i, R_{i+1}; \tau)$ is taken over the path $R_i \rightarrow R_{i+1}$ in imaginary time $\tau = \beta/M$, where $\beta = 1/k_\mathrm{B}T$ and M is called the Trotter number. The trace implies a closed path ($R_M = R_0$).

For simulation, we use the pair approximation in the action[9,17] for the Coulomb interaction of charges. This is exact in the limit $M \rightarrow \infty$, but chemical accuracy is reached with sufficiently large M, i.e., small enough τ. Sampling in the configuration space $\{R_i\}$ in NVT ensemble is carried out using the Metropolis algorithm[18] with bisection and displacement moves.[19] The total energy is calculated using the virial estimator,[20] which is proper for molecular energetics.

The error estimate in the PIMC scheme is commonly given in powers of the imaginary time-step τ.[9] Therefore, in order to systematically determine the thermal effects on the system we have carried out all the simulations with $\tau = 0.03 E_\mathrm{H}^{-1}$, where E_H denotes the unit of Hartree. Thus, the temperatures and the Trotter number M are related by $T = (k_\mathrm{B} M \tau)^{-1}$, where k_B is the Boltzmann constant.

In the following we mainly use the atomic units, where the lengths, energies, and masses are given in the units of Bohr radius (a_0), Hartree (E_H), and free electron mass (m_e), respectively. Thus, for the mass of the electrons we take $m_\mathrm{e} = 1$ and for the protons $m_\mathrm{p} = 1.836\,152\,672\,48 \times 10^3 m_\mathrm{e}$. Conversion of the units of energy is given by $E_\mathrm{H} = 219\,474.631\,370\,5\ \mathrm{cm}^{-1} \approx 27.2$ eV, and correspondingly, $k_\mathrm{B} = 3.166\,815\,2 \times 10^{-6} E_\mathrm{H}\,\mathrm{K}^{-1}$.

The statistical standard error of the mean (SEM) with 2 SEM limits is used as an error estimate for the evaluated observables.

For the NVT simulations, we place one H_3^+ ion, i.e., three protons and two electrons, into a cubic box and apply periodic boundary conditions and the minimum image principle. The simulations are performed in three different super cell (box) volumes: $(300a_0)^3$, $(100a_0)^3$, and $(50a_0)^3$. These correspond to the mass densities of $\sim 1.255 \times 10^{-6}\,\mathrm{g\,cm}^{-3}$, $\sim 3.388 \times 10^{-5}\,\mathrm{g\,cm}^{-3}$, and $\sim 2.710 \times 10^{-4}\,\mathrm{g\,cm}^{-3}$, respectively, which are relevant to H_3^+ ion containing atmospheres.[6] The density has no essential effect at low T, where dissociation rarely takes place. At higher T, however, the finite density gives rise to the molecular recombination balancing the more frequent dissociation.

It should be pointed out that application of the minimum image principle with only one molecular ion in the periodic super cell may give both rise to the finite-size effects and also disregard high density distribution effects, i.e., fragments of several ions in the simulation box. Thus, the lower the density the better we are able to minimize the finite-size effects, which in this work are negligible, if not absent. In principle, the zero density limit cannot be reached due to the finite T. To avoid all these high density distribution ambiguities we have defined our targets as molecular energetics, molecular partition function, and other related molecular quantities, at all temperatures and considered low densities. Therefore, in the following, we also exclude the trivial contribution from the center-of-mass thermal dynamics and energy $3/2 k_\mathrm{B} T$ to the molecular quantities.

We do not simulate the real-time quantum dynamics with our approach, but evaluate the quantum statistics of the thermal equilibrium from the imaginary time paths of particles. However, the energetics and other expectation values evaluated from the correct quantum statistics inherently include all contributions from the equilibrium thermal motion and quantum dynamics in translationally, vibrationally, and rotationally excited states.[16] With rising temperature, the thermal contribution takes over leading to the classical limit, whereas decrease towards zero Kelvin takes to the quantum limit, where only the zero point motion remains.[15]

The contribution to energetics from nuclear quantum dynamics, which was shown to be essential at low T, turns out to be negligible at higher temperatures. It is included, however, to be consistent with the low temperature results and our earlier study. Also, the distinguishable particle (boltzmannon) simulation was shown to be accurate for the nuclei due to the negligible overlap of nuclear wavefunctions and the two electrons in singlet state. Now, at higher temperatures both assumptions are still valid as the direct Franck–Condon transition energies of H_3^+ and H_2 to the lowest triplet state are still more than an order of magnitude larger than the thermal energy of these molecules in our simulations.[21–23] For the free fragments, the overlap of electronic wavefunctions is again

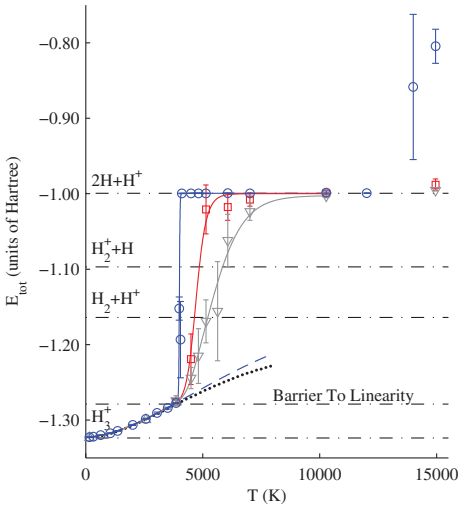

FIG. 1. NVT total energy of the H_3^+ molecular ion as a function of temperature at three different densities: blue circles ($\sim 1.255 \times 10^{-6}\,\mathrm{g\,cm^{-3}}$), red squares ($\sim 3.388 \times 10^{-5}\,\mathrm{g\,cm^{-3}}$), and gray triangles ($\sim 2.710 \times 10^{-4}\,\mathrm{g\,cm^{-3}}$). The blue dashed line is the energy fitted to Eq. (7). The black dots give the energy computed using the partition function fit given in Ref. 2. The horizontal dashed-dotted lines are the nonadiabatic zero Kelvin energies for the ion, its fragments and the barrier to linearity. The high temperature solid lines are mainly for guiding the eye, but used later for numerical evaluation of the partition function.

negligible and contributions from the weak overlapping configurations turns out to be vanishing.

For more details about the model and a discussion about the here neglected contribution from the exchange interaction, see Ref. 15.

III. RESULTS AND DISCUSSION

A. Overview of molecular energetics

In Fig. 1, the NVT total energy (canonical ensemble internal energy) of the H_3^+ ion and its fragments is shown as a function of temperature. The molecular energy does not include the center-of-mass translational kinetic energy $3/2k_BT$. The data from simulations are given as circles, squares, and triangles corresponding to the three densities. The PIMC data is also given in Tables I and II.

The solid lines at $T < 4000$ K are fitted to analytical model forms but at higher temperatures lines are only for guiding the eye. Our low temperature fit and analytical model, Eq. (8), is given as a blue dashed line and it is discussed in Secs. III B and III C in more detail. For comparison, the energies from the fitted partition function of Ref. 2 is shown as black dots. These two do not manifest dissociation, and therefore, are not relevant at "higher T."

The horizontal dashed-dotted lines show the zero Kelvin energies for the ion and its fragments in Eq. (2). One of these lines presents the energy for the "barrier to linearity," i.e., the minimum energy needed for the transformation to the linear molecular geometry on the zero Kelvin Born–Oppenheimer surface.

TABLE I. NVT energetics of the H_3^+ molecular ion at low temperatures—here the same data applies for all three densities. The energies are given in the units of Hartree (atomic units) and with 2 SEM error estimates. The energies from our low T fit (LTFIT) from Eq. (7) and those from the fit of Ref. 2 (NT) are also given as comparison. At 0 K, the best upper bound is given, see the footnote *c*.

$T(K)$	PIMC[a]	LTFIT[a]	NT fit[b]
0		−1.3231	(−1.32367)[c]
∼160.61	−1.3227(7)	−1.3227	−1.3232
∼321.22	−1.3221(6)	−1.3220	−1.3225
∼642.45	−1.3198(6)	−1.3202	−1.3209
∼1052.6	−1.3173(7)	−1.3171	−1.3179
∼1365.2	−1.3143(5)	−1.3141	−1.3148
∼2000.3	−1.3064(7)	−1.3065	−1.3070
∼2569.8	−1.2983(8)	−1.2984	−1.2989
∼3049.2	−1.2905(12)	−1.2909	−1.2917
∼3499.3	−1.2840(12)	−1.2835	−1.2847
∼3855.6	−1.2774(7)	−1.2774	−1.2792

[a]This work.
[b]Calculated from the fit given in Ref. 2.
[c]Para-H_3^+, see Refs. 23 and 25.

Within the considered molecular densities, $T \approx 4000$ K can be considered as apparent dissociation temperature. The energetics below 4000 K is so close to density independent that the differences between the three curves in Fig. 1 cannot be seen.

Above 4000 K, the density dependence is clearly seen as varying composition of fragments. In the range from 4000 to 10 000 K, the changing dissociation–recombination balance leads to distinctly different energetics, and above that, at our highest simulation temperatures the thermal ionization of hydrogen atoms starts contributing to the energy. However, it is worth pointing out that the temperature limits of these three ranges, i.e., about $0 - 4000$ K, about $4000 - 10\,000$ K, and above 10 000 K, are subject to changes with larger variation of densities.

TABLE II. PIMC NVT energetics of the H_3^+ molecular ion at high temperatures for the three densities (expressed as the number of molecular ions per volume), see Fig. 1. Notations are the same as in Table I.

$T(K)$	$(300a_0)^{-3}$	$(100a_0)^{-3}$	$(50a_0)^{-3}$
∼3999.2	−1.152(16)		
∼4050.0	−1.19(6)		
∼4100.4	−0.9995(4)		
∼4498.2	−0.9993(4)	−1.219(34)	−1.244(15)
∼4819.5	−0.9993(4)		−1.215(37)
∼5139.6	−0.9995(4)	−1.020(33)	−1.169(29)
∼5634.8			−1.156(66)
∼6070.3	−0.9991(4)	−1.018(18)	−1.062(35)
∼7017.2	−0.9995(4)	−1.008(9)	−1.024(12)
∼10279	−0.997(3)	−0.9995(8)	−1.003(3)
∼12016	−0.9993(6)		
∼13997	−0.86(10)		
∼14951	−0.805(23)	−0.988(8)	−0.9957(8)

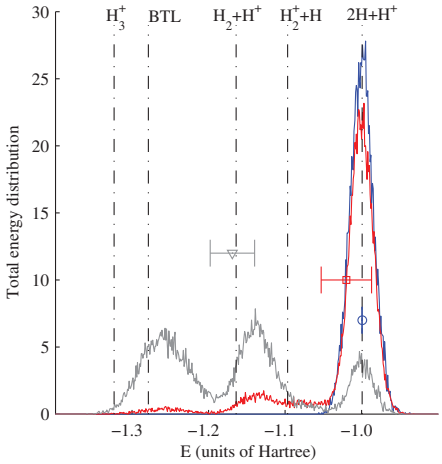

FIG. 2. Histogram of total energy sampling pinned in boxes of width $0.001E_H$ from at least $(2 \times 10^4) \times 10^5$ Monte Carlo samples averaged over blocks of 10^5 samples. The energy expectation values are also given with 2 SEM error estimates. The temperature and the Trotter number are ∼5139.6 K and 2048, respectively. The histograms are normalized to unity for all three densities. Other notations are taken from Fig. 1.

Above 10 000 K, in our lowest density case the thermal ionization of H atoms is evident, see Fig. 1, but for our higher density cases some 15 000 K is needed to bring up first signs of ionization. Similar trend for the ionization is stated in Ref. 24, although the density is notably less than our lowest one.

Let us now consider the dissociation–recombination reaction chain, Eq. (2), and the contributing fragments to the quantum statistical NVT equilibrium trying to give an intuitive classical-like picture of the composition. With finite T, instead of zero, we have finite β, instead of infinite, that brings classical nature to the system the more, the higher the temperature. In other words, the partial decoherence in our five-particle quantum system increases with increasing temperature, that enables us to distinguish the fragments as separate molecules and atoms in thermal equilibrium. Based on this interpretation, we show the total energy distribution in Fig. 2 from sampling the imaginary time paths at about 5000 K with $M = 2048$ for all considered densities.

For our highest density (gray in Fig. 2), for example, we see three main peaks and by inspection of the energy distribution the first and the second can clearly be assigned to the rovibrationally excited H_3^+ and $H_2 + H^+$, respectively. As there are no rovibrational excitations available for $2H + H^+$, the third main peak average position is very close to $-1E_H$. The fourth fragment, $H_2^+ + H$, can be identified as the small high-energy side shoulder of $H_2 + H^+$ peak. With the interpretation of the area under the peak as the abundance of the fragment in the equilibrium we find this contribution to be much smaller than that of the others, for which we can suggest following explanations. Probably due to loose binding of H_2^+ the distribution of its energetics is broad, and therefore, partly covered by the neighboring narrow peaks. Also, the larger entropy factor $-TS$ in free energy of the three particle system $2H+H^+$ increases its contribution. Lower densities make this effect even stronger as is distinctly seen in the Fig. 2.

It is important to note, however, that the above illustration is dependent on the block averaging procedure, see the caption of Fig. 2. Pinning the energy data of each and every sample, i.e., choosing block of size one sample, would broaden the peaks in Fig. 2. At the opposite limit, all samples in one block, would give the single mean energy or the ensemble average corresponding to the quantum statistical expectation value. From the highest density to the lowest, the expectation values are $-1.169(29)E_h$, $-1.020(33)E_h$, and $-0.9995(4)$, respectively, Figs. 1 and 2, where the statistical uncertainty decreases with increasing simulation length.

B. Molecular partition function

To compare with the other published approaches for the molecular partition function based on single molecule quantum chemistry we start from the lowest temperature range from 0 to ∼4000 K, where the molecule does not essentially dissociate, yet.

We present a low temperature H_3^+ molecular partition function as a first approximation for the modeling of low density H_3^+ ion containing atmospheres. Our aim is to find a simple analytical form, which can be accurately fitted to the NVT energies from our simulations.

The partition function in terms of the Helmholtz free energy F is written as

$$Z = e^{-\beta F}, \tag{4}$$

where $\beta = (k_B T)^{-1}$, and the energy expectation value is straightforwardly derived from the partition function as

$$\langle E \rangle = -\frac{1}{Z}\frac{\partial Z}{\partial \beta}. \tag{5}$$

After solving the free energy from Eq. (4) as

$$F(T) = -k_B T \ln Z(T), \tag{6}$$

we write $F(T) = -k_B T f(T)$ and the energy expectation value may be written as

$$\langle E \rangle = k_B T^2 \frac{\partial f(T)}{\partial T}. \tag{7}$$

We find that a well-behaving function fitting perfectly into our simulation data,

$$\langle E \rangle = k_B T^2 (a e^{-bT} + c) + d e^{-\alpha/T}, \tag{8}$$

allows analytical integration of Eq. (7) for $f(T)$ or $\ln Z(T)$,

$$\ln Z(T) = -\frac{a}{b} e^{-bT} + cT + \frac{d}{k_B \alpha} e^{-\alpha/T} + D. \tag{9}$$

Using the boundary condition for the molecular partition function with a nondegenerate ground state, $Z(0) = 1$ or $\ln Z(0) = 0$, we get $D = a/b$ in our model. Another choice, inclusion of the contributions from the ground state spin degeneracy factor and the zero-point rotations would give $Z(0) = \xi > 1$ and $D = a/b + \ln \xi$, and thus, shift the function $\ln Z$ by a constant, only. We have chosen the first and more conventional boundary value, $Z(0) = 1$.

The weighted least squares fit of the above energy function, Eq. (8), to our data for temperatures up to about 3900 K, see Table I, gives the parameters,

$$a = 0.00157426,$$
$$b = 0.000132273,$$
$$c = -6.15622 \times 10^{-6},$$
$$d = 0.00157430,$$
$$\alpha = 269.410, \text{ and}$$
$$D = a/b \approx 11.9016.$$

In the fit, in addition to the $(2\text{SEM})^{-2}$ weights, we force the first derivative of the energy with respect to the temperature to be monotonically increasing up to 3900 K. The fit extrapolates the 0 K energy to about $0.000\,549 E_{\text{H}}$ above that of the para-H_3^+, i.e., it gives an excellent match within the statistical error estimate.

In Fig. 3, the function $\ln Z(T)$ from Eq. (9) is shown in the range $0 < T < 4000$ K — the behavior of the model at higher T is illustrated by the dashed line. Above 4000 K, the three curves for different densities are obtained from those shown in Fig. 1 by numerical integration of Eq. (7) as

$$\ln Z(T) = \ln Z(T_1) + \int_{T_1}^{T} \frac{\langle E \rangle}{k_{\text{B}} T^2} \mathrm{d}T, \tag{10}$$

where $T_1 = 500$ K.

In Ref. 2, Neale and Tennyson (NT) have presented the partition function $\ln Z(T)$ based on a semi-empirical potential energy surface, see Fig. 3. The NT partition function has conventionally been used in atmospheric models. The overall shape is similar to the one of ours. However, the energy $\langle E \rangle$ evaluated from their fit tends to be systematically lower than ours, although roughly within our 2SEM error limits. Thus, the deviations are not visible in Fig. 1. The energy zero of the NT fit, black dots in Figs. 1 and 3, is the same as ours in this work, and thus, allows direct comparison in Fig. 1.

Also in Fig. 3, the difference due to the choice of the $J = 0$ state as the zero reference is illustrated by the NT partition function values, black pluses — the shape is notably affected at low T, only. As mentioned above, already, the zero reference of $\ln Z$ can be chosen differently.

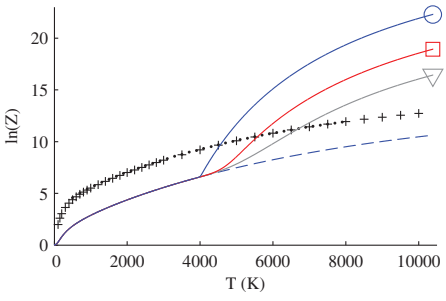

FIG. 3. The molecular NVT ensemble $\ln Z(T)$ from the energetics in Fig. 1 with the same notations. The blue solid line below 4000 K and its extrapolation (dashed line) are from Eq. (9), whereas the curves for three densities are from Eq. (10). The $\ln Z(T)$ data (black pluses) and the fit (black dots) of Ref. 2 are also shown. The black dots have the same zero energy as the partition function of this work (see text).

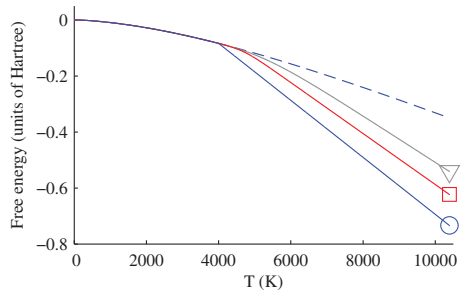

FIG. 4. Helmholtz free energy from Eq. (5) in the units of Hartree. Notations are the same as in Fig. 3.

Our low temperature partition function, Eq. (9), is close to complete. With the PIMC approach, we implicitly include all of the quantum states in the system with correct weight without any approximations. This partition function is the best one for the modeling of the low density H_3^+ ion containing atmospheres, at the moment. However, it is valid up to the dissociation temperature, only. As soon as the density dependence starts playing larger role, more complex models are needed. Such models can be fitted to our PIMC data given in Tables I and II.

C. Other thermodynamic functions

In Fig. 4, we show the Helmholtz free energy from combined Eqs. (6) and (9). As expected, lower density or larger volume per molecule lowers the free energy due to the increasing entropic factor. Dissociation and the consequent fragments help in filling both the space and phase space more uniformly or in less localized manner.

This kind of decreasing order is seen more clearly in the increasing entropy, shown in Fig. 5. The entropy has been evaluated from

$$S = \frac{U - F}{T}, \tag{11}$$

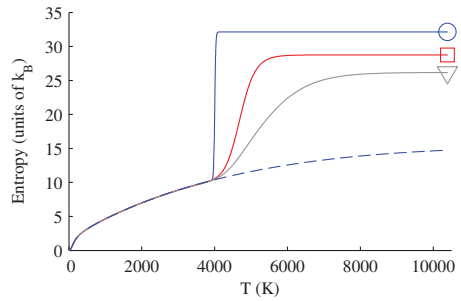

FIG. 5. Entropy from Eq. (11) in the units of k_{B}. Notations are the same as in Fig. 3.

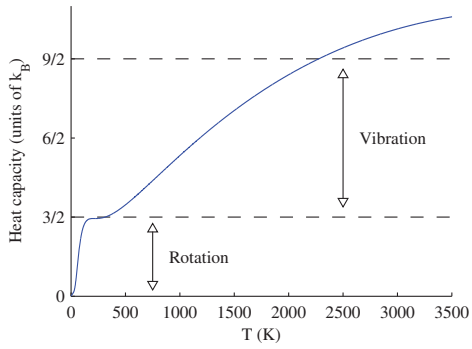

FIG. 6. Molecular heat capacity as a function of temperature calculated using the analytical model of this work. The values on the y-axis are given in units of the Boltzmann constant k_B.

where the internal energy is $U = \langle E \rangle - \langle E \rangle_{T=0}$. As expected, both the total energy (internal energy) and entropy reveal the dissociation taking place, similarly.

Finally, in Fig. 6, we present the molecular constant volume heat capacity

$$C_V = \frac{\partial \langle E \rangle}{\partial T}, \tag{12}$$

where $\langle E \rangle$ is taken from Eq. (8), which is valid below dissociation temperatures, only.

Considering the goodness of our functional form for $\langle E \rangle$, it is very convincing to see the plateau at about $3/2k_B$ corresponding to "saturation" of the contribution from the three rotational degrees of freedom. Thus, above 200 K the rotational degrees of freedom obey the classical equipartition principle of energy. It is the last term in the functional form of Eq. (8), that gives the flexibility for such detailed description of the energetics.

It should be emphasized that the plateau is not artificially constructed to appear at $3/2k_B$, except for a restriction given for the first derivative of the total energy to be increasing. Thus, the analytical model we present, Eq. (8), is found to be exceptionally successful at low temperatures, i.e., below dissociation temperature.

IV. CONCLUSIONS

We have evaluated the temperature dependent quantum statistics of the five-particle molecular ion H_3^+ at low densities far beyond its apparent dissociation temperature at about 4000 K. This is done with the PIMC method, which is basis set and trial wavefunction free approach and includes the Coulomb interactions exactly. Thus, we are able to extend the traditional *ab initio* quantum chemistry with full account of correlations to finite temperatures without approximations, also including the contributions from nuclear thermal and equilibrium quantum dynamics.

At higher temperatures, the temperature dependent mixed state description of the H_3^+ ion, the density dependent equilibrium dissociation–recombination balance, and the energetics have been evaluated for the first time. With the rising temperature the rovibrational excitations contribute to the energetics, as expected, whereas the electronic part remains in its ground state in the spirit of the Born–Oppenheimer approximation. At about 4000 K the fragments of the molecule, $H_2 + H^+$, $H_2^+ + H$, and $2H + H^+$, start contributing. Therefore, presence of the H_3^+ ion becomes less dominant and eventually negligible in high enough T.

We have also shown how the partial decoherence in the mixed state can be used for interpretation of the fragment composition of the equilibrium reaction. Furthermore, we have evaluated explicitly the related molecular partition function, free energy, entropy, and heat capacity, all as functions of temperature. An accurate analytical functional form for the internal energy is given below dissociation temperature. We consider all these as major additions to the earlier published studies of H_3^+, where the dissociation–recombination reaction has been neglected.

It is fair to admit, however, that PIMC is computationally heavy for good statistical accuracy and approximations are needed to solve the "Fermion sign problem" in cases where exchange interaction becomes essential. With H_3^+, however, we do not face the Fermion sign problem, as the proton wavefunctions do not overlap noteworthy and the two electrons can be assumed to form a singlet state, due to large singlet to triplet excitation energy.

ACKNOWLEDGMENTS

We thank the Academy of Finland for financial support, and we also thank the Finnish IT Center for Science (CSC) and Material Sciences National Grid Infrastructure (M-grid, akaatti) for computational resources.

[1] J. J. Thomson, Phil. Mag. **21**, 225 (1911).
[2] L. Neale and J. Tennyson, Astrophys. J. **454**, L169 (1995).
[3] M. B. Lystrup, S. Miller, N. D. Russo, J. R. J. Vervack, and T. Stallard, Astrophys. J. **677**, 790 (2008).
[4] T. T. Koskinen, A. D. Aylward, and S. Miller, Astrophys. J. **693**, 868 (2009).
[5] L. Neale, S. Miller, and J. Tennyson, Astrophys. J. **464**, 516 (1996).
[6] G. J. Harris, A. E. Lynas-Gray, S. Miller, and J. Tennyson, Astrophys. J. **600**, 1025 (2004).
[7] T. T. Koskinen, A. D. Aylward, C. G. A. Smith, and S. Miller, Astrophys. J. **661**, 515 (2007).
[8] B. M. Dinelli, O. L. Polyansky, and J. Tennyson, J. Chem. Phys. **103**, 10433 (1995).
[9] D. M. Ceperley, Rev. Mod. Phys. **67**, 279 (1995).
[10] M. Pierce and E. Manousakis, Phys. Rev. B **59**, 3802 (1999).
[11] Y. Kwon and K. B. Whaley, Phys. Rev. Lett. **83**, 4108(4) (1999).
[12] L. Knoll and D. Marx, Eur. Phys. J. D **10**, 353 (2000).
[13] J. E. Cuervo and P.-N. Roy, J. Chem. Phys. **125**, 124314 (2006).
[14] I. Kylänpää and T. T. Rantala, Phys. Rev. A **80**, 024504 (2009).
[15] I. Kylänpää and T. T. Rantala, J. Chem. Phys. **133**, 044312 (2010).
[16] R. P. Feynman, *Statistical Mechanics* (Perseus Books, Reading, MA, 1998).
[17] R. G. Storer, J. Math. Phys. **9**, 964 (1968).
[18] N. Metropolis, A. W. Rosenbluth, M. N. Rosenbluth, A. H. Teller, and E. Teller, J. Chem. Phys. **21**, 1087 (1953).
[19] C. Chakravarty, M. C. Gordillo, and D. M. Ceperley, J. Chem. Phys. **109**, 2123 (1998).
[20] M. F. Herman, E. J. Bruskin, and B. J. Berne, J. Chem. Phys. **76**, 5150 (1982).
[21] M. Misakian and J. C. Zorn, Phys. Rev. Lett. **27**, 174 (1971).

[22]Ch. Jungen, I. Dabrowski, G. Herzberg, and M. Vervloet, J. Chem. Phys. **93**, 2289 (1990).
[23]M. Pavanello and L. Adamowicz, J. Chem. Phys. **130**, 034104 (2009).
[24]T. T. Koskinen, R. V. Yelle, P. Lavvas, and N. K. Lewis, Astrophys. J **723**, 116 (2010).
[25]W. Kutzelnigg and R. Jaquet, Phil. Trans. R. Soc. A **364**, 2855 (2006).